



UNIVERSITAT POLITÈCNICA
DE CATALUNYA
BARCELONATECH

Assessment and characterization of subsidence in the Catalan potash basin

Nor Sidki Rius

ADVERTIMENT La consulta d'aquesta tesi queda condicionada a l'acceptació de les següents condicions d'ús: La difusió d'aquesta tesi per mitjà del repositori institucional UPCommons (<http://upcommons.upc.edu/tesis>) i el repositori cooperatiu TDX (<http://www.tdx.cat/>) ha estat autoritzada pels titulars dels drets de propietat intel·lectual **únicament per a usos privats** emmarcats en activitats d'investigació i docència. No s'autoritza la seva reproducció amb finalitats de lucre ni la seva difusió i posada a disposició des d'un lloc aliè al servei UPCommons o TDX. No s'autoritza la presentació del seu contingut en una finestra o marc aliè a UPCommons (*framing*). Aquesta reserva de drets afecta tant al resum de presentació de la tesi com als seus continguts. En la utilització o cita de parts de la tesi és obligat indicar el nom de la persona autora.

ADVERTENCIA La consulta de esta tesis queda condicionada a la aceptación de las siguientes condiciones de uso: La difusión de esta tesis por medio del repositorio institucional UPCommons (<http://upcommons.upc.edu/tesis>) y el repositorio cooperativo TDR (<http://www.tdx.cat/?locale-attribute=es>) ha sido autorizada por los titulares de los derechos de propiedad intelectual **únicamente para usos privados enmarcados** en actividades de investigación y docencia. No se autoriza su reproducción con finalidades de lucro ni su difusión y puesta a disposición desde un sitio ajeno al servicio UPCommons No se autoriza la presentación de su contenido en una ventana o marco ajeno a UPCommons (*framing*). Esta reserva de derechos afecta tanto al resumen de presentación de la tesis como a sus contenidos. En la utilización o cita de partes de la tesis es obligado indicar el nombre de la persona autora.

WARNING On having consulted this thesis you're accepting the following use conditions: Spreading this thesis by the institutional repository UPCommons (<http://upcommons.upc.edu/tesis>) and the cooperative repository TDX (<http://www.tdx.cat/?locale-attribute=en>) has been authorized by the titular of the intellectual property rights **only for private uses** placed in investigation and teaching activities. Reproduction with lucrative aims is not authorized neither its spreading nor availability from a site foreign to the UPCommons service. Introducing its content in a window or frame foreign to the UPCommons service is not authorized (*framing*). These rights affect to the presentation summary of the thesis as well as to its contents. In the using or citation of parts of the thesis it's obliged to indicate the name of the author.

Assessment and characterization of subsidence in the Catalan Potash Basin

By

Nor Sidki-Rius

Supervisors: Dr. Lluís Sanmiquel Pera

Dr. Marc Bascompta Massanes

Manresa, Spain

2023

Thesis for the Doctor of Philosophy Degree at the Polytechnic University of
Catalonia within Doctoral Program of Natural Resources and Environment

Abstract

The importance of potash is inevitable to life on the planet earth as it is required by living mechanisms including plants, animals and human beings. In Europe, this vital ore is produced mainly by Germany and Spain, which consists of up to 10% of the global supply. As a matter of fact, higher demand for potash may be required due to population growth. This may lead to increasing potash mining activities, which might create instability with regard to the geomechanical features of the mining areas and potential environmental and social impacts.

The main objective of this research is to approach innovative models that can describe the geomechanical behavior of the Catalan Potash Basin deposit. Including concern about surface subsidence, high deformations and collapses of underground potash mining, with the ultimate goal of improving the present working conditions and mitigating the environmental impacts. Four Specific objectives have been defined; (1) The creation of a model to predict subsidence based on the geomechanical parameters of the ore deposit. (2) The Geochemical characterization of the pelitic and insoluble phase detected between the saline beds and within them. (3) The characterization of the surface subsidence basin, including boundary angle and distance of influence. (4) The assessment of the deformations in the underground mining facilities. To achieve these objectives, a combination of FEM, InSAR, GPS, Laser Scanner and Geochemical techniques has been used to predict the subsidence and achieve a better geomechanical behavior characterization of it, which have resulted in two main outcomes. First, it has been established that numerical 2D modeling is a useful tool for planning land management and mining operations, providing the flexibility and predictability needed to manage huge surfaces and reduce environmental consequences. The approach is also adaptable to other subsurface infrastructure types. Second, the subsidence basin has been successfully characterized. Third, pelitic layers with insoluble mineralogy within saline lithologies have successfully undergone geochemical examination. However, to expand the study area to include the entire active ore deposit mineralogy, additional examination will be required. Fourth, the laser scanner technique has been satisfactorily assessed, it has given important insights into the displacements that occur during the early opening of an underground mining drift affirming that it is a suitable technique to be implemented for routinely tracking deformations in the geomechanical management of the ore deposit. However, it is necessary to perform a precise topographic control of the targets used, in order to correctly georeference the point clouds produced by the laser scanner.

Furthermore, characterization of the subsidence has been successfully assessed in the eastern portion of the Catalan Potash Basin. With the help of the methods mentioned, it was possible to evaluate a large dataset and identify four unique zones, one of which was experiencing residual subsidence. Mining firms may choose to use this flexible and effective method and apply it to other studies involving subsidence. In the end, based on the results and objectives achieved in the study, suggestions for further research have been proposed, which can further advance the knowledge in this line of research.

The structure of the thesis is as follows: Chapter 1 introduces the case study and states the objectives and hypothesis developed in the research. In chapter two, an extensive and precise bibliographic review is made. Chapter 3 describes the methodologies followed in the different investigations developed. Chapter 4 presents the results and discusses them. Finally, Chapter 5 presents the conclusions and proposes future research to improve and complement the knowledge obtained.

Keywords: *Underground mining, Subsidence, Numerical modelling, Laser Scanner, Potash, Phyllosilicates, Environmental impact*

Acknowledgements

I would like to thank my family for all the support and love they have given me over the years.

Also, I would like to thank my supervisors, Dr Lluís Sanmiquel and Dr Marc Bascompta for their guidance and dedication. As well as to all the professors of the mining section for their valuable teachings during all these years of formation.

Finally, to my fellow PhD colleagues, for all the laughs and good times we have had together.

Table of Contents

Abstract	1
Keywords:	2
Acknowledgements	3
Table of Contents	4
List of figures	11
List of tables	17
List of equations	19
Chapter 1	22
1 Introduction	23
1.1 Geological structural context	25
1.2 Local structure	31
1.2.1 The Mig-món outcrop structure	31
1.2.2 The Sucova structure.....	33
1.2.3 Tordell’s fault	34
1.2.4 Sinkholes of Cardaner river valley.....	35
1.3 Extracting method	36
1.4. Objectives	38
1.4.1 General objectives.....	38
1.4.1.1 Specific objectives	38
1.5. Hypothesis and methodology	38
1.5.1 Hypothesis 1	38
1.5.2 Hypothesis 2.....	39
1.5.3 Hypothesis 3.....	39
1.5.4 Hypothesis 4.....	39
Chapter 2	41
2. Literature review	42
2.1 Mechanical concepts	42
2.1.1 Rheological models and lineal viscoelasticity	42
2.1.2 “Creep”. Fluency concept.....	46
2.1.3 Discontinuities	47
2.1.4 Rock masses classifications	52

2.1.5 Crystal structure. Grain size	53
2.2 Rehology: Salt deformation mechanisms	55
2.2.1 Rheological equations for rock salt	59
2.2.2 Mechanical behavior of saline materials: transport fluid properties and associated microstructures	60
2.2.2.2 Fluid transport in salts	62
2.2.2.3 Brine migration	63
2.2.2.4 Vapor phase transport within the connected porosity	64
2.2.2.5 Liquid transport by force gradient applied to salt.....	64
2.2.3 The permeability of granular Salt.....	64
2.2.4 Associated Microstructures on the strain/ deformation mechanisms	67
2.3 Geochemistry.....	69
2.3.1 Sulphates in evaporitic deposits.....	69
2.3.2 Phyllosilicates.....	69
2.3.2.1 Clays family.....	70
2.3.2.2 Micas family	71
2.3.2.3 Chlorite family	71
2.4 Subsidence	72
2.4.1 The history of the study of subsidence.....	72
2.4.2 Subsidence due to underground mining	73
2.4.2.1 Discontinuous subsidence mechanisms.....	74
2.4.2.2 Continuous subsidence mechanisms.....	76
2.4.3 Surface subsidence areas	79
2.4.4 Introduction to subsidence of evaporite reservoirs.....	80
2.4.4.1 Subsidence in C.P.B	81
2.4.5 Subsidence prediction methods.....	82
2.4.5.1 Surface subsidence variables and their general relationship	84
2.4.5.2 Typical curve method	84
2.4.5.3 Profile function method	84
2.4.5.4 Probability integration method	84
2.4.5.5 Surface subsidence prediction for mountain area	85
2.5 Numerical modeling	85
2.5.1 Subsidence Prediction in Ebro Basin and Catalan Potash Basin (C.P.B)	86
2.5.2 Finite Element Method (F.E.M.)	86
2.5.2.1 Finite element method from a practical point of view	89
2.5.3 Finite element method (F.E.M.) applied to underground infrastructures	89

2.5.3.1 Constitutive models for rocks	90
2.5.3.1.2 Failure criteria	90
2.6 Global Positioning System (GPS)	92
2.6.1 The GPS segments	93
2.6.2 How the GPS system work	94
2.6.3 GPS Satellite hardware	94
2.6.4 How the position of satellites is known	95
2.6.4.1 Example of Calculation of user position	95
2.6.5 Differential GPS methodology (DGPS)	96
2.7. InSAR Technique	96
2.7.1 Synthetic Aperture Radar	97
2.7.2 Interferometric Synthetic Aperture Radar	98
2.7.3 Movement measurement.....	101
2.7.4 Surface displacement caused by natural events.....	101
2.7.5 Background of the study of subsidence in the CPB.....	102
2.7.5.1 Methodology used to quantify the subsidence produced in the CPB	103
2.7.5.2 Quality control methods.....	104
2.7.5.2.1 Software-based quality control method	104
2.7.5.2.1.1 Remediation of control points method.....	104
2.8 Terrestrial Laser Scanning Theory	105
2.8.1 Basic principles.....	107
Chapter 03	114
3. Materials and Methods.....	115
3.1 Subsidence Management and Prediction System.....	115
3.1.1 GPS and InSAR technology.....	115
3.1.2 Targeted area.....	116
3.1.3 Subsidence average profile.....	117
3.1.4 Numerical model design	118
3.1.4.1 Design of the mining drifts	120
3.1.4.2 Numerical model definition.....	120
3.1.4.3 Young's modulus decreasing methodology	121
3.2. Definition of characteristic subsidence parameters. A case study in the Catalan Potash Basin.....	123
3.2.1 Database creation.....	123
3.2.2 Database management.....	125
3.2.3 Characteristic function of the subsidence basin.....	127

3.3 Statistical Model Definition.....	130
3.3.1 Characteristics of the statistical model	131
3.3.1.1 Fault	131
3.3.1.2 Topography	131
3.3.1.3 Overburden	131
3.3.1.4 Typology	132
3.3.1.5 Percentage of filling.....	132
3.3.1.6 Extraction ratio.....	132
3.4 Geomechanical and geochemical parameters of saline Lithologies	132
3.4.1 Sampling	132
3.4.2 Geomechanical behavior.....	134
3.4.2.1 Analysis of Discontinuities.....	134
3.4.2.2 Particle-size analysis (PSA) methodology.....	135
3.4.2.3 Determination of natural density methodology	138
3.4.2.3.1 Density of Paraffine.....	141
3.4.2.4 Humidity Methodology test	142
3.4.2.4.1 Determination of Concentration.....	143
3.4.2.5 Determination of dry density test methodology.....	144
3.4.2.6 Determination of insoluble particles percentage	145
3.4.2.7 Insoluble particle analysis with geochemical techniques.....	145
3.4.2.7.1 Scanning Electron Microscopy (SEM) with Energy dispersive X-ray Spectroscopy (EDS)	145
3.4.2.7.2 X-ray powder diffraction (XRD).....	146
3.5 Laser Scanner post-processing	147
3.5.1 Cyclone software (Leyca Geosystems)	147
3.5.1.1 Cyclone REGISTER 360 (Leica Geosystems).....	147
3.5.1.1.1 Import BLK360 Data.....	149
3.5.1.1.2 Review and Optimize.....	150
3.5.1.1.3 Targets.....	154
3.5.1.4 Finalize and Report	156
3.5.1.2 Cyclone 3DR (Leica Geosystems).....	157
3.5.1.2.1 The 3D meshes	160
3.5.1.2.1.1 Meshing in two steps	160
3.5.1.2.1.2 Spherical mesh	161
3.5.1.2.1.3 2D mesh.....	161
3.5.1.2.2 Generation of sections.....	162
3.5.1.2.2.1 Section analysis	163
Chapter 4	166

4. Results and Discussion.....	167
4.1 Results and Discussion in “Subsidence Management and Prediction System: A Case Study in Potash Mining”	167
4.2. Definition of characteristic subsidence parameters. A case study in the Catalan Potash Basin.....	174
4.2.1 Active and residual areas in the Catalan Potash Basin (E-CPB).....	174
4.2.2 Characteristic boundary angle and distance of influence	175
4.2.3 Approximation of the characteristic function of the subsidence basin.	179
4.3 Geomechanics and geochemical results.....	182
4.3.1 Roughness of discontinuities. The JRC parameter.	182
4.3.2 Particle-size analysis (PSA)	183
4.3.3 Determination of natural density	193
4.3.4 Humidity.....	194
4.3.5 Determination of dry density	194
4.3.6 Determination of % Insoluble particles	195
4.4 Laser scan results	197
4.4.1 GC-01, the ramp drift	197
4.4.2 GC-02(MC-3R, transversal drift)	203
Chapter 5	214
5.1. Findings and hypothesis fulfilment	215
5.1.1 Hypothesis 1	215
5.1.2 Hypothesis 2.....	215
5.1.3 Hypothesis 3.....	216
5.1.4 Hypothesis 4.....	217
5.2 Implication of the findings: Further research and improvements.....	217
5.2.1 Hypothesis 1	217
5.2.2 Hypothesis 2.....	218
5.2.3 Hypothesis 3.....	219
5.2.4 Hypothesis 4.....	219
5.3 Conclusions	219
References	221
Appendixes	239
Appendix 1.....	240
Samples pictures	240
Intermediate salt	240

Upper salt.....	243
A potash bed.....	246
Transformed salt.....	249
Stratigraphic column samples	251
Appendix 2.....	255
Panreac Paraffin.....	255
Appendix 3.....	256
Barton comb profiles	256
Appendix 4.....	262
Particle size distribution test.....	262
Appendix 5.....	266
Natural density test.....	266
Appendix 6.....	270
Humidity test	270
Appendix 7.....	274
Insoluble particles.....	274
Appendix 8.....	278
Binocular Microscope images	278
Appendix 9.....	280
SEM images	280
Appendix 10.....	294
XRD diffraction graphics.....	294
% insoluble particles Intermediated salt	294
% insoluble particles A potash bed	295
% insoluble particles Transformed salt	296
% insoluble particles (Transformed salt).....	297
% insoluble particles Upper salt	298
Appendix 11.....	299
LASER SCAN	299
GC-01.....	299
GC-02.....	304
Map Appendixes.....	314
Appendix 12.....	315
Cabanasses' mine map.....	315
Vilafruns' mine map.....	317

Appendix 13	319
Laser scanner sections (GC-01 and GC-02).....	319
Publications	332

List of figures

Figure 1.1 Location of the case study. The CPB deposit is highlighted in red. _____	25
Figure 1.2 Formation of the Ebro Basin and the Catalan Potash Basin (CPB). (Adapted from Geopark scheme). _____	27
Figure 1.4 Stratigraphic section of the Catalan evaporitic sequence (Adapted from Cendón et al, 2003). _____	31
Figure 1.5 Mig-món anticline outcrop. _____	32
Figure 1.6 Mig-món anticline outcrop scheme (Adapted from Central Catalonia Geopark scheme). _____	32
Figure 1.7 Súria municipality, the Cabanasses mine shafts and the Mig-Món outcrop. _____	33
Figure 1.8 Diagram of surface and underground mining infrastructures located in the municipality of Súria (Adapted from Central Catalonia Geopark scheme). _____	33
Figure 1.9 General view of the Sucova structure (Adapted from Fàbrega et al., (2007)). _____	34
Figure 1.10 The geological structure of the Tordell's fault. _____	35
Figure 1.11 Example 1 of Cardaner river valley sinkhole. _____	36
Figure 1.12 Example 2 of Cardaner river valley sinkhole. _____	36
Figure 1.13 Room and Pillar method (Adapted from Hamrin, 1980). _____	37
Figure 2.1 Scheme of Kelvin-Voigt model (Dusseault & Fordham, 1993). _____	43
Figure 2.2 Scheme of Maxwell model (Dusseault & Fordham, 1993). _____	44
Figure 2.3a, and, b Schemes of Zener model (Mainardi & Spada, 2011). _____	45
Figure 2.4 Scheme of Burgers model (Mainardi & Spada, 2011). _____	46
Figure 2.5 Creep curve scheme of a saline rock (Jeremic, 1994). _____	47
Figure 2.6 a, b, c, d Conceptual model of forming and block fall (Camara Zapata, 2019). _____	48
Figure 2.7 Patton's experiment on the shear strength of saw tooth specimens (Hoek, 2007). _____	49
Figure 2.8 Roughness profiles and corresponding JRC values (N. Barton & Choubey, 1977). _____	51
Figure 2.9 Example of high rough discontinuity in Cabanasses ore deposit (Camara, 2019). _____	52
Figure 2.10 Polycrystalline halite structure with fluid inclusions and grain boundaries (Spiers et al., 1986). _____	54
Figure 2.11 Grain size influence in creep compaction curves in brine saturated samples (Spiers et al., 1990). _____	54

- Figure 2.12 Characteristic processes and mechanisms of saline materials. Modified from (Barberán, 2000). _____ 55
- Figure 2.13 Schematic drawing of the microstructural processes that can operate during deformation of halite at temperatures in the range 20-200°C. Different shades of green represent crystals with different orientations (Urai et al., 2008). _____ 56
- Figure 2.14 Simplified deformation map, showing the general conditions where each deformation mechanism dominates relative to one another (Davis et al., 2011). _____ 57
- Figure 2.15 Steady state strain rate data of fine-grained wet halite samples deforming by solution- precipitation processes, showing a stress exponent n close to 1. Gray bands represent the theoretical flow law for this process (Spiers et al., 1990). _____ 60
- Figure 2.16 Strain/Deformation mechanism of saline material. Fluid pressure P between (0.1 to 20 MPa). σ deviatoric force, μ Elastic modulus, T Temperature, and T_m Melting Point/Temperature (Spiers et al., 1990). _____ 62
- Figure 2.17 Schematic diagrams illustrating the pattern of mass transfer involved in creep by pressure solution. (a) Compaction creep in a porous or granular polycrystalline aggregate saturated with fluid Figure. (b) Conventional creep in a dense polycrystalline material. In both cases, grain boundaries contain fluid in an adsorbed film or island-channel form (Spiers et al., 1990). _____ 67
- Figure 2.18. Microstructures graphic associated with salt strain/deformation (Spiers et al., 1990). _____ 68
- Figure 2.19 Microphotography obtained in the laboratory. (a) Initial granular material ($d_0 = 275 \mu\text{m}$). (b) Compacted salt ($\epsilon_v = 11\%$, $d_0 = 410 \mu\text{m}$), the island-channel microstructure is shown, (c) Compacted salt ($\epsilon_v = 20\%$, $d_0 = 410 \mu\text{m}$), interdigitation, truncation and overdevelopment structures are shown, (d) compacted salt ($\epsilon_v = 24\%$, $d_0 = 175 \mu\text{m}$), interdigitation, truncation and overdevelopment structures are shown (Spiers et al., 1990). _____ 68
- Figure 2.20. Two main types of clay family structures, tetrahedron and octahedron type. The appearance of three different ways of drawing the model: as a sphere-packing model (top row), a ball-and-stick model (middle row), and a polyhedral model (bottom row) (Schulze (2005)). _____ 70
- Figure 2.21 Discontinuous subsidence scheme (after Whittaker and Reddish, 1989). 74
- Figure 2.22 Continous subsidence diagram of the land that sinks due to the subsidence produced by mining in the specific case of a stratified sedimentary deposit (modified by Lee and Abel, Jr, 1983) _____ 74
- Figure 2.24 Process of forming surface movement basin. 1, 2, 3, 4 equal different positions of face advance; s_1 , s_2 , s_3 , and s_4 are surface movement basins formed when the face is at

<i>the corresponding positions of 1, 2, 3, 4, respectively; s04 is the final surface static movement basin. h0 is mining depth. (Peng, 2020)</i>	77
<i>Figure 2.25 Subsidence profile and main parameters (National Coal Board, 1975).</i>	78
<i>Figures 2.26 a Supercritical subsidence basin, b Critical subsidence basin and c Subcritical subsidence basin (Peng, 2020).</i>	78
<i>Figure 2.27 The three zones of a surface subsidence basin (Peng, 2020)</i>	79
<i>Figure 2.28. characteristic angles in a subsidence profile along the directions of a horizontal mining drift.</i>	80
<i>Figure 2.29 Subsidence prediction methodologies are based on four steps; the model, the parameters the algorithm and the software. The average prediction precision of subsidence is 10% (Adapted from Peng, 1992).</i>	83
<i>Figure 2.30 Portioning of the domain into triangular elements (Whiteley, 2014).</i>	88
<i>Figure 2.31 The finite element approximation to the solution of the differential equation (Whiteley, 2014).</i>	88
<i>Figure 2.32 The geometry of the SAR system (Adapted from Bamler & Hartl, 1998 and Laukness, 2010)</i>	98
<i>Figure 2.33 SAR imaging geometry and InSAR geometry. R is the inclination range (distance between the radar and the target), P is the height of the point and is determined as Hp: topographic height, B is the baseline, distance from the orbit, Bp is the perpendicular baseline, which is the projection of the baseline perpendicular to the inclination range, θ is the look angle of the satellite. (Adapted from UN, N.D)</i>	99
<i>Figure 2.36 Operating diagram of a terrestrial laser scanner (Shand and Tooth, 2008)</i>	108
<i>Figure 2.37 Example of basic principles of terrestrial laser scanner data acquisition (Wang et al, 2014).</i>	110
<i>Figure 2.38 Connection of multiple laser scanning stations (Kraus, 2004)</i>	111
<i>Figure 3.1. The methodology followed to reach the average surface subsidence profile.</i>	115
<i>Figure 3.2 The mining area, with the two different perimeters.</i>	117
<i>Figure 3.3. Mining areas with two different perimeters, the five profiles and the twelve selected zones can be seen.</i>	118
<i>Figure 3.4 The stratigraphic column used for the RS2 model.</i>	119
<i>Figure 3.5 Tunnel wizard tool (RS2 software).</i>	120
<i>Figure 3.6. Example of an RS2 model with the geological and drifts characteristics.</i>	121
<i>Figure 3.7. The methodology followed to define Young's modulus decrease.</i>	122
<i>Figure 3.8 Example of the seven stages and their associated Young's modulus (E).</i>	122
<i>Figure 3.9 Young modulus decrease.</i>	123

Figure 3.10. The nine sections are located in the case study area, in pink. _____	126
Figure 3.11. Example of 11 subsidence basins from 2003 to 2021. _____	127
Figure 3.14. Distribution of horizontal strain, surface displacements, boundary angle and surface vertical settlements trough (O'Reilly, M.P. & New, 1982). _____	129
Figure 3.15. Example of strain curvature (Adapted from (National Coal Board, 1975). _____	130
Figure 3.16 Area of interest with 120 points defined _____	131
Figure 3.17 Roughness meter or Barton comb together with the saline sample. _____	134
Figure 3.18 Discontinuity surface of a sample from the intermediate salt lithology. _____	135
Figure 3.19 Udden-Wentworth grain-size classification scheme (Wentworth, 1922). _____	136
Figure 3.20 Example of different particle size distribution well and poor graded (Hillel, 1982). _____	136
Figure 3.21 Example of original material (a) and after the crushing made with the hammer rubber (b). _____	137
Figure 3.22 a) Sieve column, and b) detail of a single sieve; Where samples were tested. _____	137
Figure 3.23 Process of waxed. _____	139
Figure 3.24 Scheme of natural density test, from (Yubero, 2008). _____	140
Figure 3.25 Hydrostatic bascule built with the laboratory material. _____	140
Figure 3.26 Heater used (geology laboratory, EPSEM). _____	144
Figure 3.27 Equipment used for calculating the percentage of insoluble particles. _____	145
Figure 3.28 The four major stages of the projects: Import, Review and Optimize, Finalize and Report, marked in yellow are the setting and file version options. _____	148
Figure 3.29 Setting dialogue, cloud-to-cloud tab _____	149
Figure 3.30 Project and Storage Dialog _____	149
Figure 3.31 Remarkd in yellow Drag and Drop import mechanism and register options on the right side. _____	150
Figure 3.32 Import option. _____	150
Figure 3.33 Visual alignment, source: Leica. _____	151
Figure 3.34 Graphic where it is shown the overlap per cent and the average absolute error. _____	151
Figure 3.37 Summary of erasure options. _____	152
Figure 3.38 "Bounding box" option underline in yellow at the upper part of the window. _____	153
Figure 3.40 Set of blocked links. _____	154
Figure 3.41 blocked link summary graphic. _____	154
Figure 3.42 Optimized button. _____	154

Figure 3.43 a) Marked in yellow is a target located on the wall of a drift b) An example of a target.	155
Figure 3.44 shows the window where it can be seen the option to apply the control "Aplicar control".	155
Figure 3.45 targets displayed in purple.	156
Figure 3.46 a) Report process development b) Report and Publishing option all marked in yellow.	156
Figure 3.47 Cyclone 3DR initial window.	158
Figure 3.48 a) the data just imported b) the data grouped.	158
Figure 3.49, the different software sections.	158
Figure 3.51 Before and after cleaning the point cloud.	159
Figure 3.52 Mesh options.	160
Figure 3.53 Example of the "Two-step mesh" tab.	161
Figure 3.54 the final result of a mesh developed with the option of "two-step mesh".	162
Figure 3.55 Process diagram to build the polyline and the sections.	162
Figure 3.56 a) 2D sections on a grid b) 3D sections making up the drift.	163
Figure 3.57 a) Section according to cyclone 3DR format b) Section modified according to CAD format.	164
Figure 3.58 AutoCAD window with the "height tool" displayed, where it can be seen all the options of measure, also two sections are compared, day fifth and twelfth of March 2020.	164
Figure 3.59 a) undefined section b) Average section. Pink: 18/03/2020, green:25/03/2020 (both from section 10 meter)	165
Figure 4.2. Maximum subsidence values of MP 03.	169
Figure 4.3. Average subsidence profile together with a 90% confidence level.	170
Figure 4.4. Example of the FEM post-processing stage achieved using RS2.	171
Figure 4.5. Average subsidence profile with the results of the sections analyzed.	172
Figure 4.6. a) b) c) d) Sequence of profiles A-A', B-B', C-C' and D-D', from 2020 to 2021.	175
Figure 4.7. Average boundary angle and distance of influence of the active zones together with the profiles (in color pink) used for the analysis.	176
Figure 4.8. Surface transverse settlement profiles in section 1-1'.	180
Figure 4.9. Interpretation of measurements by an empirical Gaussian curve.	180
a) Section 1_1'_2016_2017; b) Section 1_1'_2017_2018.	180
Figure 4.10. Relationship between strain and θ/l meters.	181
Figure 4.11 a) and b) show two examples of samples with discontinuities (a) upper salt, b) Intermediate salt).	183

<i>Figure 4.12 Comparison between Particle Size Distributions of each sample.</i>	_____	189
<i>Figure 4.13 Particle size using a binocular microscope.</i>	_____	192
<i>Figure 4.14 (a) and (b) Two views of the insoluble particles filling the microroughness of the discontinuities.</i>	_____	193
<i>Figure 4.15 (a) Clay fraction particles (Intermediate salt) (b) Clay fraction particles (Upper salt).</i>	_____	196
<i>Figure 4.16 (a) Monoclinical gypsum cristal surrounded with clay fraction particles (Upper salt), (b) Monoclinical gypsum cristal (Transformed salt).</i>	_____	196
<i>Figure 4.17 Section number 10 from ramp drift (GC-01)</i>	_____	198
<i>Figure 4.18 Section number 45 from transversal drift (GC-02)</i>	_____	204
<i>Figure 4.19 shows the recorded deformation for GC-02 drifts with two weeks gap.</i>	_	212
<i>Figure 4.20 Approximated location of galleries GC-01 and GC-02.</i>	_____	213

List of tables

Table 2.1 <i>Phyllosilicates families, reproduced from (Arabmofrad et al., 2020; Bergaya & Lagaly, 2013; Johnston, 2018; Kotal & Bhowmick, 2015).</i>	70
Table 2.2 <i>BLK360 product specifications (Leica Geosystem).</i>	105
Table 2.3 <i>Three categories of scanning laser (Fuentes, 2010).</i>	109
Table 3.1. <i>Values of geomechanical properties for each lithology.</i>	119
Table 3.2. <i>Geomechanical properties of the potassic group used in the RS2 models.</i>	119
Table 3.3 <i>Correlation between periods and methodologies used.</i>	124
Table 3.4 <i>Analytical techniques applied to samples.</i>	133
Table 3.4. <i>Calculation of paraffin density</i>	141
Table 3.5 <i>Maximum saturation or solubility corresponding to pure NaCl at different temperatures.</i>	143
Table 3.6 <i>Report summary.</i>	156
Table 3.7 <i>The target coordinate list (Y, X, Z).</i>	157
Table 4.1. <i>Average subsidence values with a 90% confidence level and values of the sections assessed</i>	173
Table 4.2 <i>Northern part data of the subsidence basin.</i>	176
Table 4.3 <i>Data used for the calculation of the boundary angle of the southwestern part of the subsidence basin.</i>	177
Table 4.4 <i>Data used for the calculation of the boundary angle of the southern part data of the subsidence basin.</i>	178
Table 4.5 <i>Particle-size distribution of Transformed salt (underlined on tables in light yellow, also it is underlined in light grey the total weight of the sifted sample).</i>	184
Table 4.6 <i>Particle-size distribution of Upper salt</i>	185
Table 4.7 <i>Particle-size distribution of A potash bed.</i>	185
Table 4.8 <i>Particle-size distribution of Intermediate salt.</i>	186
Table 4.9 <i>Results of relative density of salts in paraffin oil</i>	193
Table 4.10. <i>Humidity values.</i>	194
Table 4.11 <i>Natural and dry density for each salt (Intermediated salt, Upper salt, A potash bed and Transformed salt).</i>	195
Table 4.12 <i>Percentage comparison between samples of insoluble particles.</i>	195
Table 4.13 <i>Descriptive statistical analysis of the total measurements of the GC-01 drift.</i>	198
Table 4.14 <i>GC-01 recorded values of the roof corner control point.</i>	198
Table 4.15 <i>Descriptive statistical analysis of the measured values at the roof point of the GC-01 drift.</i>	199
Table 4.16 <i>GC-01 recorded values of the right roof corner control point.</i>	199

<i>Table 4.17 Descriptive statistical analysis of the measured values at the right roof corner point of the GC-01 drift.</i>	200
<i>Table 4.18 recorded values of the left roof corner control point.</i>	200
<i>Table 4.19 Descriptive statistical analysis of the measured values at the left roof corner point of the GC-01 drift.</i>	201
<i>Table 4.20 GC-01 recorded values of the right wall control point.</i>	201
<i>Table 4.21 Descriptive statistical analysis of the measured values at the right wall point of the GC-01 drift.</i>	202
<i>Table 4.22 GC-01 recorded values of the left wall control point.</i>	202
<i>Table 4.23 Descriptive statistical analysis of the measured values at the left wall point of the GC-01 drift.</i>	202
<i>Table 4.24 Convergence evolution using five control points.</i>	203
<i>Table 4.25 Descriptive statistical analysis of the total measurements of the GC-02 drift.</i>	204
<i>Table 4.26 GC-02 roof movements registered by laser scan.</i>	205
<i>Table 4.27 Descriptive statistical analysis of the measured values at the roof point of the GC-02 drift.</i>	205
<i>4.28 Right roof movements registered by laser scan.</i>	206
<i>Table 4.29 Descriptive statistical analysis of the measured values at the right roof corner point of the GC-02 drift.</i>	207
<i>4.30 Left roof movements registered by laser scan.</i>	207
<i>Table 4.31 Descriptive statistical analysis of the measured values at the left roof corner point of the GC-02 drift.</i>	208
<i>Table 4.33 Descriptive statistical analysis of the measured values at the right wall point of the GC-02 drift.</i>	209
<i>Table 4.35 Descriptive statistical analysis of the measured values at the left wall point of the GC-02 drift.</i>	211
<i>Table 4.36 Convergence evolution of five control points.</i>	211

List of equations

<i>Equation 2.1</i>	42
<i>Equation 2.2</i>	43
<i>Equation 2.3</i>	43
<i>Equation 2.4</i>	43
<i>Equation 2.5</i>	43
<i>Equation 2.6</i>	43
<i>Equation 2.7</i>	44
<i>Equation 2.8</i>	45
<i>Equation 2.9</i>	45
<i>Equation 2.10</i>	46
<i>Equation 2.11</i>	46
<i>Equation 2.12</i>	46
<i>Equation 2.13</i>	49
<i>Equation 2.14</i>	50
<i>Equation 2.15</i>	50
<i>Equation 2.16</i>	50
<i>Equation 2.17</i>	51
<i>Equation 2.18</i>	51
<i>Equation 2.19</i>	53
<i>Equation 2.20</i>	53
<i>Equation 2.21</i>	59
<i>Equation 2.22</i>	59
<i>Equation 2.25</i>	60
<i>Equation 2.26</i>	61
<i>Equation 2.27</i>	63
<i>Equation 2.28</i>	64
<i>Equation 2.29</i>	65
<i>Equation 2.30</i>	65
<i>Equation 2.31</i>	65
<i>Equation 2.31</i>	65
<i>Equation 2.32</i>	65
<i>Equation 2.33</i>	66
<i>Equation 2.34</i>	66
<i>Equation 2.35</i>	66
<i>Equation 2.36</i>	66
<i>Equation 2.37</i>	66
<i>Equation 2.38</i>	66
<i>Equation 2.39</i>	67

<i>Equation 2.40</i>	67
<i>Equation 2.41</i>	79
<i>Equation 2.42</i>	82
<i>Equation 2.43</i>	82
<i>Equation 2.44</i>	82
<i>Equation 2.45</i>	82
<i>Equation 2.46</i>	82
<i>Equation 2.47</i>	82
<i>Equation 2.48</i>	85
<i>Equation 2.49</i>	85
<i>Equation 2.50</i>	85
<i>Equation 2.51</i>	87
<i>Equation 2.52</i>	87
<i>Equation 2.53</i>	87
<i>Equation 2.54</i>	91
<i>Equation 2.55</i>	91
<i>Equation 2.56</i>	91
<i>Equation 2.57</i>	91
<i>Equation 2.58</i>	91
<i>Equation 2.59</i>	92
<i>Equation 2.60</i>	92
<i>Equation 2.61</i>	92
<i>Equation 2.62</i>	92
<i>Equation 2.63</i>	95
<i>Equation 2.64</i>	95
<i>Equation 2.65</i>	95
<i>Equation 2.66</i>	95
<i>Equation 2.67</i>	99
<i>Equation 2.68</i>	99
<i>Equation 2.69</i>	100
<i>Equation 2.70</i>	100
<i>Equation 2.71</i>	100
<i>Equation 2.71</i>	101
<i>Equation 2.72</i>	101
<i>Equation 2.73</i>	101
<i>Equation 2.74</i>	101
<i>Equation 2.75</i>	109
<i>Equation 2.76</i>	110
<i>Equation 2.77</i>	110
<i>Equation 2.78</i>	110

<i>Equation 2.79</i>	110
<i>Equation 2.80</i>	111
<i>Equation 3.1</i>	128
<i>Equation 3.2</i>	128
<i>Equation 3.3</i>	128
<i>Equation 3.4</i>	138
<i>Equation 3.5</i>	138
<i>Equation 3.6</i>	140
<i>Equation 3.7</i>	141
<i>Equation 3.8</i>	141
<i>Equation 3.9</i>	141
<i>Equation 3.10</i>	142
<i>Equation 3.11</i>	142
<i>Equation 3.12</i>	142
<i>Equation 3.13</i>	142
<i>Equation 3.14</i>	143
<i>Equation 3.15</i>	143
<i>Equation 3.</i>	143
<i>Equation 3.17</i>	143
<i>Equation 3.18</i>	143
<i>Equation 3.19</i>	143
<i>Equation 3.20</i>	144
<i>Equation 3.21</i>	144
<i>Equation 4.1</i>	187
<i>Equation 4.2</i>	187
<i>Equation 4.3</i>	187
<i>Equation 4.4</i>	187
<i>Equation 4.5</i>	187
<i>Equation 4.6</i>	187
<i>Equation 4.7</i>	187
<i>Equation 4.8</i>	188
<i>Equation 4.9</i>	193
<i>Equation 4.9</i>	193
<i>Equation 4.11</i>	194
<i>Equation 4.12</i>	194
<i>Equation 4.13</i>	194
<i>Equation 4.14</i>	194
<i>Equation 4.15</i>	195
<i>Equation 4.16</i>	195
<i>Equation 4.17</i>	195

Chapter 1

Introduction

Objectives

Hypothesis

“Smile, breathe and go slowly.”— Thich Nhat Hanh

1 Introduction

Potash is an essential nutrient for earth life since, both, animals and plants need it. The name potash is used to refer to a group of various potassium-bearing minerals and chemicals. The most important source for potash is called Sylvite, which is a potassium chloride mineral (KCl) usually found in relatively pure form. It can also be found mixed with halite (NaCl) forming the rock called sylvinite (KCl + NaCl), or it can be found associated with carnallite ($\text{KMgCl}_3 \cdot 6\text{H}_2\text{O}$). The two main industrial potassium ores are Sylvite and Silvinite, while other significant potassium resources are potash sulphate and potash nitrate (USGS, 2022).

The main global producers of potash are Canada, Russia, Belarus, and China. Whereas Germany and Spain are the main producers in Europe, reaching around 10% of the world's supply. The main use of potash is as a fertilizer, representing 90% of the total production (Jasinski, 2021). The main compounds used as fertilizer are potassium chloride (KCl), potassium sulfate (SOP), potassium-magnesium sulfate (SOPM) and potassium muriate (MOP). In addition, potassium ores can have other usages, listed below (Sanz et al., 2022).

- Chemical industry: Potassium nitrate is used to manufacture gunpowder and matches. Moreover, potassium chromate can be used as a red colorant in fireworks. Also, it is used in soap production due to its mildness and because it is more soluble than sodium hydroxide.

- Medical industry: Potassium chloride is used in heart surgery to stop the heart temporarily. Titanyl potassium phosphate (KTP) is used in Nd:YAG laser to treat benign prostate enlargement (BPE).

- Energy industry: In nuclear reactors, sodium and potassium mixture is used as a heat-transfer medium. In addition, molten salts, typically a mixture of sodium nitrate and potassium nitrate can be used to store thermal energy.

- Food industry: Potassium chloride is used as a substitute for salt to control hypertension. Furthermore, Potassium bisulfite is used in alcoholic beverages.

- Animal feed: Potash is used to increase the amount of nutrients of the livestock animals.

- Glass: Potassium carbonate is used in glass manufacturing in order to lower the temperature of melting. Furthermore, it confers clarity to glass, thus is usually used in glassware, Television and computer monitors.

-Other sectors where potash is also used are pharmaceuticals, the detergent industry, bleach and leather treatments, the electromechanical and metallurgy industry, and aluminium recycling processes.

Nowadays, some trials had been done to find substitution options for potash ores, using unconventional potassium resources such as glauconite ($(K, Na)(Fe^{3+}, Al, Mg)_2(Si, Al)_4O_{10}(OH)_2$) sands and potassium feldspars ($K(Si, Al)_4O_8$). However, they have been unsuccessful (European Commission, 2022).

Besides, food demand is expected to increase according to the current increasing tendency of the world population. Therefore, it is expected higher demand for potash production to fertilize all the needed crops. A feasible estimation may be an increase in demand by 13%, from 59.9 Mt K_2O in 2018 to 67.8 Mt K_2O in 2023 (International Fertilizer Association, 2019). Accordingly, there is new mining infrastructure expected to start in years to come (i.e. Canada, Belarus, China, Laos, Spain...). In addition, it is expected the expansion of the existing potash mining infrastructure and capacity to meet this increase.

Overall, it is crucial to ensure a sustainable and responsible extraction of the main deposits, particularly from the European point of view. The case study of this thesis is located in the Catalan Potash Basin (CPB). The CPB is part of the Cardona evaporite formation in the Ebro Valley, Figure 1.1 shows the location of the Ebro basin and the CPB is highlighted in red (Cendón et al., 2003). Currently, only one deposit in the town of Súria is active, despite three other deposits can be found in the CPB, located in the towns of Cardona, Balsareny, and Sallent, respectively, all those located around 75 km from Barcelona. Potash mining is closely related to the province of Barcelona, as it has been developed for the last 100 years. Nowadays, the Súria deposit reaches great depths, from 600 to more than 1000 meters. These depths inevitably entail associated issues, such as high temperatures and in-situ stresses. In these conditions, potash and salt layers have an elastic-plastic behavior, reducing the cross-section of the drifts and their stability. Although the creep mechanism generates a safety problem for rock salt or potash mining, it is not as easy as it could seem to obtain bibliographic references applied directly to a potash ore deposit since there is a lack of knowledge on the creep mechanism applied to the geological field. Therefore, the main motivation of this work is to experimentally investigate the geomechanical behavior of the case study, to increase the available knowledge as well as to improve the conditions of the area affected by the mining infrastructure and the associated subsidence generated.

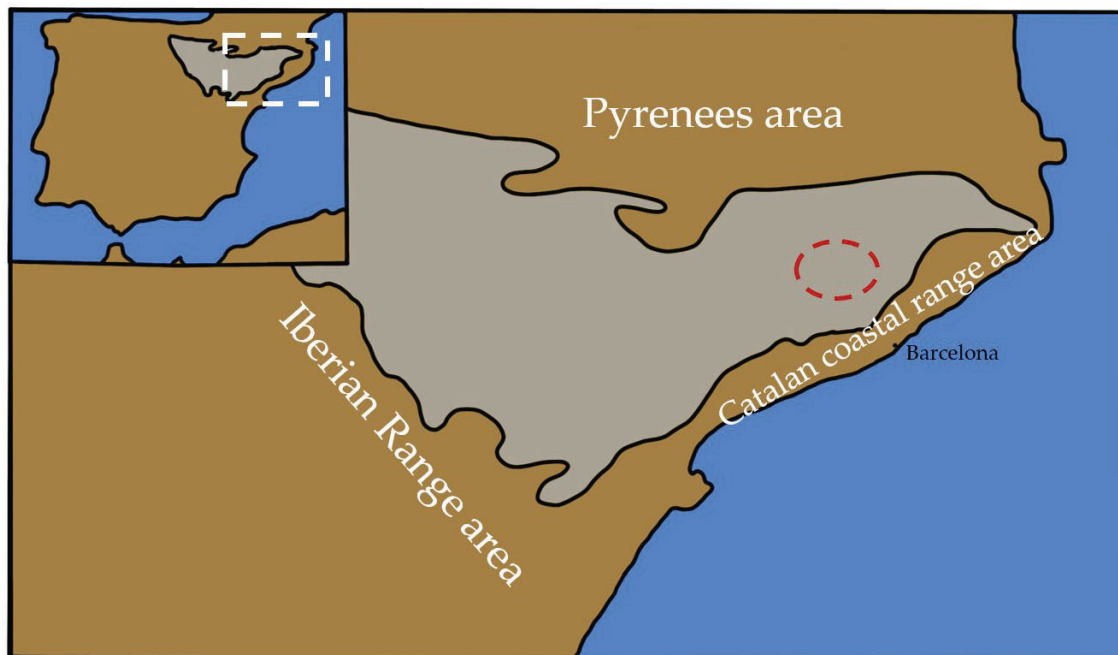


Figure 1.1 Location of the case study. The CPB deposit is highlighted in red.

1.1 Geological structural context

The CPB belongs to the Ebro basin, which extends throughout Catalonia, Aragon and Navarra and it is bounded by the Pyrenees, the Catalan Coastal Range and the Iberian Mountain Range. The Ebro basin has its origin in the depression that during part of the Tertiary was filled by sediments that came from the reliefs that delimited it (López-Blanco et al., 2000). The sediments that filled this basin were mainly gravels, sands, mud and salts, so the rocks and minerals that are currently found in it are conglomerates, sandstones, lutites and evaporites, respectively. The potassic salts are distributed only in the Catalan and Navarra regions, although with greater thicknesses in the Catalan area (Cendón et al., 2003). The sedimentary Ebro Basin is an accumulation of sediments up to 8 km thick, most of which belong to the tertiary age. The basin was formed as a result of the accumulation of marine, detrital and evaporitic sediments in the topographic depression between the Pyrenees, the Iberian range and the Catalan coastal range. 37 million years ago, an inland sea was disconnected from the ocean (García-Castellanos et al., 2003) due to tectonic uplifts in the present-day region of La Rioja. This inland sea gave rise to a huge evaporite endorheic basin. This situation lasted until about 13 and 8 million years ago (Costa et al., 2009). In this period, the lakes had reached an altitude of several hundred meters above sea level due to the accumulation of sediments. This lacustrine system found through the Catalan coastal mountain range an outflow for their waters and, therefore, the system began to drain towards the Mediterranean Sea, forming the current

fluvial network of the Ebro River. Figure 1.2 configures a group of four diagrams intended to illustrate the formation of the Catalan Potash Basin (CPB), which was formed while the Ebro basin was being configured. Since 1960s, several studies have been carried out on the subsoil of the CPB (Ayora et al., 1994b, 1994a, 1995; Cendón et al., 2003; Costa et al., 2009; Garcia-Castellanos et al., 2003; JM, Rios, 1963; López-Blanco et al., 2000; Martínez Garcia et al., 2016; Pueyo Mur, Juan José, 1975; Puigdefàbregas & Souquet, 1986; Rosell & Pueyo, 1997; Rosell Ortiz, L, 1983; Sáez et al., 1991; Schütt, 1998; Taberner et al., 1999; Utrilla et al., 1992; Valentí Masachs, 1962).

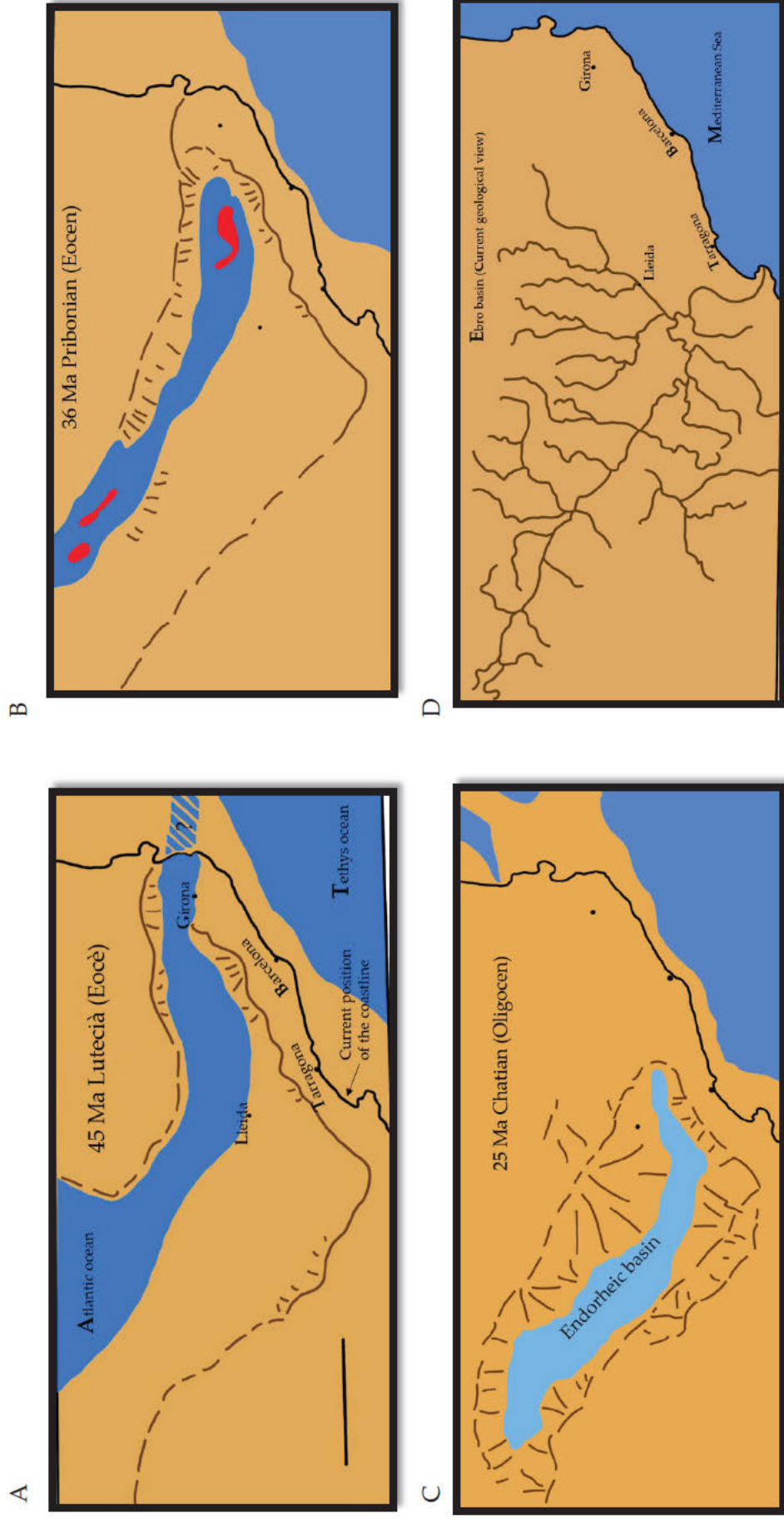


Figure 1.2 Formation of the Ebro Basin and the Catalan Potash Basin (CPB). (Adapted from Geopark scheme).

The C.P.B dates from the Upper Eocene, and the evolution of the basin is related to the uplift of the Pyrenees. Between 42 and 35 million years ago, middle Eocene, when the Ebro basin was filled by marine sediments with continental sediments at the top, the evaporite formation took place at the transition from marine to continental conditions (Cendón et al., 2003; López-Blanco et al., 2000; Taberner et al., 1999). The C.P.B subsoil was formed during the accumulation of sediments, mud and sands in the shallow sea that, at that period of time, it was connected to the Atlantic Ocean. In the south of the region, there were deltas formed by the materials dragged from the mountain range. Coral reefs, with very varied fauna, occupied the areas close to the coast of that warm sea. About 35 million years ago, in the upper Eocene, the sea went restricting until dry, which led to the precipitation of evaporites (salt rock, potash, gypsum, anhydrite, ...) (Ayora et al., 1994, 1995; Cendón et al., 2003; Pueyo Mur, Juan José, 1975). During the beginning of the Oligocene, the C.P.B. was a continental basin with rivers that produced important sedimentation. Because of the terrigenous sedimentation detrital rocks were created, basically the characteristics of reddish sandstones and reddish lutites that characterize the central-western and northern sectors of the area. The forces produced due to the tectonics movement during the alpine orogeny and the different plasticity of the geological materials formed narrow anticlines and several folds, separated by a large and smoother syncline. While the anticlines were forming, the diapiric intrusion started in the nuclei of the underlying evaporites. Nowadays, the diapiric saline formation is only shown in Cardona (Garcia-Castellanos et al., 2003; López-Blanco et al., 2000; Puigdefàbregas & Souquet, 1986; Sáez et al., 1991; Valentí Masachs, 1962).

Diapirs are representative of evaporitic formation. The confined salt can deform plastically under pressure and temperature, becoming a mobile elastic, thereby the salt is forced by the unequal pressures flowing upward through weaker overlying strata. The resulting formation takes a characteristic form of an elongated mushroom and it is made of relatively pure halite (Sanz et al., 2022). Figure 1.3 details a brief explanation of the different stages that led to the formation of the CPB relief as it is known today. Showing a geological section of Súria, from NNW to SSE, with the sequence of materials formed by alternating layers of lutites, red sandstones, limestones and marls. The thickness of these layers varies between a few decimeters and several meters.

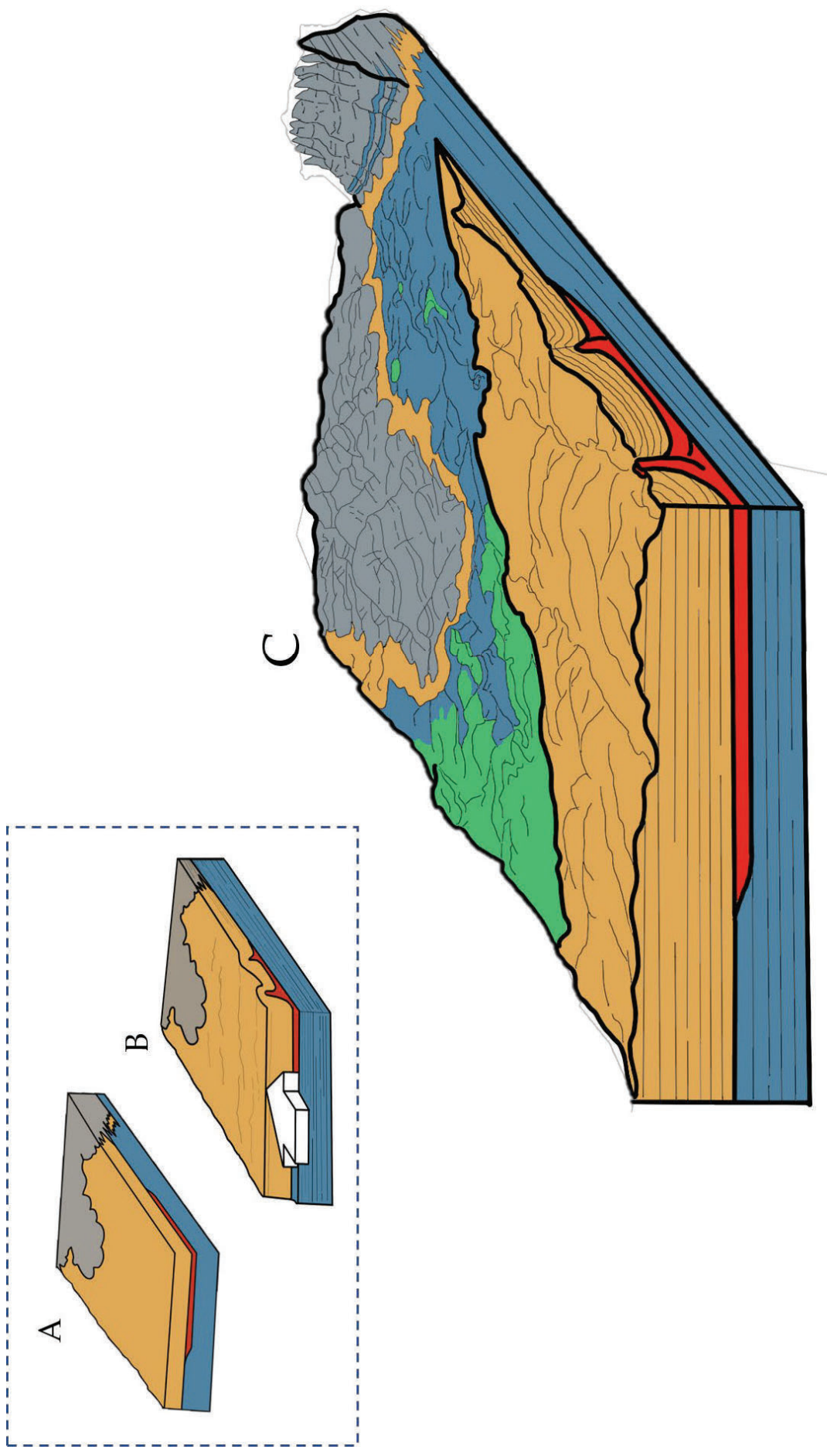


Figure 1.3. Summary of the stages that led to the formation of the current CPB relief. (Adapted from Oms and Biosca, 2011).

The mineralogy of the Catalan potash basin has been defined with the works carried out by different authors (Ayora et al., 1994a, 1994b, 1995; Cendón et al., 2003; Pueyo Mur, Juan José, 1975; Rosell Ortiz, L, 1983). Figure 1.4 describe the different units:

- Basal Anhydrite Unit (BAU); The Basal Anhydrite Unit contains two anhydrite layers, 2 and 9 m thick, respectively, separated by a 2 meters thick marl layer. Both anhydrite layers are made up of an alternation of anhydrite and carbonate laminae.
- Lower Halite Unit (LHU); The Lower Halite Unit consists of 90 m of coarse-grained halite displaying a banded structure. The lower part comprises up to 80 m and it is formed of white-grey halite layers up to 10 cm thick, alternating with darker halite up to 3 cm thick. In the upper 10 m of the LHU, the halite layers are thinner and separated by continuous layers of clay and anhydrite.
- Potash Unit (PU); The Potash Unit consists of a lower Sylvite Member and an upper Carnallite Member. The Sylvite Member is mined for potash and it is made of centimeter-scale cycles. Each cycle is made up of a millimetre-thick clay and sulphate laminae, followed by orange-red halite, similar to that described for the upper LHU, and finally sylvite. The Carnallite Member, with a thickness of 43 m, forms the major part of the Potash Unit. It is made up of carnallite beds with red halite intercalations progressively more abundant upwards. In mine drifts, the uppermost orange-red halite in the Carnallite Member can be up to 35 m thick. Carnallite beds are brecciated or massive and composed of anhedral red crystals of carnallite in a pink matrix. The matrix is a massive aggregate of carnallite with scattered clays, anhydrite and halite. Halite beds in the Carnallite Member are similar to those of the upper LHU and Sylvite Member.
- Upper Halite Unit (UHU); The Upper Halite Unit consists of 3 m of banded halite and anhydrite. A thick and continual formation of conglomerates, sandstones and lutites of continental origin covered the evaporite sequence.

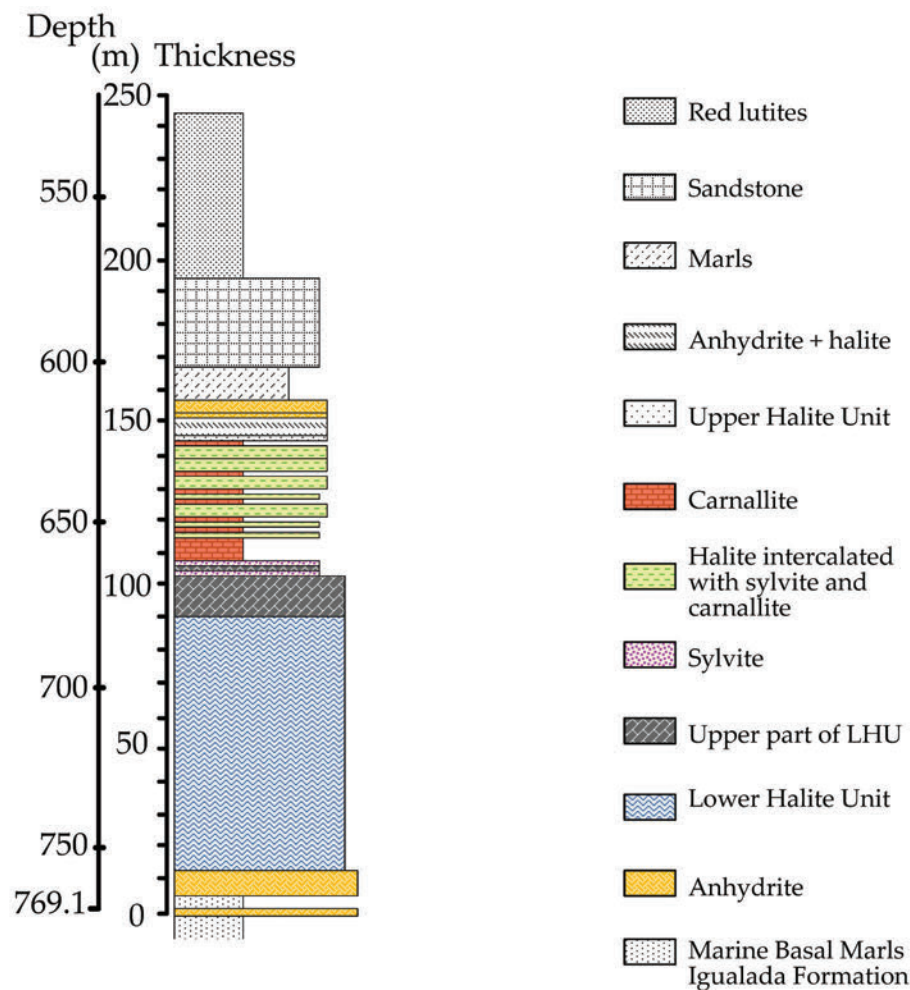


Figure 1.4 Stratigraphic section of the Catalan evaporitic sequence (Adapted from Cendón et al, 2003).

1.2 Local structure

The characteristic relief of the Catalan Potash Basin has been based on the geological structures that conformed it through the geological eras. The majority of these structures are located in the municipalities of Cardona, Súria, Balsareny and Sallent. Following, the main ones are described.

1.2.1 The Mig-món outcrop structure

The outcrop of “the Mig-món” (the half-world), is a geological structure known as the anticline of Balsareny, which is located from the municipality of Balsareny to the mountain range of Castelltallat. The rock layers on both sides of the fold converge in the middle, producing the typical geometry of an anticline. Due to the intensity of this one in the nucleus, the rock layers do not link (Fàbrega et al., 2007). Figure 1.5 shows the geometry of this anticline, where it can be seen that the anticline is asymmetrical, the south flank (on the right) dips more than the

north flank. Figure 1.6 shows a scheme of the outcrop to better illustrate the geological structure. In addition, Figures 1.7 and 1.8 give an overview of the mining area of Súria, where you can see highlighted in purple the distribution of the mining infrastructure (the Cabanasses mining shafts), the anticlinal structure of the Mig-mon outcrop and the urban area.



Figure 1.5 Mig-món anticline outcrop.

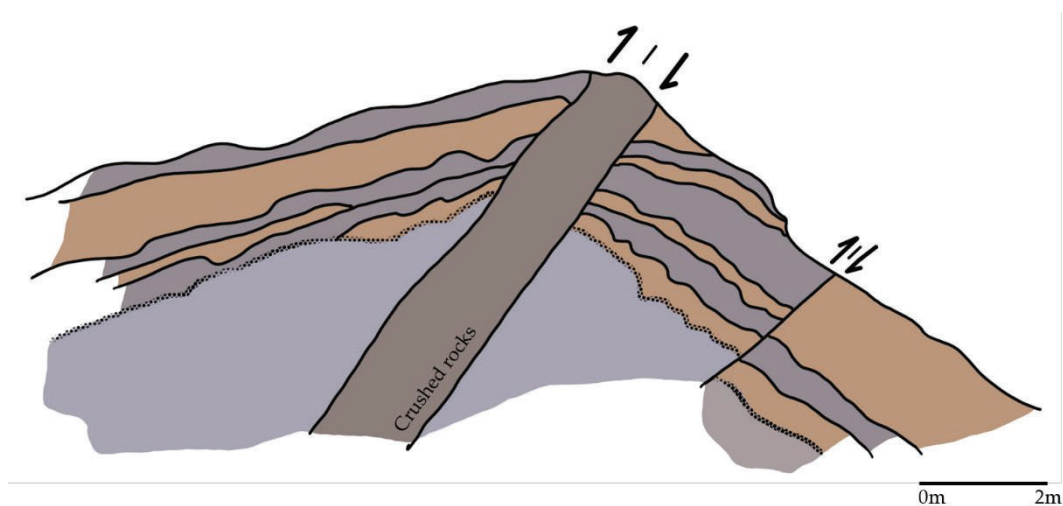


Figure 1.6 Mig-món anticline outcrop scheme (Adapted from Central Catalonia Geopark scheme).



Figure 1.7 Súria municipality, the Cabanasses mine shafts and the Mig-Món outcrop.

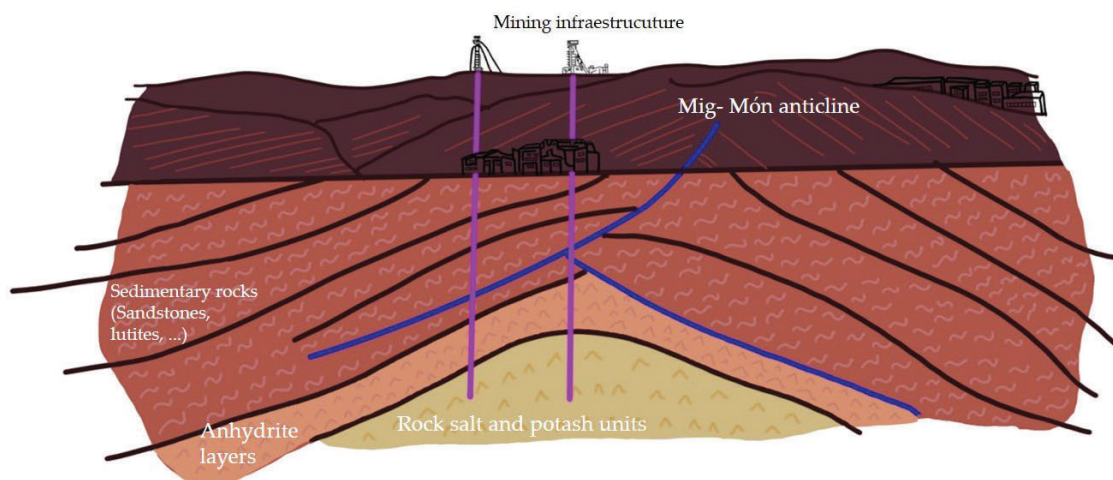


Figure 1.8 Diagram of surface and underground mining infrastructures located in the municipality of Súria (Adapted from Central Catalonia Geopark scheme).

1.2.2 The Sucova structure

The Sucova structure can be seen in Figure 1.9. This outcrop gives us a very deformed view of the Balsareny anticline. The rocks have been placed almost

vertically and form a very closed anticlinal fold (on the right side). On the left side of the Balsareny anticline it is seen another anticline, called the Coaner anticline, much looser and smaller. The stresses on both sides would have originated from the faulted syncline seen in the centre (highlighted with a purple line), blurred due to a strong crushing of the materials. In this location, it can be seen how the sedimentary rocks can behave in a ductile way due to strong deformation before fracturing (Fàbrega et al., 2007).



Figure 1.9 General view of the Sucova structure (Adapted from Fàbrega et al., (2007)).

1.2.3 Tordell's fault

The Tordell's fault forms the NE end of the long Balsareny anticline. The southern block, whose strata are shown crushed and whitish-greyish in color, has been displaced above the strata of the reddish-colored northern block (highlighted using a purple line and orange arrow). Figure 1.10 shows the geological structure of the Tordell's fault.



Figure 1.10 The geological structure of the Tordell's fault.

1.2.4 Sinkholes of Cardaner river valley

In the valley of the Cardener river, the salt is covered only by the sediments of the river itself. Occasionally, in the vicinity of the Tordell's fault, there may be land subsidence or sinkholes caused by the dissolution of gypsum, salt or carnallite, such as those shown in Figures 1.11 and 1.12 (highlighted in purple).



Figure 1.11 Example 1 of Cardaner river valley sinkhole.



Figure 1.12 Example 2 of Cardaner river valley sinkhole.

1.3 Extracting method

The resource is exploited at a depth of around 500 in Vilafruns and 900 meters in Cabanasses, by means of an irregular room and pillar system. Figure 1.13

displays a theoretical system in a horizontal layer and working faces on two different levels. The underground tunnels are placed on two different levels. The exploitation zone is placed in the upper levels. While the service tunnels are at a lower level, which is used to connect the different parts of the mine and a conveyor belt system carries the mineral to the shaft or directly to the surface through a ramp. The mineral transmission between exploitation and service levels is done by a vertical downhole with a length of approximately 30 meters. The exploitation in both mines is done using continuous mining machines, called miners, usually equipped with a transversal head, digging and transmitting the mineral into a truck that carries the burden to the downhole connection levels. Commonly, a loader is used to achieve better mineral transmission between both levels, while there is a transmission system formed by a crusher and a continuous haulage machine attached to the conveyor belt system at the service level. Maintenance of the service tunnel is carried out by smaller miners.

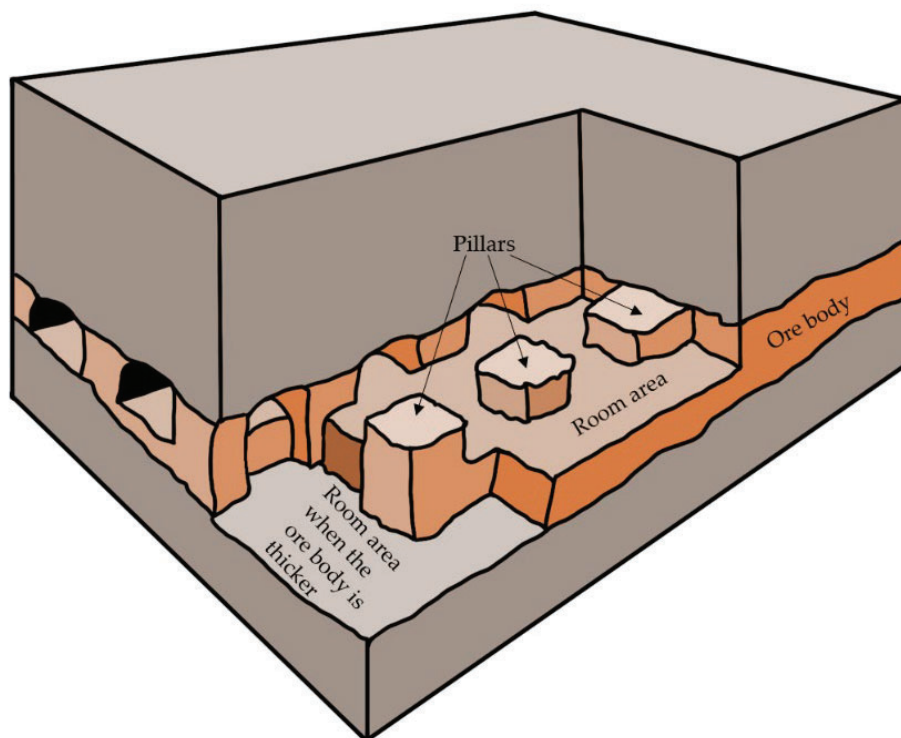


Figure 1.13 Room and Pillar method (Adapted from Hamrin, 1980).

1.4. Objectives

1.4.1 General objectives

The main objective of this study is to approach innovative models that can describe the geomechanical behavior of CPB deposit. Including concern about surface subsidence, high deformations and collapses of underground potash mining, with the ultimate goal of improving the present working conditions and the environmental impacts.

1.4.1.1 Specific objectives

Following, there are the specific goals established in order to achieve the main objective.

- Approach the geomechanical behavior by studying the main geomechanical parameters of each lithology of the CPB deposit.
- Characterize the main parameters of the CPB subsidence basin.
- Improve the current land management and subsidence prediction models of the CPB deposit.
- Carry out the geochemical and textural characterization of the interlayered clays and other insoluble mineralogy.
- Evaluate the influence of different mining and geological parameters on surface subsidence.
- Establish where are located the critical areas and which planes are known to be the most likely to detach and therefore cause accidents.

1.5. Hypothesis and methodology

1.5.1 Hypothesis 1

The creation of a straightforward model that can predict the surface subsidence of the deposit, based on its geomechanical parameters, will provide solutions as well as will improvements in the current mining management.

The combination of the surface subsidence database collected between 2008 to 2021 and the geomechanical parameters of the lithologies, from the Catalan Potash Basin, assessed during 2021, will allow the creation of a model by means of Finite Element Methods (FEM).

The FEM model will improve the current approach to predict surface subsidence, as well as the geomechanical underground behavior. Likewise, creating a suitable tool for underground mining management.

1.5.2 Hypothesis 2

The geochemical characterization and the textural analysis of the interlayered mineralogy between the saline beds, as well as other insoluble mineralogy within them, will improve the health and safety levels of the underground mining infrastructure.

The sampling will be developed in the underground ore deposit. The techniques employed to assess the geochemist characteristics of the samples will be done by means of the XRD technique and the textural analysis by means of SEM-EDS microscope.

The knowledge achieved through the characterization will give a key information to improve the health and safe conditions in the underground infrastructure.

1.5.3 Hypothesis 3

The characterization and evaluation of the surface subsidence basin and the main mining and geological parameters that influence the settlement process will improve land management, and contribute to reducing the current environmental impact.

The surface subsidence basin is going to be characterized by calculating the angle of boundary and distance of influences in all directions (North, South, East and West). This characterization is going to improve surface land management.

Various geological and mining parameters will be evaluated over time in the characterized subsidence basin. This analysis will help to know which are the parameters that influence the subsidence processes over the years, thus helping to reduce the current surface environmental impact.

1.5.4 Hypothesis 4

The application of laser scanner technology for monitoring the stability of underground mine drifts will improve the health and safety of daily production activities in the deposit, reducing the possibility of sudden mine collapses.

Two pilot mining drifts will be monitored weekly for 6 months, to test the possibility of implementing deformation control through laser scanner technology. This application could improve safety in underground mining facilities.

A methodological and periodic control of all mining works, starting with weekly laser acquisitions, would allow detection of the evolution of deformations, as

well as their rate of deformation. Thus, representing key information regarding the prevention of possible unexpected block collapses.

Chapter 2

Literature Review

“Try to learn something about everything and everything about something.” – Thomas Henry Huxley

2. Literature review

2.1 Mechanical concepts

2.1.1 Rheological models and lineal viscoelasticity

Viscoelastic materials have both, elastic (instantaneous deformation) and viscous (deformation depends on time) characteristics.

Lineal Viscoelasticity theory is based on two basic mathematic laws. Firstly, the linearity law, which happens when a function can be graphically represented as a straight line. Moreover, a function is lineal when it satisfies that the image of the sum is equal to the sum of the images (i.e. $f(x+y) = f(x) + f(y)$) and when the image of the multiple of an object is equal to the multiple of the image (i.e. $f(\lambda x) = \lambda f(x)$). Secondly, the superposition property, which states that, for all linear systems, the response caused by two or more inputs is the sum of the responses that would have been caused by each input, individually (i.e. F produces X and G produces Y, then (F+G), will produce the response (X+Y) (Barnes et al., 1989).

Initially, viscoelasticity formulae were based on integral equations. The material response depended not only on the current stress and deformation state but all of its preceding stress and deformation events. With the increasing advance in computational power, the demand for a high memory was limited. However, this inconvenient was solved thanks to the “rheological models”.

Rheological models replace integral equations with differential equations. Therefore, the need to store variables is limited and must be updated at every new time interval. Rheological models for a viscoelastic material are based on a parallel combination or series combination of two mechanical devices, a spring and a dashpot.

The two basic models are the Maxwell model and the Kelvin-Voigt model. In addition, it is known that when the combination is done in series creep requirements are added. However, when the combination is done in parallel, relaxation moduli is added (Mainardi & Spada, 2011).

2.1.1.1 Kelvin-Voigt Model

When a spring is combined in parallel to a dashpot is known as the Kelvin-Voigt model. Figure 2.1 shows a scheme of the Kelvin-Voigt model.

Kelvin-Voigt Equations are expressed in the following equations (Eq. 2.1, 2.2 and 2.3):

$$\sigma(t) = m \epsilon(t) + b_1 \frac{d\epsilon}{dt} \quad \text{Equation 2.1}$$

$$\left\{ \begin{array}{l} J(t) = J_1 \left[1 - e^{\frac{-t}{\tau_\epsilon}} \right], J_1 = \frac{1}{m}, \tau_\epsilon = \frac{b_1}{m} \quad \text{Equation 2.2} \\ G(t) = G_e G_\delta(t), \quad G_e = m, \quad G_{=b_1} \quad \text{Equation 2.3} \end{array} \right.$$

Where τ_ϵ is referred to as the retardation time

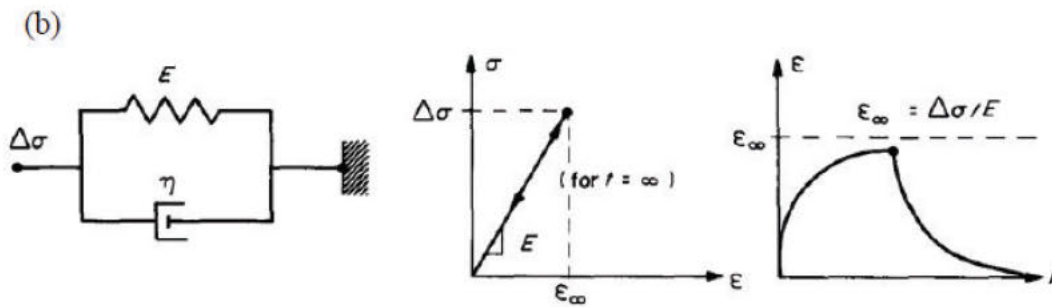


Figure 2.1 Scheme of Kelvin-Voigt model (Dusseault & Fordham, 1993).

2.1.1.2 Maxwell Model

When a spring is combined in series to a dashpot is known as the Maxwell model. Figure 2.2 shows a scheme of the Maxwell model.

Maxwell Equations are expressed in the following equations (Eq. 2.4, 2.5 and 2.6):

$$\sigma(t) + a_1 \frac{d\sigma}{dt} = b_1 \frac{d\epsilon}{dt} \quad \text{Equation 2.4}$$

$$\left\{ \begin{array}{l} J(t) = J_g + J_+ t, \quad J_g = \frac{a_1}{b_1}, \quad J_+ = \frac{1}{b_1} \quad \text{Equation 2.5} \\ G(t) = G_1 e^{\frac{-t}{\tau_\sigma}}, G_1 = \frac{b_1}{a_1}, \quad \tau_\sigma = a_1 \quad \text{Equation 2.6} \end{array} \right.$$

Where τ_σ is referred to as the relaxation time

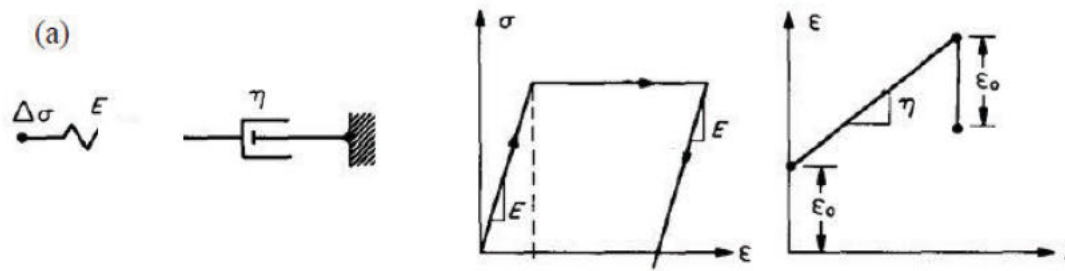


Figure 2.2 Scheme of Maxwell model (Dusseault & Fordham, 1993).

Both models have their limitations. On the one hand, the Maxwell model can properly reproduce elastic deformation, however, it has a limitation with viscous fluency. Therefore, Maxwell's model reproduces viscous fluency as a time-lineal. On the other, the Kelvin-Voigt model cannot reproduce the initial instantaneous elastic deformation.

When both models (Maxwell and Kelvin-Voigt) are mixed in series or parallel, it is possible to obtain various rheological models achieving more realistic solutions.

2.1.1.2.1 Generalized Maxwell or Maxwell-Weichert model

This model can be formed by assembling several Maxwell elements (spring-dashpot segments) in parallel since it considers that the relaxation mechanism occurs in a period of time, not just in a single moment. Therefore, this model can adjust an accurate representation of the mechanism showing as many Maxwell elements as it needs, a scheme can be seen in (Roylance, 2001).

2.1.1.3 Zener or Standard linear solid model

This model was introduced by Zener (1949) bearing the name of Standard Linear Solid. Nowadays it is known by both names (Liu et al., 1976; Zener & Siegel, 1949).

The Zener model is the simplest viscoelastic model. It is obtained by adding a spring in series to the Voigt model or the case of the Maxwell model adding the spring in parallel (Figure 2.3). Therefore, it is added a positive constant, both to the Voigt-like creep requirement and to the Maxwell-like relaxation modulus (Mainardi & Spada, 2011).

Zener Equations are expressed in the following equations (Eq. 2.7, 2.8 and 2.9):

$$\left[1 + a_1 \frac{d}{dt}\right] \sigma(t) = \left[m + b_1 \frac{d}{dt}\right] \epsilon(t) \quad \text{Equation 2.7}$$

And

$$\left\{ \begin{array}{l} J(t) = J_g + J_1 \left[1 - e^{-\frac{t}{\tau_\epsilon}} \right], J_g = \frac{a_1}{b_1}, \quad J_1 = \frac{1}{m} - \frac{a_1}{b_1}, \tau_\epsilon = \frac{b_1}{m} \quad \text{Equation 2.8} \\ G(t) = G_e + G_1 e^{-\frac{t}{\tau_\sigma}}, \quad G_e = m, \quad G_1 = \frac{b_1}{a_1} - m, \tau_\sigma = a_1 \quad \text{Equation 2.9} \end{array} \right.$$

We state the condition $0 < m < b_1/a_1$ in order J_1, G_1 be positive and hence $0 < J_g < J_e < \infty$ and $0 < G_e < G_g < \infty$. As a consequence, we note that, for the Zener or S.L.S model, the retardation time must be greater than the relaxation time, i.e. $0 < \tau_\sigma < \tau_\epsilon < \infty$

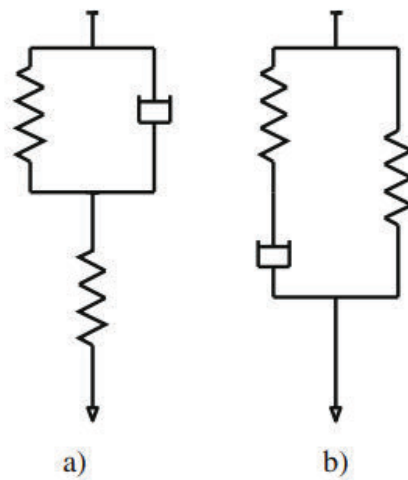


Figure 2.3a, and, b Schemes of Zener model (Mainardi & Spada, 2011).

2.1.1.3.1 Anti-Zener model

This model is obtained by adding a dashpot either in series to the Voigt-Kelvin model or in Parallel to the Maxwell model. Anti-Zener model equations show that this model is obtained by replacing the strain with the strain-rate in Zener equations. This replacement is suitable for fluids. Therefore, this model is also known as Standard Linear Fluid (Mainardi & Spada, 2011).

2.1.1.4 Burgers model

On the one hand, this model can be formed by representing a series combination of a Maxwell element with a Voigt element, supposing that a spring and a dashpot in series represent the creep mechanism. On the other hand, it can be represented by two Maxwell elements in parallel, supposing the spring or a dashpot added in parallel represents the relaxation mechanism, a scheme can be seen in Figure 2.4 (Mainardi & Spada, 2011).

Burgers Equations are expressed in the following equations (Equation 2.10, 2.11 and 2.12):

$$\left[1 + a_1 \frac{d}{dt} + a_2 \frac{d^2}{dt^2}\right] \sigma(t) = \left[b_1 \frac{d}{dt} + b_2 \frac{d^2}{dt^2}\right] \epsilon(t) \quad \text{Equation 2.10}$$

So,

$$J(t) = J_g + J_+ t + J_1 \left(1 - e^{-\frac{t}{\tau_\epsilon}}\right) \quad \text{Equation 2.11}$$

$$G(t) = G_1 e^{-\frac{t}{\tau_{\sigma,1}}} + G_2 e^{-\frac{t}{\tau_{\sigma,2}}} \quad \text{Equation 2.12}$$

J_g, J_+, τ_ϵ and $G_1, \tau_{\sigma,1}, G_2, \tau_{\sigma,2}$ in terms of the four parameters $\{a_1, a_2, b_1, b_2\}$ in the operator equation

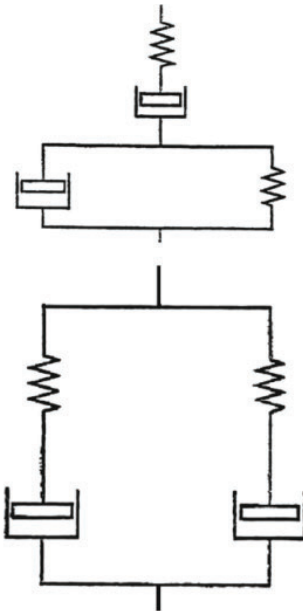


Figure 2.4 Scheme of Burgers model (Mainardi & Spada, 2011).

2.1.2 “Creep”. Fluency concept

Fluency can be described as a deformation over a long time period under constant load. Saline rocks can respond with both, elastic and viscous deformation, this phenomenon can be described as “creep”. (Jeremic, 1994).

Figure 2.5 shows saline creep over a time period. Therefore, the scheme can be distinguished into 3 different stages. The first region shows an instantaneous elastic deformation (ϵ_e), followed by a transitory deformation (First creep). The second region is a stationary stage with a constant gradient (Secondary creep).

Eventually, in the third region, an accelerated fluency leads to failure (Tertiary creep) (Jeremic, 1994).

When the load is removed on point P of the first Region, the deformation falls rapidly to level Q and finally tends asymptotically to zero at point R. The distance PQ is equal to the elastic deformation (ϵ_e). When the load is removed at point T, which is located in the second region, permanent deformation is observed, VO (Jeremic, 1994).

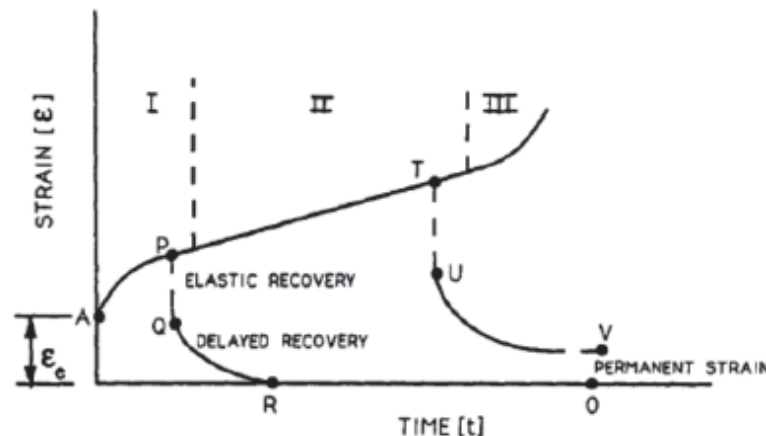


Figure 2.5 Creep curve scheme of a saline rock (Jeremic, 1994).

2.1.3 Discontinuities

Halite is the mineral form of sodium chloride (NaCl), commonly known as rock salt. Halite is a sedimentary mineral. therefore, it can form a monomineral sedimentary rock by precipitation of Sodium Chloride. Rock salt can present impurities such as clays, oxides, etc. these different impurities can give it different colorings from greyish to reddish.

Sylvite is potassium chloride (KCl), has the same origin as halite, and it can be found intercalated with halite in the deposit. Moreover, the mixture of both salts can form a rock named Silvinite. As well as Halite, sylvite can present impurities.

Carnallite is a hydrated potassium magnesium chloride ($\text{KMgCl}_3 \cdot 6(\text{H}_2\text{O})$) and similarly to Halite and sylvite has the same sedimentary origin. It can be found with different colorations from yellow to white or reddish. Carnallite usually presents a massive structure.

Impurities can be found within the salt structure, and moreover forming millimetric layers between salt blocks.

It is believed, that these layers behave as discontinuities. Pictures 2.6 a, b, c, and d has represented the mechanism of Rock block fall.

Figure 2.6 a represents an excavated drift in a saline deposit. Figure 2.6 b, shows how the saline strata begin to detach through the discontinuity. This detachment of strata causes in the contour of the drift the appearance of fractures (encircled). The mechanical behavior of these fractures will be conditioned by the strength parameters of the pre-discontinuity joint, which are the cohesion and the friction angle. When the situation persists, the fracture progresses through the rock matrix (Figure 2.6 c) and finally, the rock block breaks due to the little strength between the massif and it, producing the so-called "Liso fall"(Figure 2.6 d).

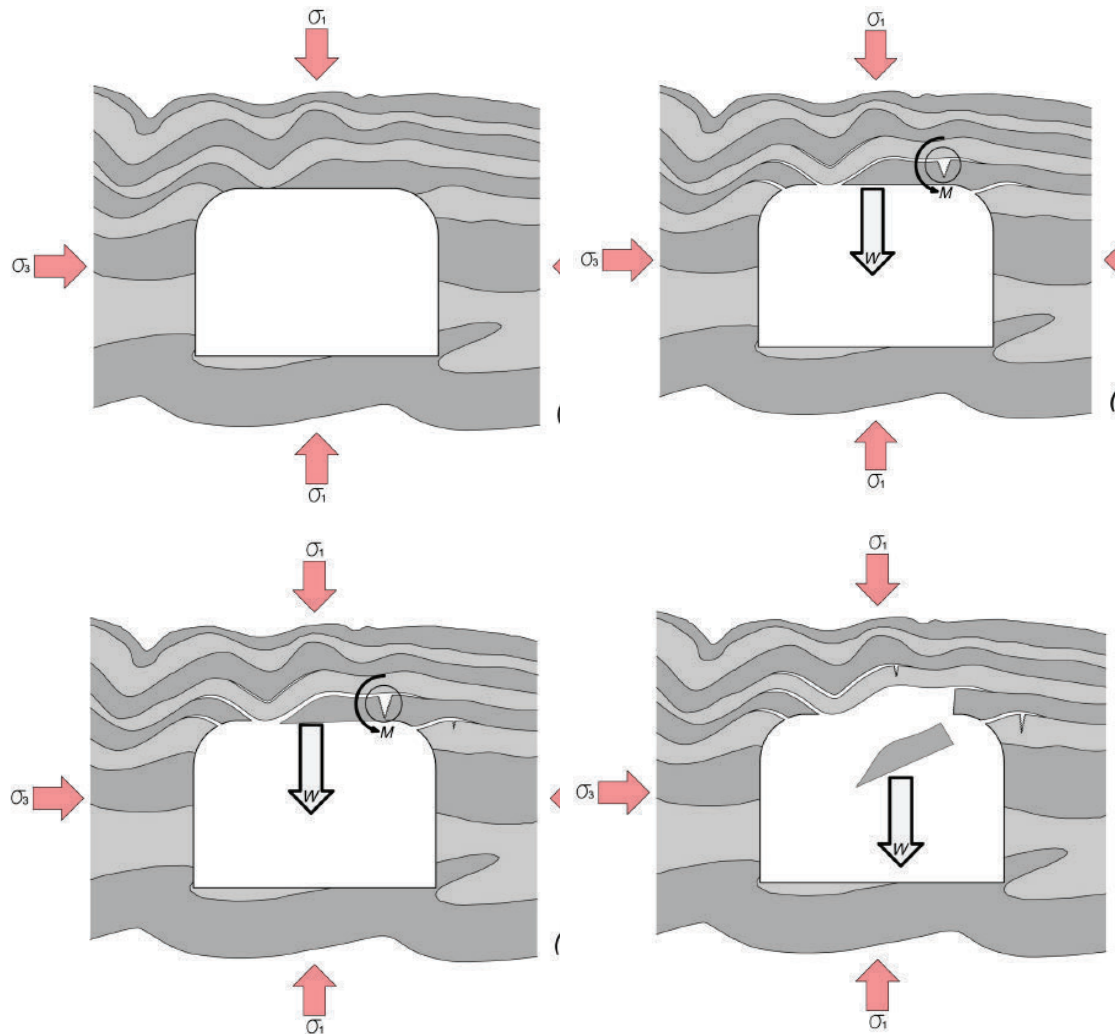


Figure 2.6 a, b, c, d Conceptual model of forming and block fall (Camara Zapata, 2019).

In addition, discontinuities can be classified to estimate the shear strength of discontinuities.

2.1.3.1 Shear strength of discontinuities (Sample's roughness)

All rock masses contain discontinuities such as bedding planes, joints, shear zones and faults. Either in shallow depth or in deep mines, the behavior of a rock

mass is controlled by sliding on the discontinuities, therefore knowing and controlling their behavior is a very important matter. In order to analyze the stability of this system of rock blocks, it is necessary to understand the factors that control the shear strength of the discontinuities which separate the blocks.

According to Hoek (2007), the undulations on a natural joint surface have a significant influence on its shear behavior. Generally, this surface roughness increases the shear strength of the surface, and this strength increase is extremely important in terms of the stability of excavations in rock. Patton (1966) demonstrated this influence by means of an experiment in which he carried out shear tests on 'saw-tooth' specimens such as the one illustrated in Figure 2.7. Shear displacement in these specimens occurs as a result of the surfaces moving up the inclined faces, causing dilation (an increase in volume) of the specimen. The shear strength of Patton's saw-tooth specimens can be represented by Equation 2.13:

$$\tau = \sigma_n \tan(\phi_b + i) \quad \text{Equation 2.13}$$

Where ϕ_b is the basic friction angle of the surface and i is the angle of the saw-tooth face.

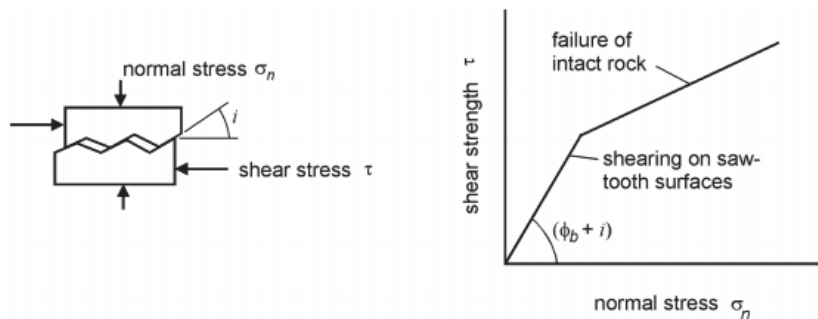


Figure 2.7 Patton's experiment on the shear strength of saw tooth specimens (Hoek, 2007).

According to Hoek (2007), Equation (13) is valid at low normal stresses, where shear displacement is due to sliding along the inclined surfaces. At higher normal stresses, the strength of the intact material will be exceeded and the teeth will tend to break off, resulting in a shear strength behavior which is more closely related to the intact material strength than to the frictional characteristics of the surfaces.

Patton's experiment does not reflect the reality that changes in shear strength with increasing normal stress is gradual rather than abrupt. Barton (1973 and

1976) studied the behavior of natural rock joints and the proposed Equation 2.13 could be re-written as Equation 2.14:

$$\tau = \sigma_n \tan \left(\phi_b + JRC \log_{10} \left(\frac{JCS}{\sigma_n} \right) \right) \quad \text{Equation 2.14}$$

Where; JRC is the joint roughness coefficient and

JCS is the joint wall compressive strength.

Barton (1973) developed his first non-linear strength criterion for rock joints, using the basic friction angle ϕ_b , from analysis of joint strength data reported in the literature. Barton and Choubey (1977), on the basis of their direct shear test results for 130 samples of variably weathered rock joints, revised equation 2.14 to equation 2.15.

$$\tau = \sigma_n \tan \left(\phi_r + JRC \log_{10} \left(\frac{JCS}{\sigma_n} \right) \right) \quad \text{Equation 2.15}$$

Where; ϕ_r is the residual friction angle

Barton and Choubey (1977) suggest that ϕ_r can be estimated from equation 2.16

$$\phi_r = (\phi_b - 20) + 20 \left(\frac{r}{R} \right) \quad \text{Equation 2.16}$$

where r is the Schmidt rebound number on wet and weathered fracture surfaces and R is the Schmidt rebound number on dry unweathered sawn surfaces.

Equations 15 and 16 have become part of the Barton-Bandis criterion for rock joint strength and deformability (N. Barton & Bandis, 1982). According to Hoek (2007) the joint roughness coefficient JRC is a number that can be estimated by comparing the appearance of a discontinuity surface with standard profiles. One of the most useful of these profile sets was published by Barton and Choubey, (1977) and is reproduced in Figure 2.8. The appearance of the discontinuity surface is compared visually with the profiles shown and the JRC value corresponding to the profile which most closely matches that of the discontinuity surface is chosen. In the case of small-scale laboratory specimens, the scale of the surface roughness will be approximately the same as that of the profiles illustrated. However, in the field, the length of the surface of interest may be several meters or even tens of meters and the JRC value must be estimated for the full-scale surface. On the basis of extensive testing of joints, joint replicas (N.

Barton & Bandis, 1982) proposed the scale corrections for JRC defined by the following relationship (Eq. 2.17):

$$JRC_n = JRC_o \left(\frac{L_n}{L_o}\right)^{-0,02JRC_o} \quad \text{Equation 2.17}$$

where JRC_o , and L_o (length) refer to 100 mm laboratory scale samples and JRC_n , and L_n refers to in situ block sizes. Because of the greater possibility of weaknesses in a large surface, it is likely that the average joint wall compressive strength (JCS) decreases with increasing scale. Barton and Bandis (1982) proposed the scale corrections for JCS defined by the following relationship (Eq. 2.18):

$$JCS_n = JCS_o \left(\frac{L_n}{L_o}\right)^{-0,03JRC_o} \quad \text{Equation 2.18}$$

Where JCS_o and L_o (length) refers to 100 mm laboratory scale samples and JCS_n and L_n refer to in situ block sizes.

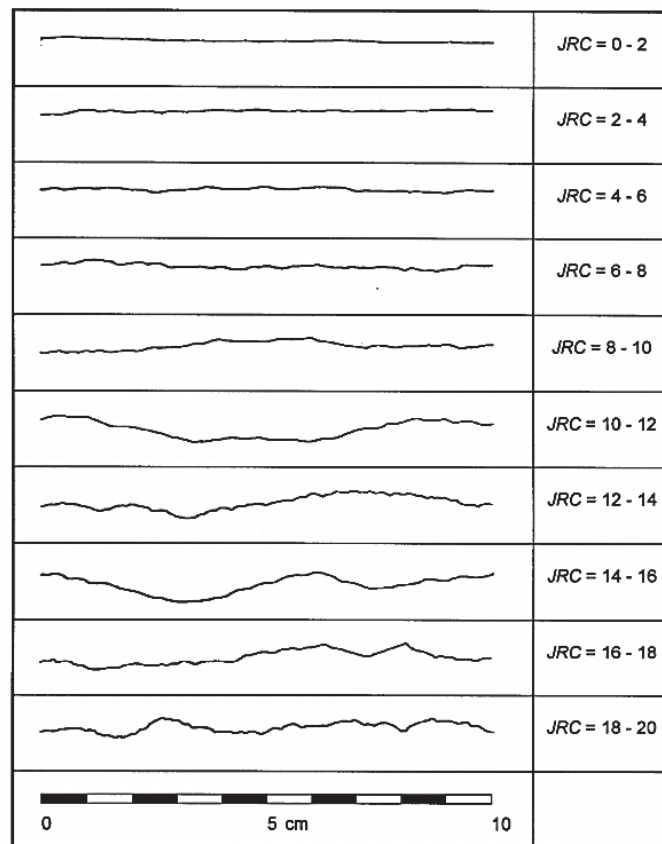


Figure 2.8 Roughness profiles and corresponding JRC values (N. Barton & Choubey, 1977).

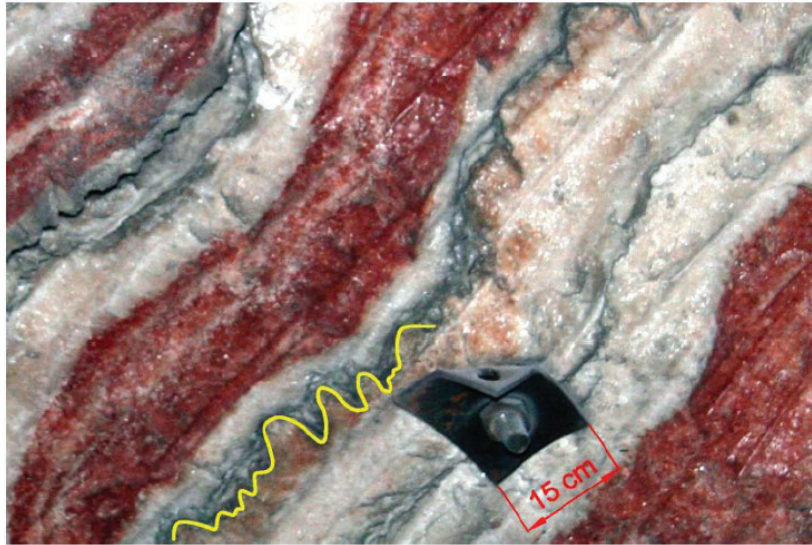


Figure 2.9 Example of high rough discontinuity in Cabanasses ore deposit (Camara, 2019).

2.1.4 Rock masses classifications

Discontinuities also have an essential role in the case of rock mass classification systems that are used for engineering design and stability analysis. They are based on empirical relationships between rock mass parameters and engineering applications (i.e. tunnels, mining infrastructure, and slopes, among others). Different classifications can be distinguished, the most commonly used being the Rock Mass Classification (RMR) and the Q-system.

2.1.4.1 Rock mass rating classification

The Bieniawski geomechanical classification, also known as Rock Mass Rating (RMR), is a geomechanical classification system developed by Bieniawski in 1973 and successively modified in 1976, 1979, 1984 and 1989 (Bieniawski, 1973, 1989, 1993, 1979).

It provides a classification of a rock mass "in situ" based on five parameters: Unaltered rock strength (uniaxial compression), Rock Quality Designation (RQD), joint spacing, joint condition and groundwater conditions. Values for these parameters are assigned according to tables. The values for these parameters are assigned according to tables, and when added together, the RMR quality index is obtained. Then, based on the orientation of the discontinuities, a correction factor must be applied. The adjustment factor has different values depending on the infrastructure to be applied (i.e. tunnels, foundations or embankments.) (Bieniawski, 1993; Lawson & Bieniawski, 2013).

2.1.4.2 Q-system

The Q system of rock mass classification, which expresses the quality of the rock mass based on a value called Q (Eq. 2.19), was developed by Barton, Lien and Lunde (Barton, 2002; Barton et al., 1974).

The value Q is defined with the following equation:

$$Q = \frac{RQD}{J_n} \times \frac{J_r}{J_a} \times \frac{J_w}{SRF} \quad \text{Equation 2.19}$$

$$RQD = \left(\frac{l_{\text{sum of length of core pieces} > 100\text{mm}}}{l_{\text{total core run}}} \right) \times 100\% \quad \text{Equation 2.20}$$

Where RQD is the Rock Quality Designation and measures the grade of a rock mass based on drill core (Eq. 2.20). The J_n is the rate of diaclases, similarly to the RQD, indicates the degree of fracturing of the rock massif. J_r is the roughness index of discontinuities and J_a is the alteration index of these discontinuities. Therefore, J_r/J_a is the shear strength between blocks. The J_w is the reduction factor for the presence of water and the SRF is the index for the stress state of the rock mass. J_r/SRF is the influence of the stress state.

2.1.5 Crystal structure. Grain size

Halite forms isometric crystals with sizes from millimetric to decimetric in size. Within its crystal structure it can be found some impurities, such as secondary minerals, solid solutions, vapor or fluids inclusions, pores or grain boundaries, (Urai & Spiers, 2017). These impurities give to halite different coloration since on pure state is transparent.

Figure 2.10, shows a microstructure sample from Asse II (Germany), where it can be extensively studied common size ranges, crystal morphologies and detecting several inclusions of brine (Spiers et al., 1986).

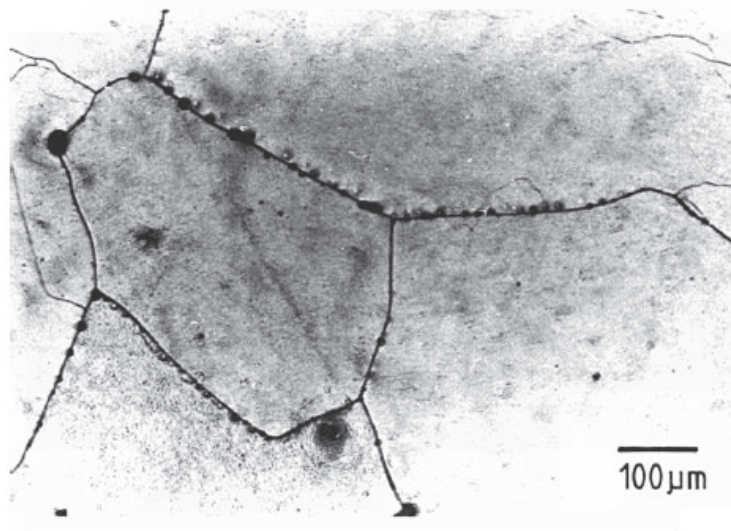


Figure 2.10 Polycrystalline halite structure with fluid inclusions and grain boundaries (Spiers et al., 1986).

Figure 2.11 shows how the decrease in grain size leads to an increase in creep deformation. Several creep compaction tests were carried out with grounded pure halite samples in the presence of saturated brine. Different particle sizes samples (98, 196 and 275 μm) were performed (Spiers et al., 1990).

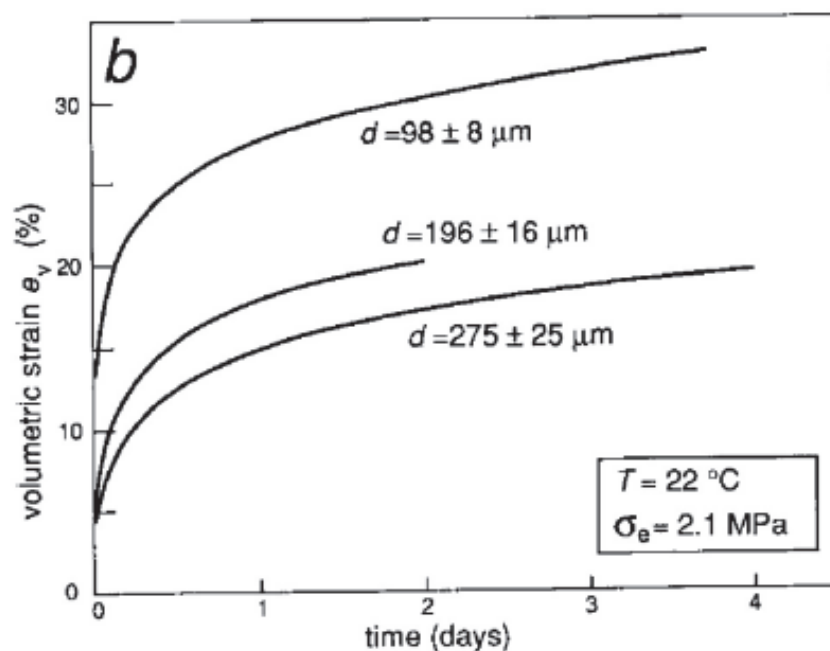


Figure 2.11 Grain size influence in creep compaction curves in brine saturated samples (Spiers et al., 1990).

2.2 Rehology: Salt deformation mechanisms

The knowledge of mechanical salt behavior is essential due to its physical properties such as high permeability, and viscoplastic behavior. Its properties must be controlled since salt can be highly deformed. The mechanical behavior of salt is linked to thermal processes and chemical and hydraulic environments (Figure 2.12).

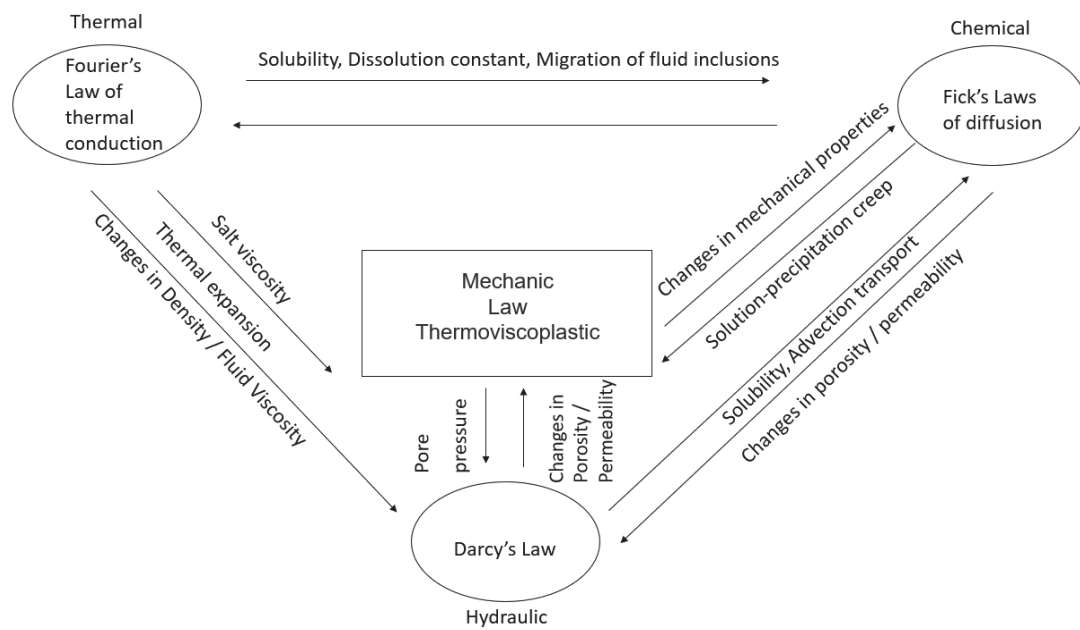


Figure 2.12 Characteristic processes and mechanisms of saline materials.

Modified from (Barberán, 2000).

Under deviatoric stress, salt rocks can be deformed by a range of processes. The deformation mechanisms known to operate at temperatures relevant to engineering and natural halokinetic conditions (20-200 °C) are summarized in Figure 2.13 (Urai et al., 2008).

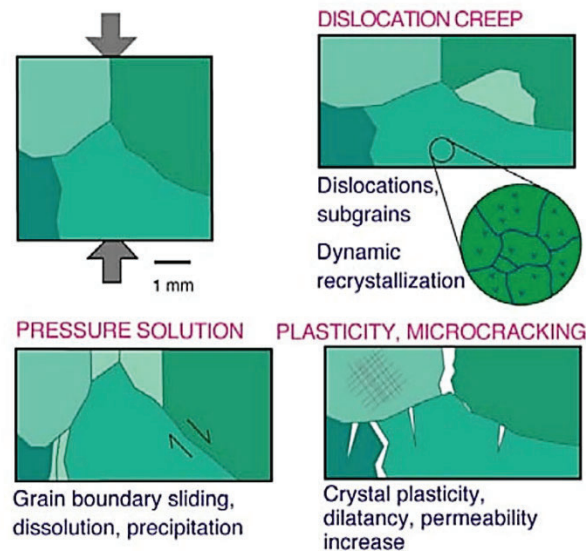


Figure 2.13 Schematic drawing of the microstructural processes that can operate during deformation of halite at temperatures in the range 20-200°C. Different shades of green represent crystals with different orientations (Urai et al., 2008).

The halokinesis term refers to all those processes that are connected with the movements of salt under the influence of gravity. Furthermore, the term halotectonics covers all those processes where compressive tectonic forces are also involved (Trusheim, 1960).

These processes can be developed because salt density and strength do not increase with burial, usually took place in large and thick salt basins and have great practical importance mainly for the oil, rock salt, and potash industries (Trusheim, 1960).

About 100 evaporite basins have been affected by salt tectonics, some examples can be found in cratonic basins (i.e. Zechstein or Pricaspian), synrift basins (i.e. Hormuz Zagros or Maritime Canada), late synrift or postrift passive margins (i.e. Gulf of Mexico) or in continental collision zones and foreland basins (i.e. Gachsaran or Ebro Basin) (Roberts & Bally, 2012).

In addition, temperature is an important factor to evaluate the deformation of salt, since a thermal increase causes a decrease in viscosity. By using a deformation map physical conditions can be illustrated. A deformation map usually plots temperature versus differential stress and can be distinguished by five categories of deformation mechanisms. (1) microfracturing, cataclasis, and frictional sliding; (2) mechanical twinning and kinking; (3) diffusion creep; (4) dissolution creep and (5) dislocation creep. These mechanisms are usually helped by other important mechanisms, such as recrystallization, that cause less-strained lattices (Davis et al., 2011). (Davis et al, 1996).

Microfracturing, cataclasis, and frictional sliding produce the formation and flow of totally fractured or pulverized rock and crystal fragments, by involving the formation, lengthening, and interconnecting of microcracks by frictional sliding along grain boundaries or microcracks (Davis et al., 2011).

Mechanical twinning and kinking are two types of deformation less aggressive than Microfracturing, cataclasis, and frictional sliding. Deformation occurs by bending, not by breaking the crystal lattice (Davis et al., 2011).

Several types of creep can be identified according to Figure 2.14. Each type of creep employs a particular strategy in order to change the shape and size of crystals as a response to directed stress (Davis et al., 2011).

Diffusion creep changes the shape and size of crystals by way of the vacancy movement and atoms within crystals and along grain boundaries. Dissolution creep changes the shape and size of crystals by dissolving material from one site and reprecipitating the material in another site, helped by fluids along grain boundaries or within pore spaces. Dislocation creep operates through an intercrystalline slip of the lattice structure (Davis et al., 2011).

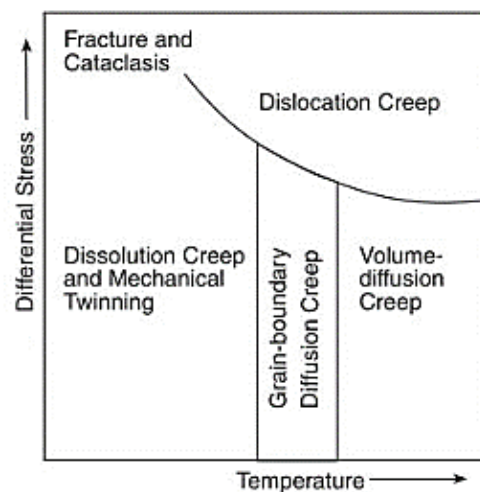


Figure 2.14 Simplified deformation map, showing the general conditions where each deformation mechanism dominates relative to one another (Davis et al., 2011).

The deformation by compaction creep is a behavior that has been studied over the years. One of the most rigorous studies is the one published by (Spiers et al., 1990). The viscoplastic creep behavior of compacted salt can be influenced by the effects of brine, causing a dissolution/precipitation, mixed with a fluid-assisted diffusional creep process (FADC). Furthermore, other studies have been focused on the hydromechanical properties of compacted salt, during long periods of time, and using numerical models (Olivella et al., 1994). Compaction creep (DC)

and resistance tests are the most common tests in order to determine the mechanical properties of saline materials. The compaction creep process can be affected by different parameters such as; impurities like clays or anhydrite, the grain size, the grain size distribution, the humidity, the initial and final pore index, stress state, the force ratio or the temperature.

Five are material dependent parameters, and three are externally controlled variables. These parameters have been studied by various authors. In the case of humidity (Spiers et al., 1990) the content of impurities was studied in Aydin and Johnson (1983), temperature (Spiers et al., 1990) and grain size and its distribution (Spiers et al., 1990). The effect of stress state, time and porosity was also studied in all the previous studies.

Humidity is one of the main properties that affect the mechanical behavior of the saline material. It should be specified, all the water within the mineral is considered brine. The humidity can modify the following effects; its effects on the initial void ratio initial humidity content, Long-term compaction creep rates, and the moisture content and the development of pore pressure. The humidity content is an important factor in the process of compaction creep. Wet salts are more compactable quicker than dried salts. (Spiers et al., 1990).

Many studies have examined the possibility of pore pressure development in compacted granular salt. For pore pressures to develop, the humidity must become impeded and the pore fluid must become compressed. Studies that have been done in the last years (Spiers et al., 1990) show the viscoplastic creep behavior of compacted granular salt, which can be influenced by the presence of brine as a fluid-assisted recrystallization and diffusional creep process. However, the mechanisms are not clearly defined yet.

The grain size is a parameter with great influence on the behavior of compaction creep rate. According to (Spiers et al., 1990) the process of compaction creep rates for low stress (<4MPa) is proportional to $1 / d^3$ (d is the grain size), for high stresses (≈ 8 MPa), this relationship is proportional to $1 / d^2$.

On the other hand, the behavior of the material with 30% or more impurities such as clays or anhydrite is dominated by the impurity's properties.

Finally, there is evidence that an increase in temperature results in a decrease in the compaction of the material (Spiers et al., 1990). On the other hand, it is known that creep rates in intact salt are sensitive to even small changes in temperature. In contrast with other types of rocks, saline rocks show creep deformation at room temperature.

The difference in sensitivity to temperature of intact versus granular salt material reflects the activation energies of the dominant mechanisms involved in their deformation.

2.2.1 Rheological equations for rock salt

Mechanically, rock salt is as strong as ordinary concrete in the short term but it is weak and ductile in the long term. These strength properties are desirable for mine and cavern construction, for healing discontinuities and for sealing engineered openings. These flow (creep) properties of rock salt are of fundamental importance. Steady-state flow properties are crucial to both concerns and transient flow properties are especially important in model predictions of the closure characteristics, stability and behaviour of underground openings (Carter et al., 1993). Rheology is a branch of physics, and it is the science that deals with the deformation and flow of materials, both solids and liquids (Schowalter, 1978). The rheology of a given crystalline material depends on the dominant deformation mechanism, which in turn depends on the time scale and hence deformation rate of interest. Many studies have been published on halite. According to (Urai et al., 2008) and considering steady state, non-dilatant deformation, the main classes of equations for the creep strain rate of halite are (Eq. 2.19, 2.20 and 2.21):

For dislocation creep:

$$\dot{\epsilon}_{DC} = A \exp\left(\frac{-Q_{DC}}{RT}\right) (\sigma_1 - \sigma_3)^n \quad \text{Equation 2.21}$$

For solution-precipitation creep:

$$\dot{\epsilon}_{PS} = B \exp\left(\frac{-Q_{PS}}{RT}\right) \left(\frac{\sigma_1 - \sigma_3}{TD^m}\right) \quad \text{Equation 2.22}$$

And finally, the total strain rate is the sum of the two

$$\dot{\epsilon} = \dot{\epsilon}_{DC} + \dot{\epsilon}_{PS} \quad \text{Equation 2.23}$$

In these equations, written in a form appropriate for axially symmetric compressive deformation, A and B are material parameters, Q_{DC} and Q_{PS} represent (apparent) activation energies for dislocation and pressure solution creep, R is the gas constant, T is absolute temperature, σ_1 and σ_3 are the maximum and minimum principal compressive stresses, D is grain size, and n and m are the exponents of stress and grain size respectively. Two important differences between equations 19 and 20 are firstly the dependence of strain rate on stress (n = 1 for solution-precipitation creep or pressure solution while n > 1 for DC creep, see Figure 2.15) and secondly the dependence of strain rate on grain size (Urai et al., 2008).

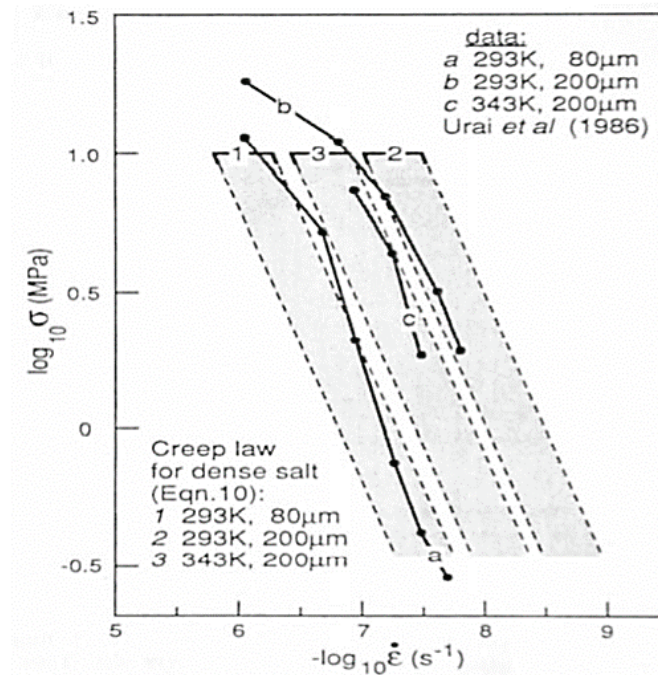


Figure 2.15 Steady state strain rate data of fine-grained wet halite samples deforming by solution- precipitation processes, showing a stress exponent n close to 1. Gray bands represent the theoretical flow law for this process (Spiers et al., 1990).

At differential stresses below 15-20 MPa and strain rates below 10^{-6} s^{-1} , both, uniaxial and triaxial experiments on natural and synthetic rock salt show power law dislocation creep behavior, with a stress exponent n of 5-6 at the higher stresses and 3.5-4.5 at lower stresses (Hunsche & Hampel, 1999). The rate of dislocation creep can vary by approximately three orders of magnitude, caused by differences in concentration of impurities in solid solution, amount and distribution of secondary mineral phases, grain size, subgrain size, dislocation density and fluids in grain boundaries (Urai et al., 2008).

2.2.2 Mechanical behavior of saline materials: transport fluid properties and associated microstructures

2.2.2.1 Creep in granular halite (vapor-liquid graphic)

Compaction creep mechanisms of granular salt materials are closely related to the time-dependent behavior of salt rocks. The first creep laws were developed to describe time-dependent deformations in metals, rubber and glass, under constant tresses, presenting a logarithmic creep law (Eq. 2.25).

$$\frac{\partial \epsilon}{\partial t} = Bt^{-1} \tag{Equation 2.25}$$

Where:

$\frac{\partial \varepsilon}{\partial t}$ Strain/Deformation of the fluid circulation

B Laboratory constant

t Time

Numerous other creep laws have been proposed to describe the strain rate/deformation. Nowadays, the most commonly accepted law describing steady state creep is a power/exponential combination which considers both stress and temperature dependent phenomena, as follows (Eq. 2.26):

$$\frac{\partial \varepsilon}{\partial t} = A \sigma^n \exp\left(-\frac{\Delta H}{RT}\right) \quad \text{Equation 2.26}$$

Where:

$\frac{\partial \varepsilon}{\partial t}$ strain rate

A laboratory constant

σ principal stress difference ($\sigma_1 - \sigma_3$)

n slope of $\log(\partial \varepsilon / (\partial t)) / \log \sigma$ graphed

ΔH Activation energy required to activate the mechanism

R Gas constant (Universal gas constant)

T Temperature in Kelvin degree

Equations of the above form can be used to describe steady state deformations by a single mechanism.

The four mechanisms of strain for saline materials are; Dislocation climb, and dislocation glide; Diffusion mechanisms, including porosity and grain boundary; Sliding between grains; Cataclasis. Figure 2.16 shows the relation between temperature/temperature melting and strain/deformation, which is caused by different mechanisms. Depending on the temperature and the stress level, the strain/deformation is caused by two different mechanisms.

Glide and climb (low and high temperatures), this mechanism is connected to the theory of Dislocation. These mechanisms usually occur in intercrystalline mechanisms. For high temperatures (T / T_m where $T_m \approx 800^\circ\text{C}$ is the melting point) would occur cases of diffusion mechanisms. For low stresses and temperatures, the most important strain mechanism is based on diffusion aided by fluid (fluid-assisted diffusional creep). Diffusion can occur between the crystal lattice (diffusion vacancy or Nabarro-Herring creep) or along the boundaries of the grain (Coble creep). The salt grains are dissolved at high stress values (grain contact) and precipitate at low stress values (pores) (Spiers et al, 1990).

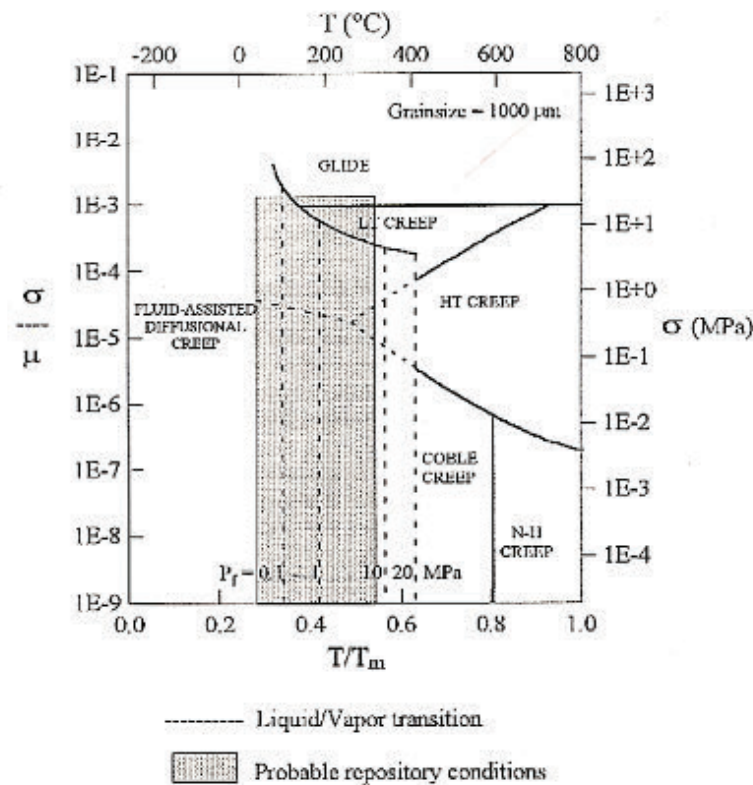


Figure 2.16 Strain/Deformation mechanism of saline material. Fluid pressure P between (0.1 to 20 MPa). σ deviatoric force, μ Elastic modulus, T Temperature, and T_m Melting Point/Temperature (Spiers et al., 1990).

The sliding between grain boundaries is a process where the change occurs in the shape of the adjacent crystals caused by diffusion and dislocation processes. The strain/deformation for each of the mechanisms (except for cataclastic) has a characteristic gradient (equation 23).

The range of every mechanism depends on the conditions of different stress and temperatures. A single mechanism law cannot adequately describe the behavior of salt over all the ranges of temperature and pressure conditions.

Although under compaction, the pressure could be the most important strain/deformation mechanism for saline materials, this mechanism needs to be accompanied by sliding in the contact boundaries in order to rearrange the grains during deformation. Granular salt has porosity, which allows the mobility of particles, where the sliding between grains takes on an important role in compaction.

2.2.2.2 Fluid transport in salts

The fluid transport in the salts is due to its high solubility in the water, the fluid present in compacted granular salt, subjected to transport is brine. Brine is present in this porous medium in two ways: brine-filled intragranular inclusions,

brine-filled pores on grain boundaries, and some hydrated minerals. Water could also be present in compacted granular salt as a part of some hydrated minerals due to the effect of the differential pressure gradient and under the effect of the pressure and temperature gradient.

2.2.2.3 Brine migration

Three mechanisms proposed for explaining the phenomenon of brine migration are (a) Motion of the brine inclusions by a temperature gradient, (b) Vapor-phase transport along connected porosity (c) Liquid transport driven by a stress gradient in the salt.

Brine-inclusion motion by temperature gradient; is the most studied theory and the most widely accepted mechanism. The equation was proposed by (Olander, 1980) (Eq. 2.27).

$$v = \frac{DC_s^{sat}}{\rho_s} \left[\left(\frac{(C_s^{sat})^{-1} dC_s^{sat}}{dT - S_0} \right) \nabla T - \left(\frac{\delta_h + \delta_c}{L} \right) \right] \quad \text{Equation 2.27}$$

Where:

v speed (cm/s) inclusion velocity

D Salt diffusion in brine (cm²/s)

C_s^{sat} medium salt concentration (mol/cm³) average salt concentration in the inclusion

ρ_s density of the saline solid (mol/cm³) density of the solid salt

S_0 Empirical coefficient (°C⁻¹)

∇T Gradient of brine temperature (°C/cm) temperature gradient in the brine

δ_h Unsaturated fraction of hot side fractional undersaturation at hot face

δ_c Unsaturated fraction of cold side fractional oversaturation at cold face

L Length of the termic gradient (cm) dimension of the thermal gradient

The first term represents the diffusion of salt within the brine, the second one represents the rate kinetics index of dissolution and crystallization each one respectively on the hot and cold faces. Although there is some variability in the velocity of the brine inclusions within crystals, the major uncertainty is their behavior on encountering a grain boundary. According to the theoretical and experimental analysis, the movements in these zones are slower. The brine is deposited at the boundary grain producing a porosity connection.

2.2.2.4 Vapor phase transport within the connected porosity

The transport of the vapor of brine is produced by water vapor that connects the porosity in salt. The potential gradient is the brine vapor pressure. The water in the brine is converted to vapor at an evaporation front that recedes into the salt with the. The equation 2.28 that governs the rate of evaporation was proposed by Hohlfelder and Hadley (1979).

$$J_v = \left(\frac{-\theta_c D_k}{KT} \right) \partial P_v / \partial z - \left(\frac{K P_v}{\mu KT} \right) \partial P_v / \partial z \quad \text{Equation 2.28}$$

J_v molecular fluxe of water in vapour phase (molecule/cm² · s)

θ_c Salt porosity connected porosity of the salt

D_k Knudsen's coeficient of difusion (cm² /s) Knudsen's diffusion coefficient

K Boltzmann's constant (erg/molecule K)

T Abosolute temperature (K)

P_v Preasure of water vapour (dina/cm²)

K Permeability

μ Water viscosity (poise)

1 erg = 2,390 · 10⁻⁸ cal

1 poise = 1 g cm⁻¹s⁻¹

The first term refers to the Knudsen fluid diffusion component; the second term is equivalent to the Darcy fluid component. If the sample is subjected to a temperature gradient, the inclusions within the brine will migrate from the grain boundaries and will add to the total water volume.

2.2.2.5 Liquid transport by force gradient applied to salt

The Liquid transport in salts is caused by the brine pressure that is found in the interconnected porosity and is determined by the stresses (the bulk pressure) applied to the salt itself. This fact is specific to the salts, due to the creep behavior. If the brine pressure, which fills the porosity is different from the stress applied in the adjacent salt, then the salt responds by creeping until a pressure in the fluid and the rock are equal.

2.2.3 The permeability of granular Salt

According to Darcy's Law, the movement of the brine in the compacted salt describes the fluid movement through the porous medium. It is considered a representative volume of porosity, to resolve equation 2.29, it is necessary to do a balance of mass in which the change in the volume of brine is equal to the

difference between the brine which has flowed in and out of each side of the volume minus the quantity of brine which has been abstracted. This gives us the relation:

$$\nabla q + \frac{\partial \theta}{\partial t} + Q = 0 \quad \text{Equation 2.29}$$

Where:

θ brine content

t time

Q flux vector

The equation that relates the permeability, in agreement with Darcy's law, is given by modifying the following expression (Eq. 2.30):

$$Q = KA \frac{h_A - h_B}{L} \quad \text{Equation 2.30}$$

where K is the constant of proportionality and is called brine conductivity or permeability. This expression can be expressed in general terms as (Equation 2.31):

$$Q = -KA \frac{dh}{dl} \quad \text{Equation 2.31}$$

Where dh / dl is known as the hydraulic gradient.

A : cross-sectional area of the porous material.

The quantity dh represents the change in piezometric height between two very close points, and dl is a very small distance. The negative sign indicates that the flow is in the direction of the piezometric height decreasing. Equation 28 can be modified to show that coefficient K (Eq. 2.31) has the dimensions of length/time, or speed. This coefficient has been called hydraulic conductivity or the coefficient of permeability:

$$K = -\frac{Q}{A(dh/dl)} \quad \text{Equation 2.31}$$

According to Hubbert (1956), Darcy's constant of proportionality, K , is a function of the properties of the porous medium and the fluid that passes through it. In fact, it is intuitive to think that a very viscous fluid, will move at a lower rate than brine in the same type of soil. The drainage is directly proportional to the specific gravity of the fluid, γ , and inversely proportional to the dynamic viscosity of the fluid, μ . From this information, we can write (Eq. 2.32 and 2.33):

$$K = k \frac{\gamma}{\mu} \quad \text{Equation 2.32}$$

$$K = k \frac{\rho g}{\mu} \quad \text{Equation 2.33}$$

Where k is the permeability of the soil. In the last expression ρ is the density of the fluid and g is gravity.

Two different methods can be used in order to know the quantification of the permeability coefficient or hydraulic conductivity. The two types are the indirect and direct methods. Indirect methods, are determined by an empirical formula and the direct methods, are measured directly in the laboratory. The permeability or hydraulic conductivity can be measured with parameters. The difference between constant load and variable load is that in the first parameter, the fluid needs to reach the equilibrium and in the second case it is not necessary. In this case, there is a decrease in the level of the fluid, which passes through the sample. The following expression (Eq. 2.32), gives the rate at which the fluid flows down:

$$v_{int} = - \frac{dh}{dt} \quad \text{Equation 2.34}$$

If A_t is multiplied by the area of the vertical tube, it is obtained the water flow (Eq. 2.33):

$$q_{int} = v_{int} A_t = -A_t \frac{dh}{dt} \quad \text{Equation 2.35}$$

When A_c is the area of the soil sample, it can be used Darcy's law to calculate the flow draining from the permeameter at any time, where h is the hydraulic load at time t (Equation 2.36):

$$q_{out} = \frac{k A_c h}{L} \quad \text{Equation 2.36}$$

If it is applied the principle of continuity, can be using the expressions given in (Eq. 2.37) and (Eq. 2.38) to write (Eq. 2.39):

$$-A_t \frac{dh}{dt} = \frac{k A_c h}{L} \quad \text{Equation 2.37}$$

If isolating the permeability K (Eq. 2.38):

$$K = - \frac{A_t L}{A_c h} \frac{dh}{dt} \quad \text{Equation 2.38}$$

If the equation is integrated from $t = 0$ to $t = t$ with an initial condition $h = h_0$ at $t = 0$ the following expression (Eq. 2.39) is obtained for the hydraulic conductivity as of a variable load permeameter:

$$K = \frac{A_t L}{A_c t} \ln \frac{h_0}{h} \quad \text{Equation 2.39}$$

If the diameters of the vertical tube and the sample are used, it is obtained the following equation (eq. 2.40):

$$K = \frac{d_t^2 L}{d_c^2 t} \ln \frac{h_0}{h} \quad \text{Equation 2.40}$$

It must be verified that the sample is completely saturated, and it is necessary to be sure that there are no air bubbles within it. When there are air bubbles, the hydraulic conductivity decreases due to the reduction in the available water area.

2.2.4 Associated Microstructures on the strain/ deformation mechanisms

Creep is viewed to occur by the dissolution of material at grain boundary interfaces under high mean normal stress, diffusion through the grain boundary solvent phase, and precipitation at interfaces under low mean normal stress. This pattern of mass transfer is illustrated in Figure 2.17 a. The typical microscopic structure of saline aggregates is an island-channel system, as in Figure 2.17 b, other less known microstructures associated with the dissolution-precipitation of salt are shown in Figure 2.18 (Spiers et al., 1990).

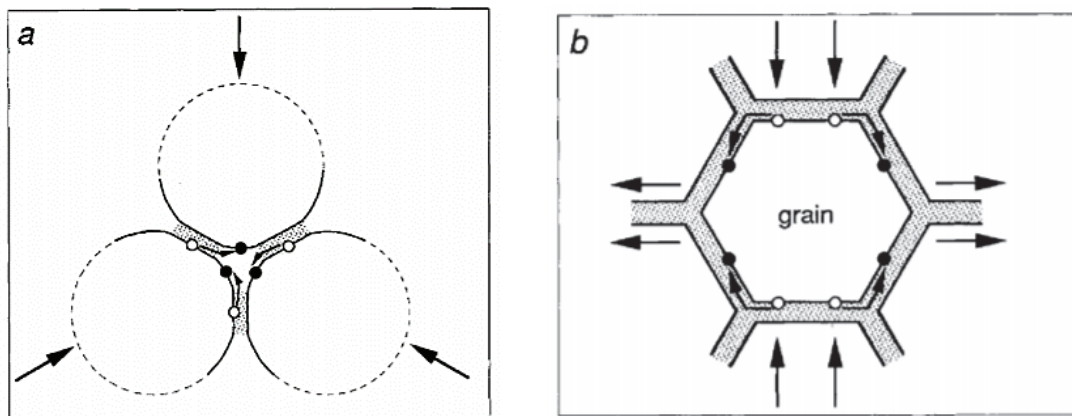


Figure 2.17 Schematic diagrams illustrating the pattern of mass transfer involved in creep by pressure solution. (a) Compaction creep in a porous or granular polycrystalline aggregate saturated with fluid Figure. (b) Conventional creep in a dense polycrystalline material. In both cases, grain boundaries contain fluid in an adsorbed film or island-channel form (Spiers et al., 1990).

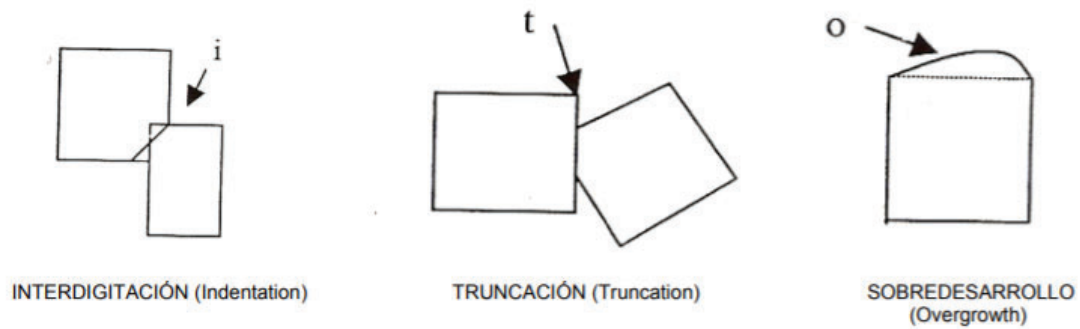


Figure 2.18. Microstructures graphic associated with salt strain/deformation (Spiers et al., 1990).

Figure 2.19 shows the microstructure of the indentation. This structure shows that when the boundaries of two adjacent salt crystals intersect, part of one crystal may become part of the other crystal. These structures are common at the apex of grains of salt. In Figure 2.19.b, the truncation microstructure is common in crystals which have not been able to develop any of their faces or vertex, in many cases the adjacent crystal had a higher development speed. In Figure 37. c, the salt crystals overgrowth, nowadays the mechanism which produces its microstructure is not clear (Spiers et al., 1990).

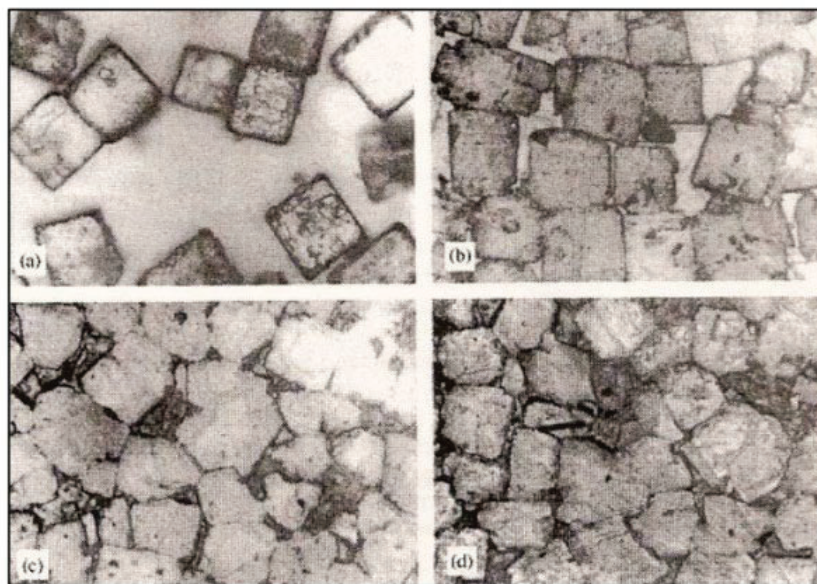


Figure 2.19 Microphotography obtained in the laboratory. (a) Initial granular material ($d_0 = 275 \mu\text{m}$). (b) Compacted salt ($\epsilon_v = 11\%$, $d_0 = 410 \mu\text{m}$), the island-channel microstructure is shown, (c) Compacted salt ($\epsilon_v = 20\%$, $d_0 = 410 \mu\text{m}$), interdigitation, truncation and overdevelopment structures are shown, (d) compacted salt ($\epsilon_v = 24\%$, $d_0 = 175 \mu\text{m}$), interdigitation, truncation and overdevelopment structures are shown (Spiers et al., 1990).

2.3 Geochemistry

As it is stated in Chapter 01, the CPB is a stratified evaporitic deposit. The formation of the several layers that form the deposit is the result of various stages of evaporation of an ancient sea. This section will focus on the material that constitutes the insoluble part of the saline layers. These insoluble geological materials can be found within the salt beds and also between them, thus forming thin layers that separate the different types of salts that compose the deposit. According to (Cendón et al., 2003) insoluble particles are formed by sulphate such as anhydrite and clays. Moreover, Pueyo (1975) define a pelitic fraction made basically by phyllosilicates such as clay minerals, stating that the presence of this clay phase in the evaporitic deposit has an essential role during both the precipitation of salts and the following metamorphic processes, mainly due to its high adsorption capacity. The main minerals that constitute the fraction are chlorites, illites, talc and silica (Pueyo Mur, Juan José, 1975).

2.3.1 Sulphates in evaporitic deposits

It is well known that evaporite deposits are formed by the evaporation of surface water in an arid climate. The presence of sulfates such as gypsum and anhydrite or carbonates is related to the early stages of evaporite mineral precipitation (Hardie & Eugster, 1970, 1970).

The main cations dissolved in surface waters come from chemical weathering of the crust, such as Na^+ , Ca^{2+} , Mg^{2+} and K^+ , the abundance of these cations depends on their relative abundance in the crustal rocks and their solubility (Spencer, 2000). Evaporite minerals are varied, as are their geomechanical behaviors, so it is important to take them into account, especially when they are present in the rock mass of underground infrastructures (Giambastiani, 2020). Specifically, the presence of gypsum or anhydrite has been found to affect the geomechanical properties of infrastructures, in various types of locations and geological environments (Abu Seif, 2014; Alberto et al., 2008; Alonso et al., 2013; Gutiérrez et al., 2008).

2.3.2 Phyllosilicates

Phyllosilicates are a group of silicate minerals whose structure is formed by parallel tetrahedral silicate layers. These sheets have a negative charge, neutralized by exchangeable cations located in the interlayer space and on the surface. They can be classified into two categories: one in which the composition is 1:1, where there is one tetrahedral sheet for every octahedral sheet present, and the second class of minerals has a 2:1 composition with an octahedral sheet

between two tetrahedral sheets. The phyllosilicates group include the following mineral families; micas, chlorite, serpentine, talc, and clays Figure 2.20.

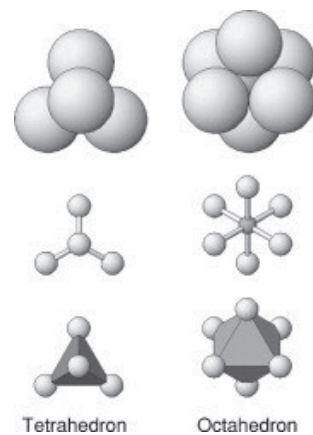


Figure 2.20. Two main types of clay family structures, tetrahedron and octahedron type. The appearance of three different ways of drawing the model: as a sphere-packing model (top row), a ball-and-stick model (middle row), and a polyhedral model (bottom row) (Schulze (2005)).

2.3.2.1 Clays family

Clay minerals represent the main group of the phyllosilicate family. It is a heterogeneous group of hydrous layer aluminosilicates, moreover, the large family of clays can be classified into the groups of kaolinite, smectite, vermiculite, illite and chlorites (Table xxx02). Geologists usually define clays as a group of particles smaller than 2 μm , while engineers and soil scientists define them as any mineral particle with a size below 4 μm . Their small size and large surface area/volume ratio give them unique characteristics, such as their high cation exchange capacity, catalytic properties and plastic behavior when wet (Huggett, 2015). The properties of clay depend on the chemical structure, the type of arrangement of atoms and ions and the type of bands that exist between its layers (C. D. Barton & Karathanasis, 2002), these characteristics depend on its potential applications and geomechanical behaviour (Arabmofrad et al., 2020; Pusch, 2006).

Table 2.1 Phyllosilicates families, reproduced from (Arabmofrad et al., 2020; Bergaya & Lagaly, 2013; Johnston, 2018; Kotal & Bhowmick, 2015).

Layer type	Group	Subgroup	Species
1:1 (T.O)	Kaolin–serpentine	Kaolinites	Kaolinite, dickite, nacrite, halloysite
		Serpentines	Chrysolite, lizardite, amesite
2:1 (T.O.T)	Pyrophyllite–talc Smectite		Pyrophyllite, talc
		Diocahedralsmectites	Montmorillonite, bentonite, laponite, sepiolite, nontronite, beidellite

		Trioctahedralsmectites	Saponite, hectorite, sauconite
	Vermiculite	Dioctahedral vermiculite	Dioct. vermiculite,
		Trioctahedral vermiculite	Trioct. vermiculite
	Mica	Dioctahedral vermiculite	Muscovite, paragonite
		Trioctahedral vermiculite	Phlogopite, biotite
	Brittle mica	Dioctahedral brittle micas	Margarite
		Trioctahedral brittle micas	Seybertite, xanthophyllite, brand site
2:1:1 (T.O.T.O)	Chlorite	Dioctahedral chlorites	
		Trioctahedral chlorites	Pennine, dinochlore, prochlorite

2.3.2.2 Micas family

Micas are 2:1 phyllosilicates with strongly retained, non-hydrated interlayer cations that balance a high layer charge. Micas are commonly found in many rocks, such as shales, phyllites and granites, among others, and in the sediments derived from them. The 2:1 layer of micas is made up of an octahedral sheet between two sheets of tetrahedra. In addition, micas can be classified as dioctahedral or trioctahedral, depending on the types and positions of the cations in the octahedral sheets. In the case of dioctahedral micas, where only two of the three octahedral cations are filled muscovite is the most abundant. Moreover, in the case of trioctahedral micas, all three octahedral positions are filled, and biotite is the most common type. The isomorphic substitution in the mica structure creates a negative charge, which results in a strong coulombic attraction for charge-compensating interlayer cations such as K, which is not exchanged in the standard cation exchange-capacity determination. In addition, micas may be the precursors of expansible 2:1 phyllosilicates, such as vermiculites and smectites, in which micas can be transformed by replacing the interlayer cations (usually K⁺) with hydrated cations (Huang & Wang, 2005).

Finally, in the specific case of sedimentary rocks or soils, mica minerals are usually found in clay fractions and are known as illite or "hydrated mica", "argillaceous mica" and "sericite" (Huang & Wang, 2005).

2.3.2.3 Chlorite family

Similarly, to the mica family, Chlorite has a 2:1 layer structure with an excess of negative charge. However, the excess charge is balanced by a positively charged interlayer hydroxide sheet instead of K⁺. The hydroxide interlayer is an octahedral sheet and can be di- or trioctahedral (Schulze, 2005).

Chlorite is a common phyllosilicate mineral that can be found in all types of sediments and sedimentary rocks. Its presence can be inherited from previous metamorphic or igneous rocks. The name chlorite derives from the green color of

most specimens, which include a group of minerals characterized by a wide range of chemical and structural variations (Bailey, 1988). When found within sediments, they are defined primarily as "clay minerals", in soils that can be an indicator of weathering. The occurrence of chlorite in sediments is usually in small amounts, its origin can be either detrital or diagenetically formed (Schulze, 2005) (Hillier, 2003). The petrology of chlorite in the sedimentary environment is diverse. The presence of chlorite in sediments is commonly described by the associations it forms with other minerals, such as the odinite-berthierine-chamosite shallow-marine association; the Mg-rich chlorite evaporite/dolomite association (Hillier, 2003).

2.4 Subsidence

2.4.1 *The history of the study of subsidence*

According to the information of the subsidence working group in the UNESCO organization (IHD), the oldest known subsidence process happened in the state of Alabama (EUA) approximately in 1900. This work was based on 42 subsidence processes from 15 countries of the world. Around 1965, UNESCO started its first global program for hydrological cycles under the title of World Decade of Hydrology, in the following years the study of subsidence became one of its main topics. In April 1975, a subsidence working group was based in Paris, the basis of which was to investigate the relationship between this phenomenon and underground water. In these surveys, new methods and techniques such as advanced geographic positioning systems (GPS), SAR and InSAR were widely used to locate subsidence in the mid-1990s.

Subsidence processes can be defined as the downward movement of the earth's surface, which can also have a small horizontal displacement vector. They can be produced by natural or anthropic causes. This height change can be a consequence of natural or human activities such as the activity of faults, tunnelling, mining, underground water extraction, and oil and natural gas extraction, among others (USGS). They can let settlement effects on the ground but can also produce collapses in some areas.

According to their origin, they can be classified into two main groups:

1. Subsidence due to natural processes:
 - a. Natural voids near the surface, like karstic features.
 - b. Solubility of some minerals, for example, salt, potash, or gypsum in groundwater.

*Other origins that can conduct subsidence effects are related to alluvial deposits, volcanism, and thermokarst areas, among others.

2. Subsidence due to anthropic works:
 - a. Mining infrastructures
 - i. Fluid extraction (i.e. water or oil).
 - ii. Underground Mining methods
 - iii. Piping methods.

It is of particular interest to focus on the second group, since the case study is an underground ore deposit. Since the nineteenth century, it has been detected subsidence processes produced by underground mining (Halbaum, 1905; Modeste et al., 2021; Sanmiquel et al., 2018; Van Sambeek, 1997). Nowadays, it is known that surface subsidence can be prevented by applying less aggressive extractive methods with the environment and, especially, by applying an appropriate support mechanism, such as rib and sill pillars, cable and rock bolting, plugging of cracks, and backfilling by sand, cement mixed tailing, and waste rock (Waltham, 1989; Zhang et al., 2019). However, underground mining is still leading to the subsidence process (Rošer et al., 2018; Sanmiquel et al., 2018). The subsidence process may be coincident with mining activities or delayed in response to time-dependent deformation of the rock mass. Various mining and geological factors, such as the quality of the underground and rock components, the quality of these geologic materials and surface conditions can influence the magnitude, shape, mode and extent of it (Hunt, 1980).

2.4.2 Subsidence due to underground mining

According to Brady and Brown (1992), subsidence is produced, with greater or lesser impact, by almost all types of underground mining. The downward displacement of the surface may be classified into two different types, discontinuous or continuous (Brady & Brown, 2006). Discontinuous subsidence involves a characteristic profile with step-formation or discontinuities and large surface displacement movements in a delimited area. This type can entail a range of mechanisms caused by different mining methods. Moreover, can be developed progressively or suddenly in a vast range of scales (Figure 2.20). Continuous subsidence has a characteristic smooth profile, with no discontinuities or steps. The resulting surface displacements are usually of an elastic order of magnitude compared to the dimensions of the subsidence zone or depth of drawdown. This type of subsidence is usually associated with the extraction of thin, horizontal, or flat-dipping reservoirs overlain by weak, non-brittle sedimentary strata. Examples of this type may include subsidence processes due to longwall mining of coal or other minerals such as evaporites deposited in sedimentary environments (Figure 2.21). In the following sections, there is a summary of each different type of discontinuous and continuous subsidence mechanism.

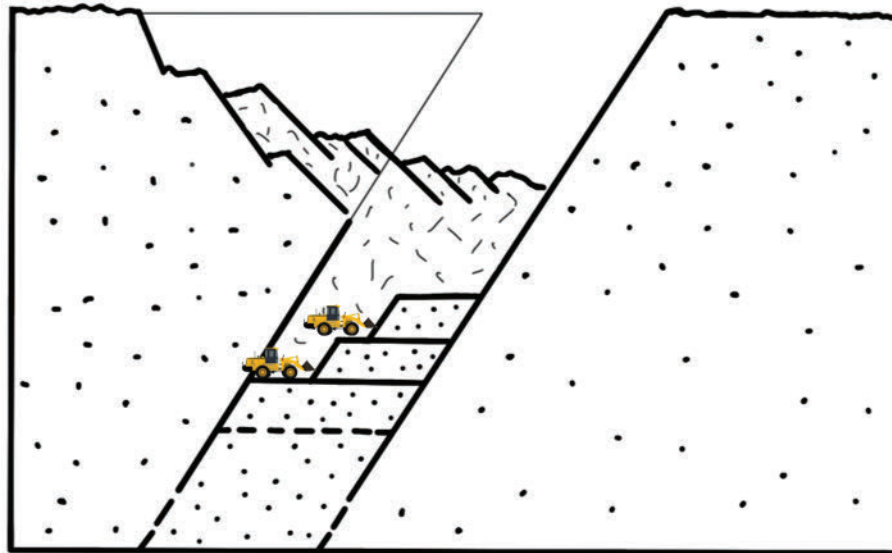


Figure 2.21 Discontinuous subsidence scheme (after Whittaker and Reddish, 1989).

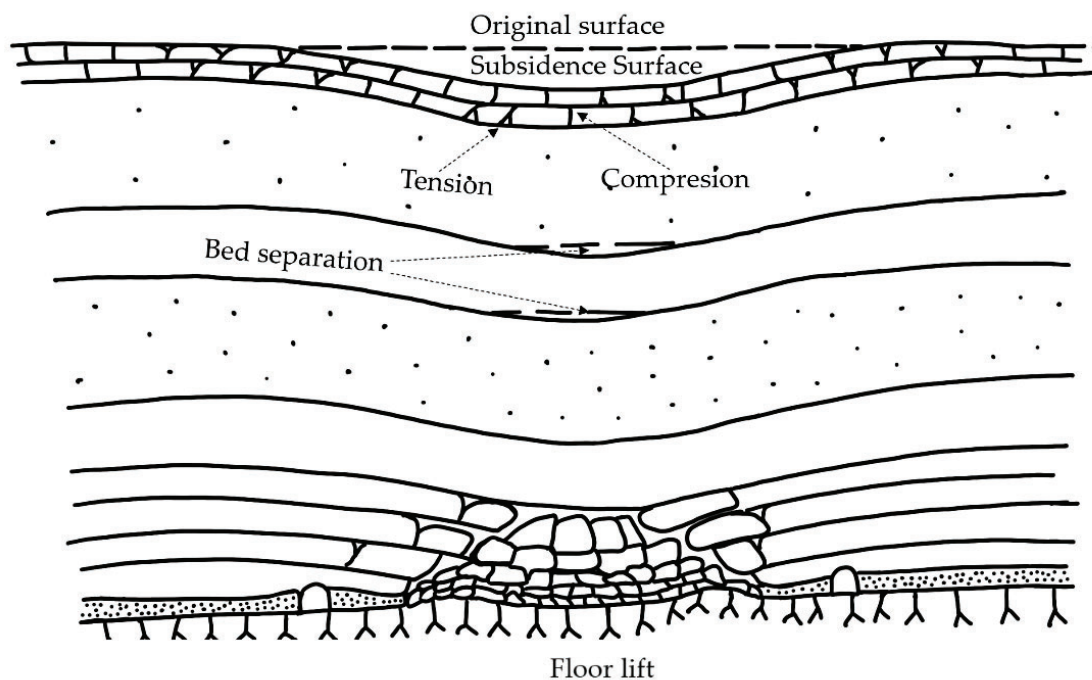


Figure 2.22 Continuous subsidence diagram of the land that sinks due to the subsidence produced by mining in the specific case of a stratified sedimentary deposit (modified by Lee and Abel, Jr, 1983)

2.4.2.1 Discontinuous subsidence mechanisms

Discontinuous subsidence mechanisms are basically included in caving mining methods. Caving mining methods are a type of underground mining method that allows a progressive collapse under the gravity effect. There are three main types of caving methods; block caving, sublevel caving and longwall, which are

described below. These mining methods produce large subsidence areas. According to Brown (2003), several geological and topographical parameters can influence the extent of the surface subsidence, including the dip and strength of the deposit, as well as its plan shape, the strength of the overburden and surrounding rocks, the presence of major structural features, such as faults or dykes crossing the deposit, and the overburden portion. The depth of mining is defined by the undercut level and associated in-situ stress field, surface inclination, any previous mining surfaces, and the placement of backfill in a pre-existing or newly produced collapse or near underground excavations.

Some parameters influence the surface subsidence in caving methods, such as the angle of subsidence or break (its complement angle is called the angle of draw), which is the angle that controls the extent of the surface subsidence, this angle is defined by the horizontal section and the straight line drawn from the level of the undercut to the end of the surface disturbance. The area defined by the angle of break is where large-scale deformations happen, and its adjacent zone is where small-scale deformations occur. Figure 2.22 shows a section of the resulting surface subsidence due to the caving method, with the main geometric parameters highlighted.

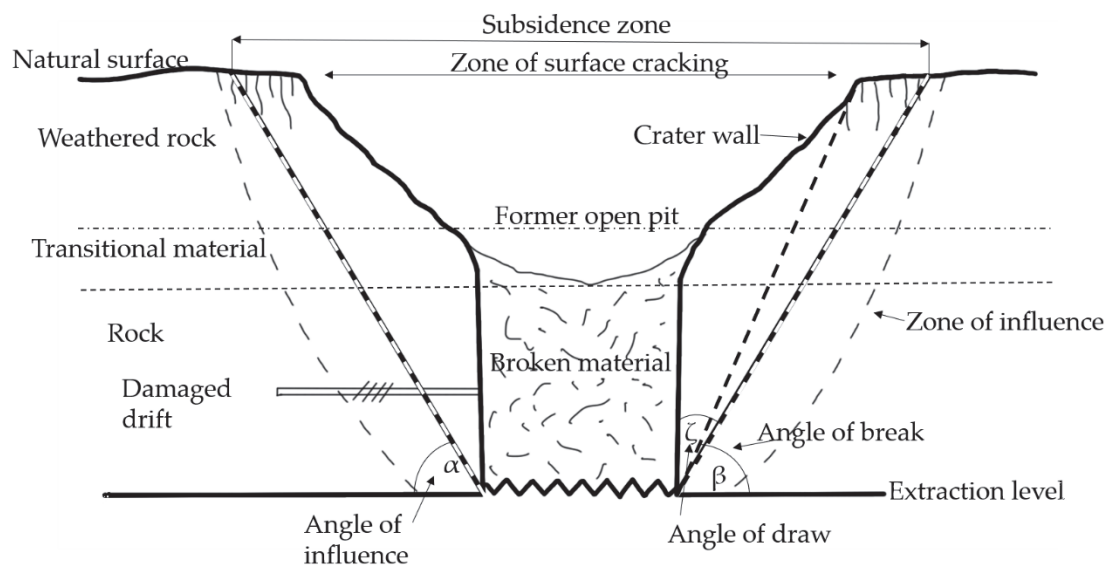


Figure 2.23 Subsidence produced due to block and caving mining method (modified of Brady-Brown, 2006).

As the surface subsidence caused by caving can have different origins, the main ones are described following. Firstly, subsidence can be started by the failure of the stope roof or wall on inclined surfaces. If it cannot be formed a stable arch and self-supporting, the failure may progressively propagate toward the surface, as material falls from the roof or the propagating cave, it will bulk and will tend to fill the void. When the void is filled with caved material it will provide support for the upper surface and so stop the development of the cave, therefore, in this case, subsidence is very important to control the extraction ratio. It is most likely

to occur if the mechanical properties of the hanging wall material are similar to those of soil. Once initiated, propagation of the failure to surface can be very rapid. This mechanism was first proposed by Crane (1931), who studied its development in an iron mining district located in northern Michigan (EUA). It was also studied by Atkinson et al. (1975) in shallow tunnels excavated in sand and clay. Secondly, it can also occur due to the unravelling of a discontinuous rock mass and it is controlled by the regular discontinuities in the rock mass. To continue to propagate this mechanism, a sufficient void must be maintained beneath the cave, therefore, also in this case is very important to control the extraction ratio. This type of chimney caving can be also considered progressive. In 1934 Rice (Rice, 1934) described a graphitic ore deposit. The third mechanism is termed plug subsidence. It is governed by structural features that provide low-shear strength surfaces over which the undercut rock plug can slip under the influence of gravity. In this case, the rock mass will suffer an essentially rigid-body displacement. Therefore, a vertical displacement at the sloped boundary will result in a vertical displacement of similar magnitude at the surface. In this case, the development of this type of chimney cave is not as strongly linked to the control of extraction as the other two types, however, it requires an initial void to occur. In the Athens mine, located in northern Michigan (EUA) a plug subsidence mechanism was controlled by dykes (Boyum, 1961). In addition, sinkholes or dolines can be described as cylindrical or conical holes, and sometimes included as a chimney caving subsidence mechanism. Mostly they are caused by natural processes like ones formed in karstic environments. However, it can be produced due to the anthropic lowering of the water table (De Bruyn et al., 2000). In addition, this type of formation can also happen by the sudden or progressive collapse of the overlying material into an underground cave or infrastructure. Chimney caves are also known as sinkholes (Szwedzicki, 1999). Finally, another type of mining method that can cause discontinuous subsidence mechanisms, is the mining infrastructures of chambers and pillars, in this case, the mining infrastructure has to be located in a shallow underground area and does not have a good closure process, so it can collapse due to its deterioration. According to Brady and Brown (2006) one of the major examples of this type of collapse happened in 1960 at the Coalbrook North Colliery, (South Africa), when a room-and-pillar mining area of approximately 3 km² collapsed (Bryan et al., 1964).

2.4.2.2 Continuous subsidence mechanisms

Continuous subsidence processes are basically produced when a tabular horizontal orebody is mined by methods that give a very high extraction ratio in large panels. For the subsidence mechanism to be continuous, the subsidence stress (induced by caving), the depth of the mining infrastructure and the strength properties of the overlying material has to be such that fracturing and discontinuous rock movement are restricted to the immediate surroundings of

the deposit (Brady & Brown, 2006). This mechanism can occur in evaporites overlain by sedimentary rocks and in the case of longwall coal mining operations, among others.

A continuous subsidence basin can be active for some time after the mining infrastructure has stopped. This time dependent characteristic in subsidence can be measured through what is called subsidence velocity, it is well-known that it will gradually decrease until it stabilizes. Subsequently, it will be formed the static or final surface subsidence basin. In Figure 2.24, it can be seen the process of development of the surface subsidence basin, these different basins will occur as mining infrastructure is excavated. (Peng, 2020).

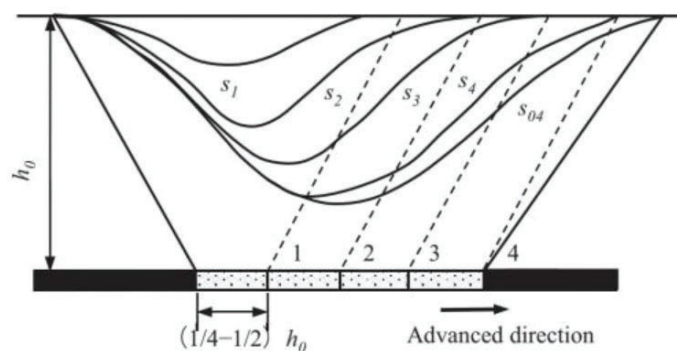


Figure 2.24 Process of forming surface movement basin. 1, 2, 3, 4 equal different positions of face advance; s_1 , s_2 , s_3 , and s_4 are surface movement basins formed when the face is at the corresponding positions of 1, 2, 3, 4, respectively; s_{04} is the final surface static movement basin. h_0 is mining depth. (Peng, 2020)

Furthermore, in Figure 2.25, we can see a typical vertical section through workings (National Coal Board, 1975). Where three different subsidence and surface slope profiles can be observed for three different panel widths. The vertical displacement, s , is called the subsidence, therefore the maximum subsidence is shown with an S in capital letter. At the point of maximum subsidence, the corresponding area and width are referred to as critical. Areas of widths for which $S < S_{max}$ are described as subcritical. In the case of supercritical areas or widths, S_{max} subsidence is reached over a finite width and not only in a single point as in the critical case (Figures 2.25 a, b and c).

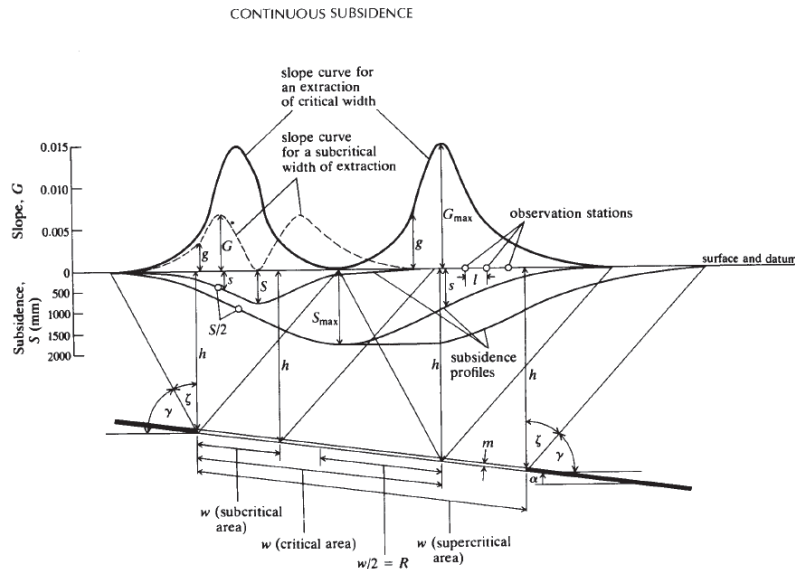
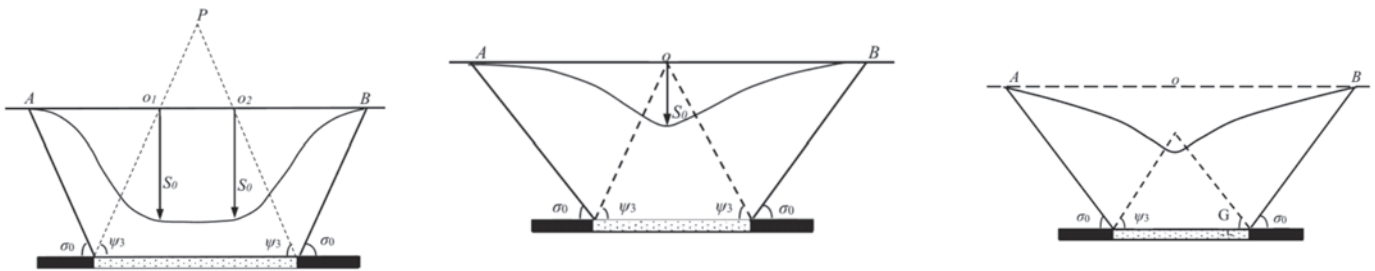


Figure 2.25 Subsidence profile and main parameters (National Coal Board, 1975).



Figures 2.26 a Supercritical subsidence basin, b Critical subsidence basin and c Subcritical subsidence basin (Peng, 2020).

As we can see in Figure 2.25 (typical section), there is highlighted the angle of draw (ζ), which can be described as the angle made with the vertical by an imaginary line drawn that goes from the base of the mined seam to the point of zero subsidence in the surface. Therefore, this angle depends directly on the depth of the mining infrastructure and the width of the subsidence basin.

Apart from the vertical displacement, all points in the subsidence basin will develop also the horizontal displacement. The slope of the surface subsidence and the developed strains in the surface subsidence vary at all points of the subsidence surface. Consequently, for a horizontal seam with a depth (h), complete subsidence will occur directly at a point vertically above the centre of the zone, if the exploitation of a critical zone reaches what is called critical diameter (D_c) and critical width (W_c) (Equation 2.41).

$$W_c = 2h \tan \zeta \quad \text{Equation 2.41}$$

2.4.3 Surface subsidence areas

According to the in-situ measurements in several worldwide examples, it is known that the surface movement basin is larger than the mining gob. The shape of the surface subsidence basin depends directly on the shape of the mining gob. In addition, if the gob follows an inclined seam, this inclination will affect the surface subsidence basin. If the subsidence process is active, the surface of the basin will have a heterogeneous shape, in different parts there will not be the same amount of deformation. However, when this surface is completely flat, it indicates that the zone has reached the final or static subsidence movement basin, which according to Peng, 2020 can be divided into 3 zones. Figure 44 shows them.

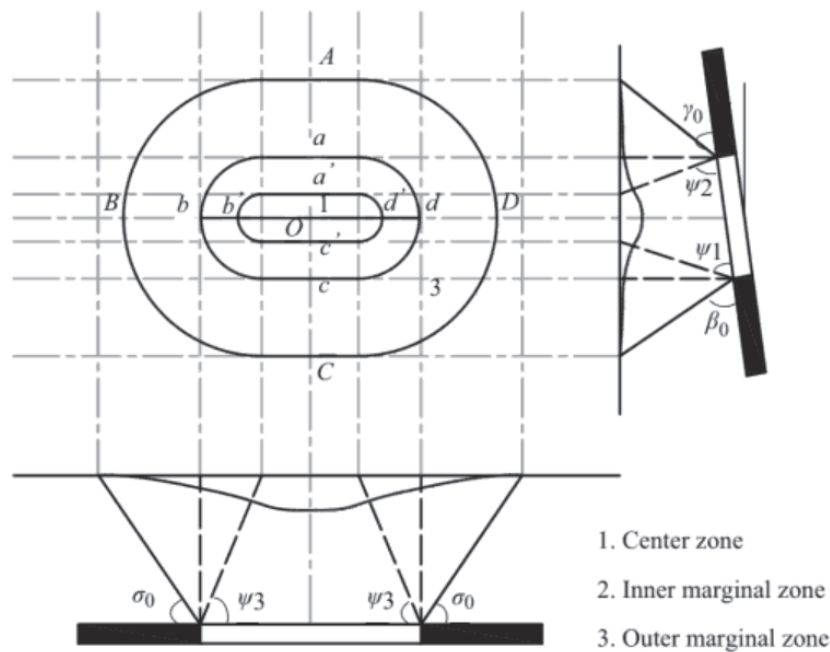


Figure 2.27 The three zones of a surface subsidence basin (Peng, 2020)

First, it can be defined as the central surficial subsidence zone or neutral area, where deformation and displacement values are close to zero, and usually, it is a zone without cracks. In this zone the surface subsidence is uniform and its values are maximal. The inner marginal zone or compression zone is located between the central zone and the collapsed area. Usually, there is also no presence of cracks in this zone. In this case, the subsidence surface forms a concave profile producing a compressive deformation, subsidence values may vary and move towards the centre of the basin. Finally, there is the external marginal zone, also named the tensile zone. This zone is located in the outer part, forming a convex profile and producing a tensile deformation. According to Peng (2020), among many other authors in the field (Booker & Carter, 1986; Ege, 1984; Galloway et

al., 1999; Walker, 1988), the superficial subsidence is not uniform and the movement of the ground goes towards the inner central zone.

Three boundaries can be distinguished in the surface movement basin depending on the influence of surface movement, as well as deformation in structures and on the surface. The most external boundary is known as the outermost boundary and the theory states that is determined by the basin boundary at which surface movement and deformation are zero. In field measurements, the boundary value is defined by the value of 10 mm of subsidence due to measurement errors. Therefore, the outermost boundary contour is determined by the 10 mm value points (Peng, 1992). The dangerous limit is defined as the limit of the critical value, which means that the infrastructure located within the limit will be damaged. The critical values of deformation are tilt (t), strain (e), and curvature (k) and their values depend on the country (Peng, 1992). The cracks boundary is defined by the line where the cracks in the surface subsidence basin will occur (Peng, 1992).

There can be distinguished three main angles: The angle of draw (δ_o), the angle of critical deformation (δ), and the angle of the outmost crack (δ''). The angle of the draw is the acute angle between the line connecting the edge of the movement basin with the 10 mm subsidence and the gob edge and the horizontal line at the gob edge. The angle of critical deformation is the acute angle between the line connecting the point of critical deformation on the major cross-section of the basin and the gob edge, and the horizontal line at the gob edge. The angle of the outmost crack is the acute angle between the line connecting the outmost surface crack and the gob edge, and the horizontal line at the gob edge. The three angles can be shown in Figure 2.28 (Peng, 1992).

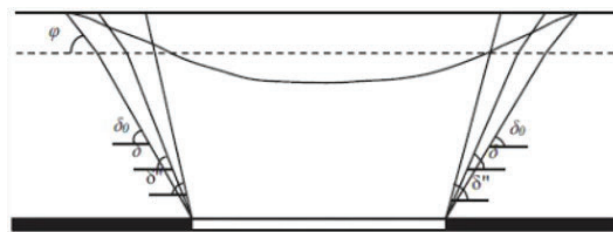


Figure 2.28. characteristic angles in a subsidence profile along the directions of a horizontal mining drift.

2.4.4 Introduction to subsidence of evaporite reservoirs

Right after the exploitation of potash minerals, it starts convergence movements, when stress increases and exceeds the strength of the rock layer, this can break and, therefore, fall. This process can produce a collapse due to the formation of a block, beam or plate. With the expansion of the mining infrastructure, the area of

affection can reach the surface, producing what is known as surface subsidence (Figure 2.21). (Peng, 1992). Surface subsidence caused by underground mining is a process that depends on time and space. Surface subsidence caused by underground mining is a process that depends on time and space. Usually, the subsidence process begins with the opening of a mining drift, after reaching a maximum speed it slows down and generally with the closure or non-exploitation of the area a stabilization stage begins. It is noticed that the properties of surface subsidence once mining stops are different from what occurs when mining is active and, therefore, both scenarios need to be properly investigated (Guo et al., 2021; Peng, 1992, 2020). Nowadays, it is well-known that subsidence processes depend on geological and mining factors (Hunt, 1980), such as the type of deposit where the effect is produced or the mining method used to extract the mineral of interest. In the case of evaporitic minerals overlaid by weak sedimentary rocks, such as the case study, the subsidence process can be classified as continuous, rather than discontinuous (caving mining methods).

2.4.4.1 Subsidence in C.P.B

Subsidence processes can cause fissures in the ground that may expand slowly and gradually and can lead to catastrophic processes such as collapses. Damages caused by subsidence and cracks in the ground are irreparable, costly and destructive. As an example, the subsidence phenomenon, by creating a change in the topography of the region, can cause significant changes in the hydrology of the region, which is one of the basic natural resources (SDGS). For example, huge and destructive floods can occur in these areas, unprecedented before subsidence. On the other hand, this phenomenon can cause more abnormal results by causing changes in the geohydrological situation of the region, such as the direction and velocity of groundwater flow or the groundwater balance.

In addition, subsidence can lead to the destruction of irrigation systems and fertile agricultural soils (by lowering their porosity). Furthermore, urban areas are particularly vulnerable due to the density of population, buildings and vital infrastructures. This phenomenon can damage streets, bridges and highways, disrupt water, and gas lines, damage the foundations of buildings, and cause cracks in them. Therefore, prediction techniques are needed to evaluate the potential effects of subsidence in order to prevent potential issues. In the case of the Catalan Potash Basin (C.P.B), subsidence has played a very significant role since, at the beginning of the 2000s, an entire neighbourhood located in Sallent (BCN) has to be evicted. This municipality is found right above a former mining area (Pipia et al., 2007). Since then, the subsidence produced in CPB is measured annually, and thus, nowadays we have a large database of subsidence values for more than a decade.

2.4.5 Subsidence prediction methods

When in the ground of the surface subsidence there are infrastructures, it is essential to define a predicting model to assess the scenarios that can be developed, as well as their possible consequences. Therefore, according to the National Coal Board (1975), the main parameters to assess are:

- The maximum subsidence, S_{max}
- The maximum ground tilt, G_{max}
- The maximum tensile and compressive ground strains, $+E_{max}$ and $-E_{max}$
- The minimum radius of ground curvature, R_{min}

According to Figure 2.24, it can be found that the tilt and strain are proportional to the maximum subsidence and inversely proportional to the cover depth (Equations 2.42, 2.43, 2.44). Therefore:

$$+E_{max} = 1000 \cdot K_1 \cdot S_{max}/h \quad \text{Equation 2.42}$$

$$-E_{max} = 1000 \cdot K_2 \cdot S_{max}/h \quad \text{Equation 2.43}$$

$$+G_{max} = 1000 \cdot K_3 \cdot S_{max}/h \quad \text{Equation 2.44}$$

Where K_1 , K_2 , K_3 are constants of proportionality.

The curvature $1/R$ is directly proportional to the strain and indirectly proportional to the depth of mining (Equation 2.45), therefore:

$$1/R_{min} = K_4 \cdot E_{max}/h \quad \text{Equation 2.45}$$

Where K_4 is a constant of proportionality.

One of the most widely used methods for predicting maximum subsidence in continuous subsidence processes was developed by the National Coal Board (1975). This developed methodology has been very successful in predicting, with a 90% confidence level, several subsidence processes in coal basins in the UK, not considering the influence of geological features such as faults or the deformation of layers (Brady and Brown, 2005).

According to Figure 2.24, the mathematical way to describe the shape of the subsidence basin profile can be as follows (Equation 2.46, 2.47):

$$s = S_{max}f(B, x, c) \quad \text{Equation 2.46}$$

$$B = h \tan \zeta \quad \text{Equation 2.47}$$

Where B is called the critical radius of extraction

x is the horizontal distance of the point from the origin of the coordinates

c is a constant

There are six categories of subsidence prediction methods: theoretical, profile function, influence function, empirical, physical and numerical modeling (Peng, 1992).

- Theoretical methods aim to explain a mechanism that may predict the vastness of subsidence.
- Profile function methods determine a number of standard functions.
- Influence function methods are based on the effect of the extraction of infinitesimal elements of an area.
- Empirical methods use graphs and tables.
- Physical methods built a real model at a smaller scale than the extracted area.
- Numerical models use finite elements, boundary elements, distinct elements and finite difference methods to calculate the displacements and subsidence of the ground surface

Figure 2.29 shows the main subsidence prediction methods currently in use. These are the traditional curve method, the profile function method, the influence function method and numerical modeling using finite element, discrete element and finite difference methodologies. (Peng, 1992).

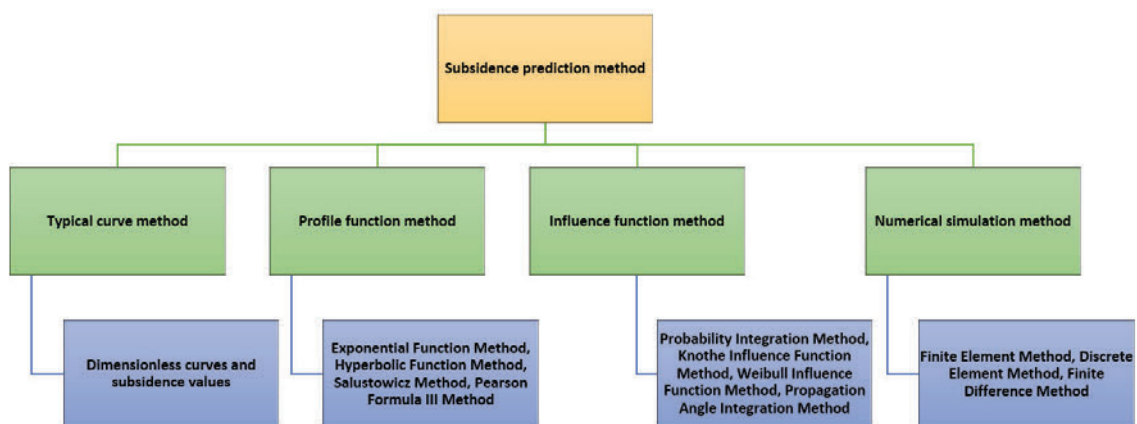


Figure 2.29 Subsidence prediction methodologies are based on four steps; the model, the parameters the algorithm and the software. The average prediction precision of subsidence is 10% (Adapted from Peng, 1992).

The model is a formula used to represent the distribution and propagation of surface and subsurface subsidence due to underground mining.

- Parameters are constants and are used to show the difference in geological conditions.
- There are several subsidence integration algorithms, including Gauss, Newton-cotes and Romberg integration.

2.4.5.1 Surface subsidence variables and their general relationship

The three main components that influence the mining subsidence are the overlying and underlying rock strata, surface and loose layers. According to Dai (2018) and based on the type of movement, directions and properties, nine variables of displacement and strain can be defined. Five vertical movements and strains, subsidence (S), tilt (i), vertical strain (ε_z), curvature (K) and twist (τ) and four horizontal movements and strains, horizontal displacement (u), horizontal strain (ε), shear strain (γ), and deflection (i_z) (Peng, 1992).

2.4.5.2 Typical curve method

The method of the typical curve (TCM) is based on measured data and it is classified as an empirical method. It is a non-dimensional curve in the principal cross-section of the surface movement basin. Because its distribution and properties are calculated directly from a vast amount of measured data, it is very reliable and straightforward to use. However, the MTC is only suitable for rectangular or rectangular-shaped mining zones (Peng, 1992).

2.4.5.3 Profile function method

A profile function method (PFM) describes the distribution of surface subsidence values throughout a profile or cross-section, as well as the deformation displacement or curvature (Diez & Alvarez, 2000). The profile is usually orthogonal to the boundary of an underground excavation of a geometrically simple shape (e.g. square or a rectangle). Profile functions allow a one-dimensional display of subsidence as a function of distance from the centre of the excavation. The profile function for predicting mining subsidence is probably the most widely applied method, suitably represented by mathematical equations or tables (Peng, 1992). However, the main disadvantage of this methodology is that it may not apply to mining infrastructures with an irregular shape with significant variances in mining properties (mining height, percentage of extraction, depth of excavation) (Bräuner, 1973; Karmis et al., 1987; Peng, 1992).

2.4.5.4 Probability integration method

The probabilistic integration method (PIM) is a theoretical method developed by Liu and Liao in 1965, which states that the variability and randomness of rock movement must be considered. The method is based on the idea that ground movement caused by underground mining is a random event, and the mining area can be subdivided into micro-units, each unit producing a corresponding unit subsidence basin with a normal distribution (Peng, 1992). Some examples are given below (Diao et al., 2016; Li et al., 2018).

2.4.5.5 Surface subsidence prediction for mountain area

According to (Peng, 1992). This method is intended for horizontal, slightly inclined coal seams with an average dip angle below 30 degrees (Zhou et al., 2022). The Subsidence expression is shown in equation 2.48:

$$S_{mou}(x, y) = S(x, y) + D_{x,y}\{P[x]\cos^2\phi + P[x]\cos^2\phi + P[y]\sin^2\phi + P[y]\sin^2\phi\cos^2\phi tg^2\alpha'_{x,y}\} \quad \text{Equation 2.48}$$

$S_{mou}(x, y)$ is the subsidence at any point (x, y) in mountain terrain (mm);

$S(x, y)$ is subsidence at any point (x, y) in the flat surface under the same conditions (mm);

$u(x, y)$ is the horizontal movement at any point (x, y) in a flat surface in the direction of ϕ under the same conditions (mm).

The major influence radius r is calculated by the following equation 2.49:

$$r(x, y) = \frac{H(x, y) - H_0}{\tan\beta} \quad \text{Equation 2.49}$$

Where $H(x, y)$ is the elevation of ground prediction point (x, y) in mountain area (m).

H_0 is the average elevation of the panel floor (m)

$D(x, y)$ is the ground characteristic coefficient for the point (x, y)

$\alpha'_{x,y}$ is the inclined angle of the ground surface at any point (x, y)

ψ is the calculation direction angle, from the positive x-axis to the reverse clockwise direction.

In Equation 2.50 $P(x)$ and $P(y)$ are described, they are slip effect functions for the main cross section across strike and dip directions.

$$P(x) = 1 + A_e - \frac{1}{2}\left(\frac{x}{r} + P\right)^2 + S_0 e^{-t\left(\frac{x}{r} + P\right)^2} \quad \text{Equation 2.50}$$

$A, P, \text{ and } t$ are slip influence parameters. Their reference values are $A=2\pi, P=2$ and $t=\pi$

2.5 Numerical modeling

Nowadays, numerical modeling is widely used to simulate rock mass behavior in various geotechnical contexts. Numerical methods used in geomaterial modeling involve the finite element method (FEM), boundary element method (BEM), finite difference method (FDM), and discrete element method (DEM) (C. C. Li, 2017).

In the early 1960s, Clough in the book "The finite element method in plane stress analysis" introduced the expression "finite element" (Clough, 1980, 1990, 1960). One of the essential contributions to the FEM development was done (Turner et al., 1956), who presented the application of finite elements for the analysis of aircraft structures. In addition, stated that FEM is a computing tool used to obtain approximate solutions to boundary value problems in engineering (C. C. Li, 2017).

The FEM methodology allows the continuous to be discretized into a finite number of elements. Moreover, the characteristics of the continuous domain can be approximated by ensemble similar properties of the discretized elements per node. The FEM method has been used for a large range of problems in applied science and engineering and has developed very quickly over the years (Rao & Morris, 2006).

The FEM can be adapted to meet certain accuracy specifications without the need for physical prototypes in the design process. Thus, with the help of the software, different designs and materials can be modeled in a matter of hours. In addition, the FEM method allows for easy modeling of irregular geometric shapes, as is the case with some geological bodies or terrain. Another advantage of the FEM method is that it can solve the problem with a high degree of accuracy. In addition, the designs use boundary conditions to define how the model should respond. The boundary conditions can include point forces, distributed forces, among others. Another advantage of this system is that it is very visual, so any vulnerability in the design can be easily detected thanks to the detailed visualizations, and It allows a detailed and very accurate structural analysis (Adams & Askenazi, 1999), (Zienkiewicz et al., 2005) (Chakraverty & Pradhan, 2018).

2.5.1 Subsidence Prediction in Ebro Basin and Catalan Potash Basin (C.P.B)

Subsidence in the Ebro basin is basically related, on the one hand, to processes associated with water systems (Concha et al., 2010). On the other hand, it is linked to processes related to evaporite formations. These, in turn, can be divided into processes associated with karstic formations (Galve et al., 2008; Gutiérrez et al., 2008, 2008; Torrijo et al., 2020; Universidad de Zaragoza et al., 2017) or underground mining (Campos de Orellana, 1996; Sanmiquel et al., 2018).

2.5.2 Finite Element Method (F.E.M.)

The finite element method originated between 1940 and 1960 to develop an analysis of structures. The concept of "element" is derived from the techniques used in stress calculus, where a structure is divided into several substructures

or elements to analyze them more easily. Since then, the finite element method has evolved. Nowadays, the most widely used finite element method is the one based on the study developed by (Turner et al., 1956). This study focused on the properties of triangular elements in plane deformation problems. In recent years, finite elements have been applied with great success to a variety of problems.

The finite element method is a common technique to solve differential equations. As mentioned earlier, the finite element method is based on dividing into smaller regions the domain in which the differential equation is defined. By using a low-order polynomial function, the solution of the differential equation can be approximated on each element.

According to Whiteley (2014), if thinking about a differential equation, defined on the interior of the ellipse $\frac{x^2}{4} + y^2 = 1$ by Eq. 2.51:

$$-\left(\frac{\partial^2 u}{\partial x^2} + \frac{\partial^2 u}{\partial y^2}\right) = 1 \quad \text{Equation 2.51}$$

It is applied Dirichlet boundary conditions on the boundary of the ellipse where $y \leq 0$, given by Equation 2.52:

$$u(x, y) = x \quad \text{Equation 2.52}$$

And Neuman boundary conditions on the boundary of the ellipse where $y \geq 0$, given by Equation 2.53:

$$(\nabla u) \cdot n = \sin(2(x + y)) \quad \text{Equation 2.53}$$

The vector n that appears in Neumann (Cheng & Cheng, 2005) boundary conditions is a normal vector, it has a unit length and is perpendicular to the plane of the ellipse.

Firstly, to calculate the finite element solution of the differential equation, the domain of the differential equation defined should be divided. Therefore, this means to divide into elements the interior of the ellipse $\left(\frac{x^2}{4} + y^2 = 1\right)$ into elements. Figure 38 shows the domain divided into triangular elements.

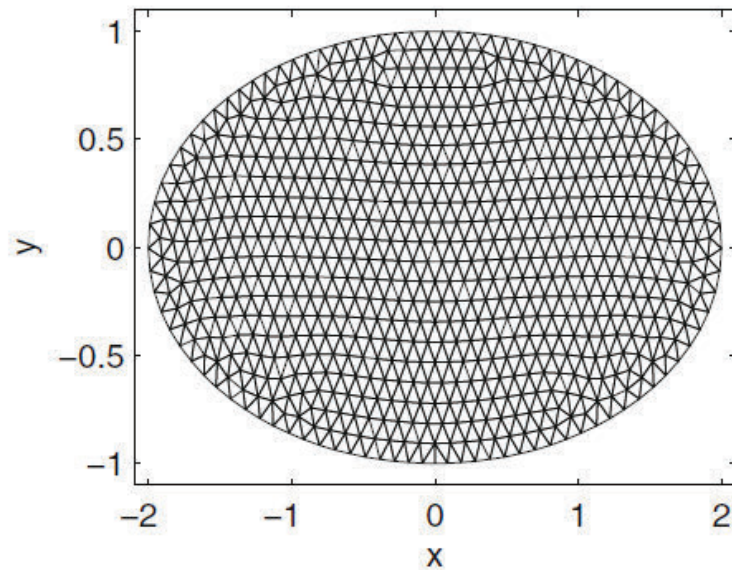


Figure 2.30 Portioning of the domain into triangular elements (Whiteley, 2014).

Secondly, once the ellipse is divided, it can be calculated the finite element solution of the differential equation, which is a linear approximation to the solution of each element. Figure 39 shows it.

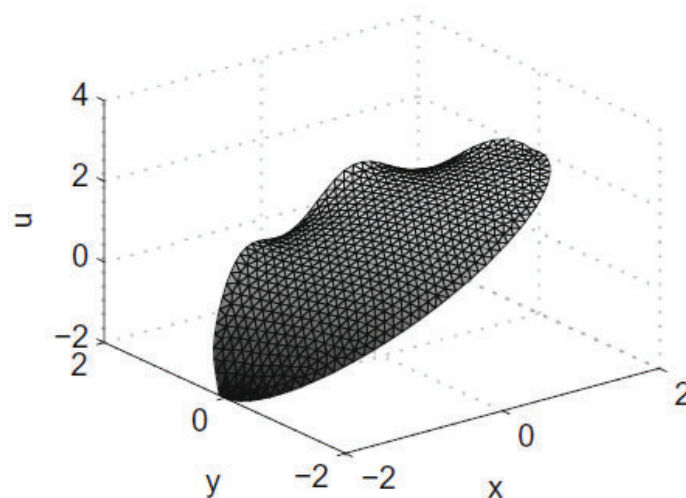


Figure 2.31 The finite element approximation to the solution of the differential equation (Whiteley, 2014).

There are three key features that make the finite element method very useful. Firstly, the finite element method can deal with domains that are of arbitrary shape. Secondly, boundary conditions with derivatives are easy to handle (i.e. Neumann boundary conditions). Finally, if it is required to reach a more accurate finite element solution, two options can be used. On the one hand, the domain can be divided into smaller triangular elements. On the other, it can be increased the degree of the polynomial approximation in each element (Whiteley, 2014).

2.5.2.1 Finite element method from a practical point of view

The FEM is a numerical method of solving differential equations. The solution obtained by FEM is only approximated. Only coinciding with the exact solution, is a finite number of points called nodes. The set of nodes is obtained by dividing or discretizing the structure into elements. The FEM method finds the solution in the rest of the domain by interpolating node values (Logan, 2011, 2022).

The first step in any FEM simulation is to discretize the initial geometry of the structure, or part, using a collection of finite elements. Each finite element represents a discretized portion of the physical structure. The finite elements are linked by shared nodes. The set of nodes and finite elements is called a mesh. The number of elements per unit length, area or volume of a mesh is the mesh density. Once the nodal displacements are known, the stresses and strains of each finite element can be calculated.

A complete analysis with FEM software usually consists of three distinct phases: pre-processing, simulation and post-processing. In the preprocessing stage, the physical model of the problem must be defined and, moreover, an input file must be created. The model can be settled up graphically using FEM software or also it can be imported from another type of software such as 2D or 3D CAD. Once the model is defined, it should be discretized and meshed. Then, the boundary conditions are applied and the materials are defined.

Once the simulation has been completed and the displacements, stresses and other key variables have been calculated, the results can be evaluated. The evaluation is generally performed interactively using the FEM software visualization module. This module has a variety of options for displaying the results, including graphical representation with colored contours, animations, graphical representation of deformed models and others. deformed models, etc.

2.5.3 Finite element method (F.E.M.) applied to underground infrastructures

The finite element method is a good tool to analyze the ground movements due to the excavation of underground infrastructures. Nowadays, numerical modelling is highly used in the engineering field, as well as the implementation of the FEM methodology in the analysis of the ground movements and deformations due to excavations. However, it has to be carefully assessed when to use them (Augarde et al., 2021; Potts et al., 2001; Singh et al., 2010). Several factors can influence the accuracy of the finite element method solution, including the degree of simplification and the assumptions made on the problem, the approximation of geological and hydraulic boundaries, initial stresses, the constitutive model used, the construction process and the geometry of adjacent

structures. Therefore, they have to be reviewed and carefully applied (Wongsaroj et al., 2005).

To use the finite element method to model a deposit, is necessary to set a geomechanical design for it. For example, from the mining area to the surface if the surface subsidence is to be modeled (Fredrich et al., 2000; Kolivand & Rahmannedjad, 2018; Paraskevopoulou et al., 2012). The design has to include the geometry of the ore deposit, the different geological layers that form it and their properties.

One of the main advantages of the method is that it is very versatile and a wide range of geological geometries that can be defined, as well as the different geological materials and their geological properties, also the overburden, can be modeled very accurately (Geertsma & Opstal, 1973; Parmar et al., 2019). Another advantage of the finite element method is the ability to model structures with challenging geomechanical behaviors as in the case of the Ameland salt deposit (Ketelaar, 2009; Marketos et al., 2015).

Although FEM methodology makes it possible to reach a very accurate prediction of vertical displacements, as well as horizontal gradients, it also has some associated limitations, such as computational time. One of the possible solutions is not to simplify the geological setting to make easier the calculation process (Geertsma, 1973; Ketelaar, 2009; Paraskevopoulou et al., 2012).

2.5.3.1 Constitutive models for rocks

Although the mining infrastructure excavation process happens in 3D, it is often simplified by opting for the use of 2D finite elements due to the complexity of the problem. To be able to analyze what impact have mining infrastructures on an outcrop, it is important to define and use accurately the appropriated constitutive models of failure. Therefore, they are one of the most important components of numerical solutions in practical engineering problems.

2.5.3.1.2 Failure criteria

Failure criteria are mathematical approximations representing models that allow estimating the strength and predicting the failure of a material (i.e. rock or soil) from its strength properties and applied stresses. These failure criteria are the basis of the empirical methods that allow the evaluation of the strength of a rock mass. According to Mehranpour & Kulatilake (2016), the main failure criterion for intact rock failure criteria: Mohr–Coulomb, Hoek–Brown, Modified Lade, Modified Wiebols and Cook, Mogi and Drucker–Prager. The most common rock failure criteria are The Mohr-Coulomb and Hoek and Brown criteria. Although the Mohr-Coulomb and Hoek-Brown criteria do not take into account the

intermediate principal stress, they are the most widely used criteria due to their simplicity on the one hand and their extensibility to rock masses on the other. An explanation of both is given below. In the case of this thesis, the Hoek-Brown criterion has been used.

2.5.3.1.2.1 Mohr-Coulomb theory

The Mohr-Coulomb (MC) criterion is a mathematical model that describes the response of brittle materials to shear stress or normal strain, such as concrete, or particulate aggregates such as soil. According to Nadai (1950), the MC criterion is based on the two theories that give it its name, on the one hand, it is based on Mohr's condition that assumes that failure depends only on σ_I and σ_{III} , and the shape of the failure envelope, σ , τ acting on a failure plane, can be linear or nonlinear (Labuz & Zang, 2012; Mohr, 1900). On the second hand, Coulomb's condition is based on a linear failure envelope to determine the critical combination of σ , τ that will cause failure on some plane (Coulomb, 1776; Labuz & Zang, 2012).

The Mohr-Coulomb failure criterion is represented by the linear envelope of the Mohr circles that occur at rupture. The relation of that envelope is expressed as follows in Equation 2.54 (Coulomb, 1776).

$$\tau = \sigma \tan(\phi) + c \quad \text{Equation 2.54}$$

Where τ is the shear strength, σ is the normal stress, c is the intercept of the failure envelope with the τ axis, and $\tan(\phi)$ is the slope of the failure envelope. The quantity c is often called the cohesion and the angle ϕ is called the angle of internal friction.

MC criterion can be written as a function of major σ_I and minor σ_{III} principal stresses, or normal stress σ and shear stress τ on the failure plane (Jaeger et al., 2009). Equations 2.55 to 2.58 describes the criterion. When all principal stresses are compressive, experiments demonstrate that the criterion applies well to rock, where the uniaxial compressive strength is much greater than the uniaxial tensile strength (Labuz & Zang, 2012).

Therefore:

$$\sigma = \sigma_m - \tau_m \sin \phi \quad \text{Equation 2.55}$$

$$\tau = \tau_m \cos \phi \quad \text{Equation 2.56}$$

Where:

$$\tau_m = \frac{\sigma_1 - \sigma_3}{2} \quad \text{Equation 2.57}$$

$$\sigma_m = \frac{\sigma_1 + \sigma_3}{2} \quad \text{Equation 2.58}$$

Some modification is needed when tensile stresses act because the theoretical uniaxial tensile strength predicted from MC is not measured in experiments (Labuz & Zang, 2012).

2.5.3.1.2.2 Hoek and Brown criterion

In 1980, Evert Hoek and E. T. Brown developed the criterion for the design of underground excavations (Hoek & Brown, 1980). The Hoek-Brown failure criterion is an empirical criterion used in rock mechanics to predict rock failure (Hoek & Brown, 1990). The main idea of the Hoek-Brown criterion was due to the existence of joints in the rock to be able to weigh the intact properties of the rock by adding factors that reduced those properties. Furthermore, including a quantification of the relationship between the stress state and the Bieniawski rock mass ratio (RMR) (Bieniawski, 1989, 1993). In 1988, the criterion was extended to apply to slope stability and surface excavation problems (Hoek & Brown, 1988) and in 2002 an update of the criterion was presented that included improvements in the correlation between the model parameters and the geological strength index (GSI) (Hoek et al., 2002). Nowadays, the Hoek-Brown failure criterion is extensively used in mining engineering design (Bastidas et al., 2022; Lawongkerd et al., 2022).

Following there are shown the equations for the generalized Hoek and Brown criterion (Equation 2.59 – 2.62) :

$$\sigma_1 = \sigma_3 + \sigma_{ci} \left(m_b \frac{\sigma_3}{\sigma_{ci}} + s \right)^a \quad \text{Equation 2.59}$$

Where m_b , s , and a are the rock mass material constants, given by:

$$m_b = m_i \exp[(GSI - 100)/(28 - 14D)] \quad \text{Equation 2.60}$$

$$s = \exp[(GSI - 100)/(9 - 3D)] \quad \text{Equation 2.61}$$

$$a = \frac{1}{2} + \frac{1}{6} \left(e^{-\frac{GSI}{15}} - e^{-\frac{20}{3}} \right) \quad \text{Equation 2.62}$$

2.6 Global Positioning System (GPS)

The Global Positioning System is a satellite navigation system and it is the only system that can determine your exact position on earth at anytime, anywhere and in any air. These satellites were built and placed in orbit by order of the U.S. Department of Defense. The first GPS satellite was placed in Earth orbit in 1978, some 44 years ago. This system was initially prepared for military use, but from 1980 onwards it was released for public use and finally, in 1994, a network of 24 satellites was formed, the number of which has now reached 31 (Vatansever & Butun, 2017).

The services of this system are available in any meteorological conditions and any part of the world at any time of the day and night. The high accuracy of this system and its universality is one of the reasons why it is used in various sciences. This system became operational in 1983 with the launch of the first GPS satellite. With the implementation of the GPS system, all previous satellite positioning systems were gradually withdrawn. GPS is an operational and always ready system that is effective in all weather conditions, the frequency of the waves sent by GPS satellites is in megahertz, and weather conditions do not affect these waves. This system is active 24 hours a day and the location can be determined by it at any time and in any place. However, their position can be accurately determined 24 hours a day and anywhere in the world. Therefore, nowadays, anyone with a GPS receiver can be able to get freely an accurate GPS signal (Vatansever & Butun, 2017).

Currently, the 31 active GPS satellites, which are located in an orbit 20.200 km above the Earth and are continuously monitored by ground stations around the world. Each of these satellites called NAVSTARs, weighs approximately 1 kg. These satellites, which cover the entire surface of the Earth at the same time, are divided into 6 orbit planes, they have an inclination of 55° , the orbit radius is 26600 km, and the orbit period is 12 hours. Therefore, every 24 solar hours during the day and night, the satellite passes over the horizon of a place twice. As we know, solar day and night are 4 minutes longer than astronomical day and night, so each day the satellite is 4 minutes ahead of the previous day. The orbit of the satellites places them between 60 degrees north latitude and 60 degrees south latitude. This means that signals from the satellite can be received anywhere on Earth at any time. The power consumption of each satellite is less than 50 watts. These satellites obtain their energy from the sun through solar batteries, each of which measures 5.5 meters. They also carry batteries for times of solar eclipse or when moving in the Earth's shadow (Blewitt, 1997).

2.6.1 The GPS segments

According to Li et al., (2010), There exist four GPS segments.

- the Space Segment: includes the constellation of GPS satellites, which transmit the signals to the user.
- the Control Segment: Responsible for the supervision and operation of the Space Segment.
- the User Segment: Includes the user hardware and processing software for positioning, navigation and timing applications.

- the Ground Segment: Includes the civilian tracking networks that provide the User Segment with reference control, accurate ephemerides and real-time services (DGPS).

2.6.2 How the GPS system work

Position can be determined by two main methods, the GPS positioning, and GPS point positioning. The first one is based on trilateration, which is the method of determining position by measuring distances to points at known coordinates. At least, trilateration requires 3 ranges to 3 known points. On the other hand, the second one requires 4 "pseudorange" to 4 satellites (Vatansever & Butun, 2017).

2.6.3 GPS Satellite hardware

There are 31 GPS satellites, but this number is variable due to the launch of new satellites to replace older decommissioned satellites. All the prototype satellites, known as Block I, have been decommissioned. Between 1989 and 1994, 24 Block II satellites were put into orbit (1989-1994). Starting in 1995, these began to be replaced by a new design known as Block IIR. The nominal specifications of the GPS satellites are as follows

- Life target: 7.5 years
- Mass: ~1 ton (Block IIR: ~2 tons)
- Size: 5 meters
- Power supply: solar panels 7.5 m² + Ni-Cd batteries
- Atomic clocks: 2 rubidium, 2 cesium

The orientation of the satellites is constantly changing, so that the solar panels face the sun and the antennas face the center of the Earth. Signals are transmitted and received by satellite via microwaves. The signals are transmitted to the user segment at frequencies L1 = 1575.42 MHz and L2 = 1227.60 MHz. The signals are received from the Control Segment on frequency 1783.74 MHz. The information flow is as follows: the satellites transmit signals to the user, which are encoded with information about their clock times and positions. These signals are then tracked by the Control Segment through receivers located at special tracking stations. This information is used to improve the positions of the satellites and predict where they will be in the near future. This orbital information is transmitted to the GPS satellites at 1783.74 MHz, which in turn transmits it to the users, and so on. The orbital information on board the satellite is updated every hour (Blewitt, 1997).

2.6.4 How the position of satellites is known

Each satellite transmits a signal in the direction of the Earth. The user's GPS receivers can read the encoded signal through the "Navigation Message". It is included in the message the orbit parameters, usually called the "broadcast ephemeris", from which the receiver can calculate satellite coordinates (X, Y, Z). These coordinates are Cartesian in a geocentric system, known as WGS-84, which has its origin at the Earth centre of mass, Z axis pointing towards the North Pole, X pointing towards the Prime Meridian, which crosses Greenwich, and Y at the right angles to X and Z to form a right-handed orthogonal coordinate system. The algorithm which transforms the orbit parameters into WGS-84 satellite coordinates at any specified time is called the "Ephemeris Algorithm," which is defined in GPS textbooks (Leick 1991; Blewitt, 1997).

It should be aware that the time at which the signal is transmitted is encoded in the signal, using the time according to an atomic clock on board the satellite. The time at which the signal is received is recorded by the receiver using an atomic clock. The receiver measures the difference between these times.

$$\text{pseudorange} = (\text{time difference}) \times (\text{speed of light}) \quad \text{Equation 2.56}$$

The Navigation Message gives the satellite clock error, in polynomial form. The user can estimate the unknown station coordinates together with the unknown receiver clock error. Since there are 4 unknowns, a minimum of 4 pseudorange measurements are needed (Blewitt, 1997).

2.6.4.1 Example of Calculation of user position

Considering four satellites the user position in three dimensions (x,y,z) can be measured following the equation 2.57.

$$\rho_j = \|s_j - u\| + ct_u \quad \text{Equation 2.57}$$

Where j, which refers to the satellite, changes from 1 to 4. Equation (2-8) expands to a series of equations with y unknowns:

$$\rho_1 = \sqrt{(x_1 - x_u)^2 + (y_1 - y_u)^2 + (z_1 - z_u)^2} + ct_u \quad \text{Equation 2.63}$$

$$\rho_2 = \sqrt{(x_2 - x_u)^2 + (y_2 - y_u)^2 + (z_2 - z_u)^2} + ct_u \quad \text{Equation 2.64}$$

$$\rho_3 = \sqrt{(x_3 - x_u)^2 + (y_3 - y_u)^2 + (z_3 - z_u)^2} + ct_u \quad \text{Equation 2.65}$$

$$\rho_4 = \sqrt{(x_4 - x_u)^2 + (y_4 - y_u)^2 + (z_4 - z_u)^2} + ct_u \quad \text{Equation 2.66}$$

Where x, y, z, j determines the position of the satellite in three dimensions. These non-linear equations can be solved by using one of the following three methods: Closed-form solutions, linearization and Kalman filter method (Cooper & Durrant-Whyte, 1994; Grafarend & Shan, 2002).

2.6.5 Differential GPS methodology (DGPS)

This method requires at least two GPS receivers that have a line of sight to the same satellites. It also requires an additional antenna for the DGPS receiver to record the GPS signal. The concept behind this process is that two nearby receivers will have similar atmospheric errors. One of the receivers needs to be precisely fixed in a known position, it will be called a reference or base station and it calculates its "position" based on the received GPS signals. It calculates the difference between the measured position and the actual position and transmits the correction data to the nearby DGPS receiver. This system can provide an accuracy of one meter (Vatansever & Butun, 2017).

2.7. InSAR Technique

According to the European Space Agency (Ferretti et al., 2007), Synthetic Aperture Radar Interferometry is a technology that has been proposed and used as an effective tool to study the phenomena that cause any type of ground movements or change, some natural examples are earthquakes, volcanoes, glaciers, landslides, salt diapirs, floods, some anthropic examples are the release of underground water and oil, underground collapses, fires, or even plant growth. Therefore, its applications include investigating and identifying natural and human hazards (Antonielli et al., 2021; Hussain et al., 2022; Zhang et al., 2022).

The basis of this methodology is the use of phase information of the radar reflection from the ground so that the changes created on the ground surface cause a phase difference in the two radar images. Therefore, it is required to capture in two different times the same area (Ferretti et al., 2007).

Interferometric Aperture Radar or InSAR is a technology that was invented to study the ground surface movements after the 1992 Landers, California earthquake, using ERS-1 images, which were taken over several months, it was possible to obtain an image that shapes changes due to the earthquake. Since then, many works have been done using the images of JERS, ERS, Space Shuttle, SIR-C, X-SAR and RADARSAT satellites to study earthquakes, volcanoes, glaciers, landslides, land subsidence and border deformation (Massonnet & Feigl, 1998).

2.7.1 Synthetic Aperture Radar

The Synthetic Aperture Radar (SAR) radar system uses an antenna beam in the direction perpendicular to the direction of movement and has high accuracy in the angle. The output of SAR technology is a high-precision image. Due to the creation of accurate images, this type of radar has many applications in geology and geography as well as in military affairs (Ferretti et al., 2007; Moreira et al., 2013).

In the SAR system, the radiation and reception of the signal take place in almost the same place in space, the reactions that are important in the SAR geometry are the reflections of the radiated radar waves. This type of interaction is called backscattering. The transmitted signal and echo received from a specific scatterer consists of two components, amplitude and phase. The echo range is determined by the efficiency of the scatterer and the geometrical factors of the system. In the simple scattering reaction, the echo phase is determined from the phase of the transmitted signal, the dielectric properties of the environment and the location of the scatterer relative to SAR. The SAR receiver records information from the ground and splits it into separate echoes. Echo or returning waves are created by the effect of scatters. The surface of the earth is made up of scatters, which are objects, such as trees, earth, and ice, which react with radio waves emitted from the satellite (Chen, 2016).

Two different imaging mechanisms are used in the SAR system. First, each radiated pulse sweeps the surface of the earth to the width of the swath. In this case, perpendicular to the satellite's flight path, the earth reflects the energy to the radar. Because the earth is formed by a continuous range of scatterers, the reflected energy is continuous as an echo. This echo is digitized at the same time as the sampling frequency. In the second mechanism, the imaging of the targeted area is in the direction of flight and the speed vector of the satellite platform is digitalized. The time scale of the cross-track and along-track systems has a difference that makes it possible to separate them. The raw SAR data and the subsequent corrected SAR data are in the form of a two-dimensional matrix whose coordinates include the range R , the distance from the SAR and the azimuth X representing the location of the scatterer in the direction finder. The name of the ground range is used for the range component in the Y direction. The two-dimensional components of the matrix form a pixel or image component. About raw SAR data, complex values are assigned to each pixel, which consists of phase and amplitude, or real or image components (Ferretti et al., 2007). Figure 2.32 shows the geometric parameters of the SAR methodology.

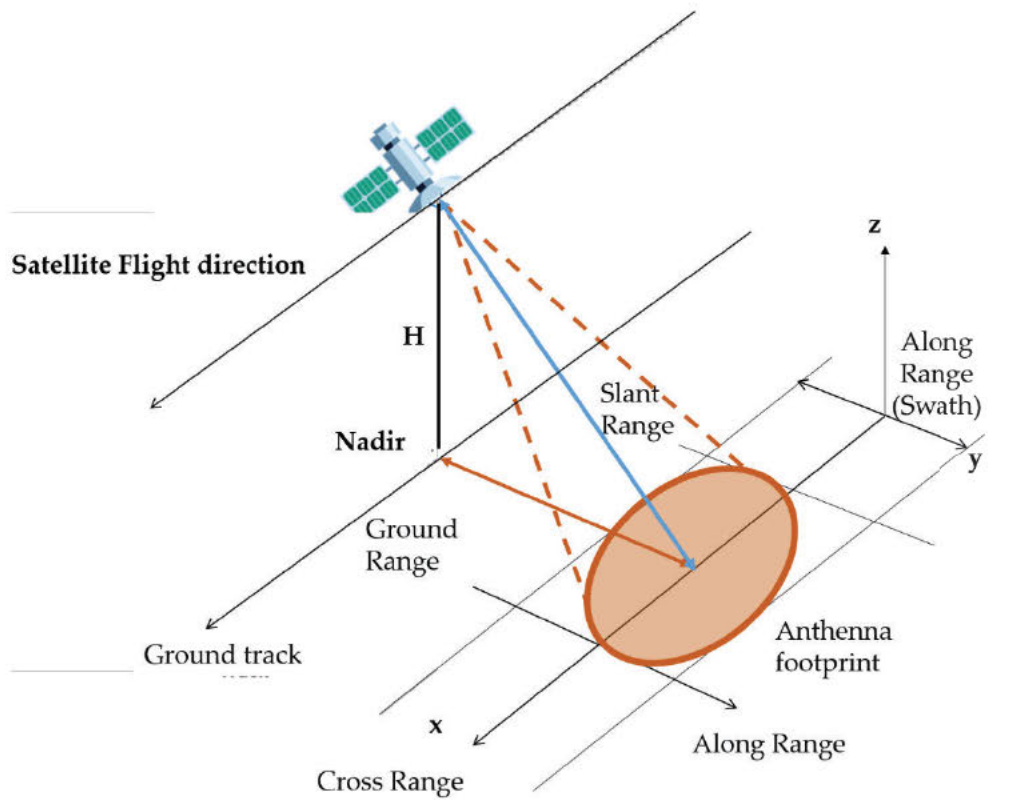


Figure 2.32 The geometry of the SAR system (Adapted from Bamler & Hartl, 1998 and Laukness, 2010)

2.7.2 Interferometric Synthetic Aperture Radar

The basic idea of SAR interferometry is to develop a comparison of the phase of two or more radar images of a given scene acquired from slightly different positions or at different times. SAR interferometry allows precise measurement of surface topography, ground deformation and subsidence, with centimeter accuracy (Sanmiquel et al., 2018). It is based on the processing of a pair of images and the result is a map of the differences of the reflected signals in a specific area.

The technology combines data obtained from radar imaging systems installed on satellite or aircraft platforms. The basis of this technology is to measure ground surface movements using repeated radar images. An image taken from a region at a specific time or also called reference time is combined with an image taken at another time by the same radar sensor. Therefore, by examining this phase difference and modeling it, surface changes on the ground can be quantified.

Using the stereoscopic effect caused by differences in the position of observation between the two images, interferograms can be used to produce digital elevation maps (DEMs). By using two images produced by the same sensor with a separation in time, other phase contributions, such as atmospheric effects, must be assumed to be minimal. Different approaches have been developed during the

development of the technology. One type consists of flying two satellites in tandem with a separation of one day for this purpose. A second approach consists of using two antennas mounted at a certain distance on the same platform and acquiring the images at the same time, which guarantees the absence of atmospheric or deformation signals. InSAR DEMs can be used for subsequent two-pass deformation studies or other geophysical applications (Bürgmann et al., 2000; Madsen & Zebker, 1992).

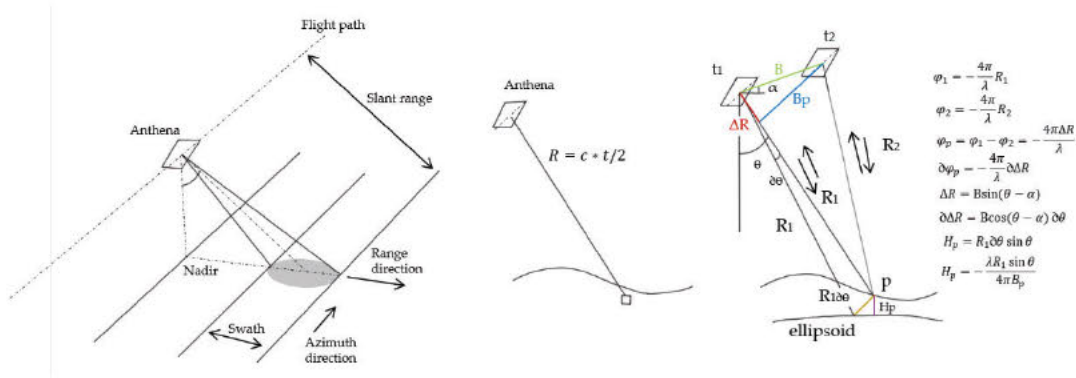


Figure 2.33 SAR imaging geometry and InSAR geometry. R is the inclination range (distance between the radar and the target), P is the height of the point and is determined as H_p : topographic height, B is the baseline, distance from the orbit, B_p is the perpendicular baseline, which is the projection of the baseline perpendicular to the inclination range, θ is the look angle of the satellite. (Adapted from UN, N.D)

In the above figure, the height of the first sensor from the ground is H, and the angle of view (radiation) is its radar. The distance between the flight paths is called the baseline (B) and its perpendicular component relative to the radar line to the ground structure is called the effective baseline or perpendicular. The angle of the baseline with the horizon is (α) (Pepe & Calò, 2017). Equation 2.67 expresses that for a SAR pixel whose center is located in the range R and azimuth x:

$$s(R, x) = |s(R, x)| e^{j\phi(R, x)} \tag{Equation 2.67}$$

Where ϕ is the resulting phase for the pixel. As mentioned earlier, the phase is random due to the many scatterers present in the separation element. However, due to the movement between the radar and the ground, the phase depends only on the distance and the refraction characteristic of the atmosphere at the radar wavelength, which is assumed to be the same at this time (Equation 2.68):

$$\phi(R, x) = \frac{-4\pi}{\lambda} R + \phi_{scat}(R, x) \tag{Equation 2.68}$$

The first term on the right side is the phase relationship resulting from the circular path between the sensor and the center of the separation element and the scattering phase ϕ_{scat} . Two SAR co-registered images will have similar pixels in each image will correspond to a similar point on the ground. Interference is obtained from the corresponding combination of two SAR images from the same area (Equation 2.69), and the interferometric phase is equal to (Equation 2.70):

$$i = s_1(R_1, x_1) s_2^*(R_2, x_2) = |s_1(R_1, x_1)| |s_2(R_2, x_2)| \exp(j\phi_{int}(R_1, R_2, x_1, x_2)) \quad \text{Equation 2.69}$$

$$\phi_{int}(R_1, R_2, x_1, x_2) = \frac{-4\pi}{\lambda} \Delta R + \phi_{scat,1}(R_1, x) - \phi_{scat,2}(R_2, x) \quad \text{Equation 2.70}$$

By simplifying and assuming $\phi_{scat,1}$ is equal to $\phi_{scat,2}$, a residual noise phase will appear due to the difference in radiation angles of both acquisitions (Equation 2.71).

$$\phi_{int} = \frac{-4\pi}{\lambda} \Delta R + \phi_{noise} \quad \text{Equation 2.71}$$

In addition, other sources of noise phases may exist and there is more information on the relative size of ϕ_{noise} . The phase difference for any point on the earth in the interference view is a number that changes between zero and 360 degrees. The adjacent ground point obtains another value of the phase difference, which indicates the specific effect of the path change.

In addition, other sources of noise phases may exist. For example, in a set of points on the ground, the 360-degree range of phase change can be displayed with 256 grey levels and as fringes with different levels. An interference image is made of a large number of such fringes. A fringe can be considered a set of counters, each of which represents a single grey level. The fixed phase difference in a fringe is directly related to the fixed path difference. In other words, the path difference is also a function of the height of the earth, because it affects the distance between the earth and the satellite. Therefore, the constant path difference can be attributed to the constant height.

According to Figure 2.33, having H and range information, if the angle is accurately known, z can be obtained for any point on the ground. Only by combining the information of the second SAR image, we can get the exact value and then z.

The geometry of SAR interferometric imaging is similar to stereographic images. However, SAR interferometry uses interferometric phase information instead of using stereographic techniques to determine the height. Based on the relations of cosines (Equations 2.71, 2.72):

$$\sin(\alpha - \theta) = \frac{(R_1 + \Delta R)^2 - R_1^2 - B^2}{2R_1 B} \quad \text{Equation 2.71}$$

$$z = H - R_1 \cos \theta \quad \text{Equation 2.72}$$

The value of the phase angle (and as a result the phase difference in an interferometer) varies from 0 to 360 degrees. To calculate the height model and the height of an area, the interference fringes should be folded. For example, an integer multiple of 360 degrees should be added to the phase difference in each pixel. If the ground is flat, the distortion of such interference leads to the creation of an image with a constant grey intensity. If the interference is from a mountainous area, the distortion will lead to an image with increasing grey intensity with increasing height.

2.7.3 Movement measurement

According to (Bechor & Zebker, 2006; Hu et al., 2014; Wegmüller et al., 1998), it is possible to calculate the movement measurement of two observations using InSAR technology. Although there may be differences in the amount and direction of motion, in a separating element, to maintain logical motion, the velocity vectors must be equal. This change requires a large-scale ground deformation of less than a kilometer, as in the case of events such as earthquakes, glacial movement, or subsidence. Equation 2.73 can describe the phase with the range change added directly to the interferometric phase as equal to:

$$\phi_{\text{int}} = \phi_{\text{topo}} + \phi_{\text{motion}} + \phi_{\text{noise}} \quad \text{Equation 2.73}$$

At the same time, the total interferometric phase includes topographical effects, earth ground movement, and atmospheric variable effects between observations and noise can be described as Equation 2.74.

$$\phi_{\text{int}} = \phi_{\text{topo}} + \phi_{\text{motion}} + \phi_{\text{noise}} + \phi_{\text{atmos}} \quad \text{Equation 2.74}$$

2.7.4 Surface displacement caused by natural events

The primary application of SAR interferometry is topography estimation. Nevertheless, one of the advanced applications of this method is in identifying surface displacement caused by natural events such as earthquakes and landslides, subsidence or unnatural ones such as subsidence caused by groundwater extraction. In this method, SAR images are used at two different times to identify the surface displacement in that period. First, an interferometer is created and with it the topography before the accident is determined. Then, the interference shows the second view of the topography after the phenomenon

happened. By differentiating one interference view from another, the fringes related to the usual topography are removed and what remains is the change created in the topography or displacement. Some examples can be found in (Wang et al., 2020; Wegmüller et al., 1998). Nowadays, there are two methods for differential interferometry.

The first option is by using three, or more, data sets. In this method, an interferometer uses the phase difference of the first and second images and the interferometer of the second image. The phase difference between the second and third images is created. Then, the resulting two interference views are separated so that the interference of the differential view is obtained.

A second option can be by using two sets of data, together with an elevation model. In this method, the interference of the view is created by using an initial digital elevation model (and accurate satellite location information at the time of imaging, orbital vectors). Then, the interference of the next view is subtracted from the interference of the initial view to eliminate the effect of the height of the ground. Therefore, what remains indicates change or displacement. Figure 2.35 shows the steps of forming a surface displacement map.

2.7.5 Background of the study of subsidence in the CPB

It is known that the Catalan Potash Basin is undergoing a process of subsidence. Therefore, in 2008 a study was started to control the speed of it. Determining the horizontal and vertical displacements of the land areas affected by the mines, located in the Súria area (Pou4- Cabanasses mines) and Sallent-Balsareny area (Vilafruns mine). For this purpose, a combination of two methodologies will be used, Global Navigation Satellite System (GNSS) and Interferometric Synthetic Aperture Radar (InSAR).

The methodology applied until the 2016 campaign was based solely on the topographic measurement of a total of 1200 control points between the two defined zones, defining 600 control points in Súria and 600 control points in Sallent-Balsareny. The design of the campaigns was biannual, so it was defined that in odd years the control points in the Súria area would be controlled and in even years the Sallent-Balsareny area would be controlled.

Since the 2017 campaign, it was decided to use a combination of two methodologies. On the one hand, the classic topographic measurement is based on a Global Navigation Satellite System (GNSS), using dual frequency receivers; and on the other hand, the differential interferometry DInSAR. This combination made it possible to reduce the number of control points to be measured topographically in each zone, therefore, from 2017 onwards, points in both zones

can be measured annually. Currently, in 2022, 78 control points were calculated in the Sallent area and 145 in the Súria area.

The coordinates of these points are calculated with the post-processing software called Magnet Tools and, then, compared with the coordinates available from the previous year's campaign. MAGNET Tools (TOPCON) is a topographic software that allows the processing and adjustment of topographic survey data collected from total station and GNSS equipment.

2.7.5.1 Methodology used to quantify the subsidence produced in the CPB

Considering 600 control points in the targeted area and an accuracy altitude and precision altitude should be ± 2 cm, it was determined together with the ICGC that the method that best adapted to these requirements was a method based on a Global Navigation Satellite System (GNSS), specifically, the method that uses "the static differential in post-processing", based on 2 dual-frequency receivers located at 2 points of known coordinates (base receivers), and the other 2 receivers (mobile receivers), also dual-frequency, located at 2 points to be measured. The minimum measurement time for each control point was determined to be about 12 minutes. It is very important that the receivers placed at the points to be measured coincide in time with the 2 base receivers placed at the 2 known points. This is because later, in post-processing, a triangulation is established from the data collected by the 2 receivers placed at known points and the data from the receiver or receivers located simultaneously at the points whose coordinates are to be calculated. The information stored by the GNSS receivers is processed in the work of the Cabinet as follows. First, the measured data is downloaded to the computer using the specific software called Topcon Receiver Utility (TRU). Then, the points are calculated in post-processing with the Magnet Tools (Topcon) software by least squares triangulation.

The two base points of Sallent, called Sallent and Vilafruns, and the two base points of Súria, called POU4 and Cabanasses or C1, are located within the company's facilities. The bases were built in concrete with a metal base with a forced centered screw. At the beginning of each campaign, the bases must be remeasured, since the 2 base points in the Súria area and the 2 in the Sallent area are affected by subsidence displacement due to mining activity. Until the 2019 campaign, the starting bases in the Súria area (Cabanasses or "C01" and "POU4") were remeasured from the geodetic vertices "Castelladral" and "El Putxot", located outside the zone of influence of the Cabanasses mine. On the other hand, the starting points in the Sallent area (Sallent and Vilafruns) were remediated from 2 geodetic points of known coordinates called "Puente" and "Torre", located

outside the zone of influence of the subsidence process generated by the Sallent mine.

From the 2020 campaign, due to the great evolution of the ICGC CatNet network, it was possible to supply data from the permanent GNSS stations of the same network. Thus, it was possible to recalculate the coordinates of the starting bases of the Súria area, and those of the Sallent area from the data downloaded from the ICGC website of 4 permanent GNSS stations coinciding in time with the measurements of more than 5 hours of duration of the indicated bases of Súria and Sallent. The measurement of these stations "C01" and "POU4" of Súria, and the bases "Sallent" and "Vilaforns", also with a measurement duration of more than 5 hours, is performed annually.

In both cases, the data per second of the selected period were downloaded from each of the 4 permanent GSS stations of the ICGC, coinciding with the times of the data measured together with the time of the GNSS receivers, in both cases. Then, the coordinates of the 2 bases of each enclosure were calculated, from the resolution of the Magnet Tools software, by least-squares Magnet Tools software, by the minimum squared method. The coordinates of the ICGC permanent GSS stations used to calculate the starting points for the Súria and Sallent areas are shown below.

2.7.5.2 Quality control methods

2.7.5.2.1 Software-based quality control method

The quality control methodology is based on the Magnet Tools post-processing software. To start the quality process, it is necessary to enter in the quality section of the software the value of 2 cm as the maximum tolerance. Therefore, in those points where the data set is not able to reach an error of less than 2 cm, a warning will be issued. Consequently, in these cases, it will be necessary to re-measure the control point in question. The causes of measurement errors may be due to:

- Human error due to improper leveling of the GNSS receiver.
- Signal interference between the receiver placed at a control point and the satellites of the constellations used due to the proximity of the control point to slopes, walls, trees, high-voltage power lines that can induce electromagnetic interactions, etc. In this case, the repetition of the measurements is performed twice. If the second repetition also fails to achieve the minimum required quality, the control point is eliminated.

2.7.5.2.1.1 Remediation of control points method

This method of quality control consists of measuring a randomly chosen point twice, 1 or 2 weeks apart to compare the two measurements and see if the difference in measurements is less than the established tolerance interval of $\pm 2-4$

cm (the most unfavourable case is that the point of the first week has an error of 2 cm to one side and in the second week also has an error of 2 cm but to the other side, therefore the total error). It is important not to exceed the measurement interval of 2 weeks, because if the control point to be analyzed is located in an area of strong subsidence, then there would be a danger that the detected coordinate difference is not due to any error, but to the subsidence process under analysis.

2.8 Terrestrial Laser Scanning Theory

The Earth's surface is subject to permanent topographic change. Terrestrial laser scanning (TLS) is a highly accurate sensor system increasingly used in Earth Sciences for observing such surface changes. From repeated data acquisitions, multitemporal 3D point clouds can be generated and used to quantify surface change over time (Eitel et al., 2016). During the last few years, terrestrial laser scanning has been widely used. The high speed of scanning, accuracy, higher productivity versus common geodetic methods (such as selective measurement of individual points by total stations), significant shortening of fieldwork, and automatic data processing into digital models make this technology almost irreplaceable in rapid speleological mapping. Another important advantage is the use of its source of a laser beam, which ensures hassle-free surveying in poorly illuminated, or even not illuminated underground spaces (Pukanska et al, 2020). TLS systems emit intense monochromatic, coherent, and high-directional radiation. Since the laser scanner used in this work is a long-range laser scanner, we used it as the main instrument for mapping and subsequent 3D modelling of the drifts from the Cabanasses ore deposit. Following, in Table 1, there are the specifications of the laser used, the BLK360 (Leica Geosystems).

Table 2.2 BLK360 product specifications (Leica Geosystem).

BLK360 PRODUCT SPECIFICATIONS	
GENERAL	
IMAGING SCANNER	3D scanner with integrated spherical imaging system and thermography panorama sensor system
DESIGN AND PHYSICAL	
HOUSING	Black anodized aluminium
DIMENSIONS	Height: 165mm
	Diameter: 100mm
WEIGHT	1 kg
OPERATION	
WIRELESS COMMUNICATION	Integrated wireless LAN (802.11 b/g/n)
INTERNAL MEMORY	Storage for > 100 setups

INSTRUMENT ORIENTATION	Upright and upside down
POWER	
BATTERY TYPE	Internal, rechargeable Li-Ion battery (Leica GEB212)
CAPACITY	Typically, >40 setups
SCANNING	
DISTANCE MEASUREMENT SYSTEM	High speed time of flight enhanced by Waveform Digitizing (WFD) technology
LASER CLASS	1 (in accordance with IEC 60825-1:2014)
WAVELENGTH	830 nm
FIELD OF VIEW	360° (horizontal) / 300° (vertical)
RANGE*	min. 0.6 - up to 60 m
POINT MEASUREMENT RATE	up to 360'000 pts/sec
RANGING ACCURACY*	4mm @ 10m / 7mm @ 20m
IMAGING	
CAMERA SYSTEM	15 Mpixel 3-camera system, 150Mpx full dome capture, HDR, LED flash Calibrated spherical image, 360° x 300°
THERMAL CAMERA	FLIR technology based longwave infrared camera Thermal panoramic image, 360° x 70°
PERFORMANCE	
MEASUREMENT SPEED	< 3 min for complete full dome scan, spherical image & thermal image
3D POINT ACCURACY*	6mm @ 10m / 8mm @ 20m
ENVIRONMENTAL	
OPERATING TEMPERATURE	+5 to +40° C

Figure 2.36 shows indicatively the different measurement techniques depending on the object size, in blue is located the case of the study. Considering typical deep excavations of sizes between 20 and 100 meters, and tunnels of between 10 meters to kilometers, it can be seen that both, close range photogrammetry and laser scanning, are at their higher end of applicability (Fuentes, 2010). Using TLS data holds the advantage that multiple analysts can perform the same digital measurements and take their time to fulfil the task. The measurement process also becomes more transparent as the survey conditions represented by the 3D point cloud can be revisited numerous times to increase consistency and develop best practices. Moreover, the sample size of the tunnel measurements through TLS is much larger than is possible by physical field measurements. Depending on the survey setup, the sample size increases by a factor of more than 100 000. It follows that the tunnel can be determined more accurately from the TLS data (Anders et al, 2020).

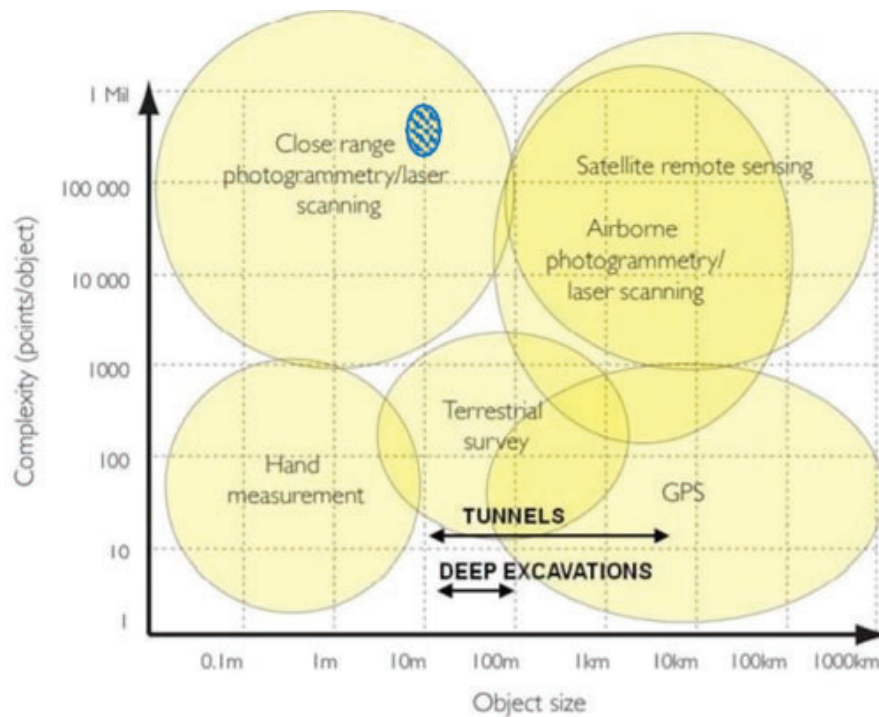


Figure 2.35 Different measurement techniques depending on the object size. (Fuentes, 2010), in blue located the study case.

The product of a laser scanner is eventually a Point Cloud. This consists of measured three coordinates for a number of points which are referred to as an origin defined by the scanner position at the time at which the scanner was taken (Fuentes, 2010). Terrestrial laser scanning can be applied to a wide variety of applications. Depending on the range distance to the measured object, applications can be divided into three different categories according to (Rics, 2006):

- Less than 1m - Sub-millimeter accuracies can be obtained
- Between 2 and 100 meters - Average accuracies of about 5mm
- Up to about 2 km - An accuracy of centimeters can be achieved. Typical applications in deep excavations and tunnels fall into the second category.

2.8.1 Basic principles

2.8.1.1 Parts of a terrestrial laser scanner

The pulsed laser beam is sent from the range finder electronics unit and meets the polygonal mirror element which rotates at a relatively high speed (Figure 2.37). The laser beam is reflected off the mirror surfaces such that it is scanned through the vertical angle ζ . After a ζ profile has been recorded, the upper part of the instrument rotates through a small angle $\Delta\alpha$ in order to sample the neighbouring ζ profile, and so on until a full horizontal circle has been covered. In terrestrial laserscanning, the object is scanned from several measurement stations

such that there is only a small overlap between the point clouds generated at each station. GPS can well serve the purpose of locating these stations. From one station one obtains the polar coordinates α , ζ and s . The data recorded from one station is, in terrestrial laser scanning, normally called a scan (Kraus, 2004).

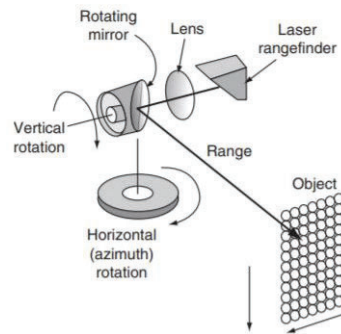


Figure 2.36 Operating diagram of a terrestrial laser scanner (Shand and Tooth, 2008)

The theoretical principles that apply to terrestrial laser scanning are different depending on the type of technology that is being used. According to Fuentes et al (2010), Laser scanners can be divided into three categories, depending on the technology they use to carry out the scan. Table 2 shows these different types, their typical applications and accuracies and operating ranges. As can be seen in Table 2.3, for small objects at very close range, the triangulation scanners are the best suited. However, these have seen little application in civil engineering. On the other hand, they would in principle be feasible for crack monitoring and laboratory work. Their economic viability against other more traditional methods needs further assessment. Phase shift scanners offer traditionally the greatest speeds of data capturing, whereas their accuracies are at least comparable to the time of flight scanners. However, their range is still somewhat shorter than that offered by the time of flight-based scanners:

- Triangulation: this technique consists in using a laser which sends light into an object via a mirror. Distances can be calculated by triangulation, using the reflection of the laser beam from the scanned object that will reach the sensor, located at a known distance from the mirror.
- Time of flight: It measures the time that it takes for the light since it is emitted by the instrument until it comes back to the sensor after having reflected in the object. From this time, and knowing the speed of light, the distance can be calculated.
- Phase shift comparison: The laser emits light in three different phases and compares continuously the differences between the emitted light and the returned light. It uses the differences to calculate the distance.

Table 2.3 Three categories of scanning laser (Fuentes, 2010).

Scanning System		Application	Typical accuracy/operating range
Triangulation	Rotation stage	Small objects for reverse engineering or replicas	50 microns 0,1m – 1m
	Arm mounted	Small objects and surfaces	50 microns 0,1m – 1m
	Mirror/prism		Sub-mm / 0,1m – 25m
Time of Flight		Deformation monitoring / building facades 3D models and surveying/tunnel surveys and deformation monitoring	3-6 mm at ranges up to 100m / 2m – 100m
Terrestrial phase shift		Deformation monitoring / building facades 3D models and surveying/tunnel surveys and deformation monitoring	5 mm at ranges up to 2m / 2m – 50m

The point cloud that is obtained from the scanner at the time of monitoring sometimes needs to be coordinated to a useful coordinate system for monitoring purposes. This process is called scan coordinates transformation. Furthermore, since a monitoring campaign would normally consist of more than one scanning position to enable good coverage of the whole site, the different point clouds need to be merged. This process is known as Registration (Fuentes, 2010).

2.8.1.2 Measurement principle

A laser scanner consists of a transmitter/receiver of the laser beams, a scanning device and a timing device (Fig 2.75). The scanner sends out laser pulses and then receives and records the reflected signals. The timing device measures the time of flight (Δt) with which the scanner can compute the distance d , where c stands for light speed (Wang et al, 2014).

$$d = \frac{c\Delta t}{2}$$

Equation 2.75

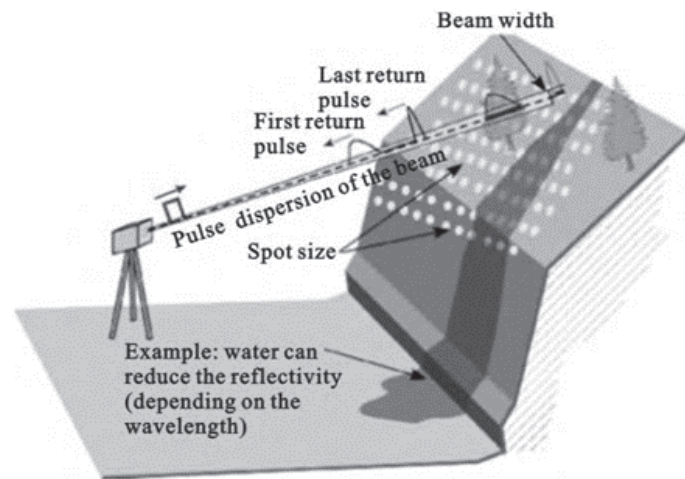


Figure 2.37 Example of basic principles of terrestrial laser scanner data acquisition (Wang et al, 2014).

Knowing the direction and the angle of the light ($\cos(\alpha)$, $\cos(\beta)$, $\cos(\gamma)$) allows determining the relative position x , y , z (Equations 2.76, 2.77, 2.78) of a reflective surface to the device (Wang et al, 2014).

$$x = d\cos(\alpha) \tag{Equation 2.76}$$

$$y = d\cos(\beta) \tag{Equation 2.77}$$

$$z = d\cos(\gamma) \tag{Equation 2.78}$$

2.8.1.3 Georeferencing

According to Kraus (2004), the laser scanner's position (X_0, Y_0, Z_0) , for example with the help of GPS in static mode, and angular orientation (ω, ψ, κ) have been determined. From these parameters, and the polar coordinates α, C, s , the X, Y , and Z coordinates in a global coordinate system can be derived as in equation 2.79:

$$\begin{pmatrix} X \\ Y \\ Z \end{pmatrix} = \begin{pmatrix} X_0 \\ Y_0 \\ Z_0 \end{pmatrix} + R_{\omega\phi\kappa} \begin{pmatrix} s \sin \zeta \cos \alpha \\ s \sin \zeta \sin \alpha \\ s \cos \zeta \end{pmatrix} \tag{Equation 2.79}$$

ζ *zenit angle with zero direction along κ axis*

α *horizontal angle, with zero direction defined by the zero direction for κ rotation*

It is particularly noticeable that no synchronization of the transformation parameters is required in terrestrial laser scanning and that the polar coordinates are derived from two deflection angles. If the location coordinates and orientation angles are unknown (free stationing), then these parameters must be determined indirectly from control points (indirect sensor orientation). In this

regard, we initially assume that, in every station scan, a number of control points can be located and identified by small retro-reflecting targets, due to the high contrast between these targets and their environment, the signals can be automatically identified in the intensity image.

After scanning and location of the control points, and using the 4 nearest scanned points, the coordinates can be determined by means of a bilinear transformation. The transformation parameters X_0, Y_0, Z_0 and ω, φ, κ for one measurement station can be determined from at least 3 well distributed control points.

The advantage of indirect sensor orientation can be appreciably increased by simultaneously connecting all scans in a measurement project. For the full set of scans, only a few more control points need to be determined in the object coordinate system. To connect scans, retro-reflecting targets are again required which can, however, be automatically found and identified in their overlapping areas. Figure 2.39 illustrates three scanner stations connected through common measured points. After converting polar coordinates to Cartesian coordinates (Equation 2.80), each scan has its own local Cartesian coordinate system (Figure 2.39 shows this only for the middle station). In addition, Figure 2.39 shows the global X, Y, and Z object coordinate in which a number of retro-reflecting control point targets must be measured.

$$\begin{pmatrix} X \\ Y \\ Z \end{pmatrix} = \begin{pmatrix} s \sin \zeta \cos \alpha \\ s \sin \zeta \sin \alpha \\ s \cos \zeta \end{pmatrix} \tag{Equation 2.80}$$

The indirect sensor orientation for a complete set of scans, each with local Cartesian coordinates derived from the original polar coordinates, corresponds to the spatial block adjustment with independent models.

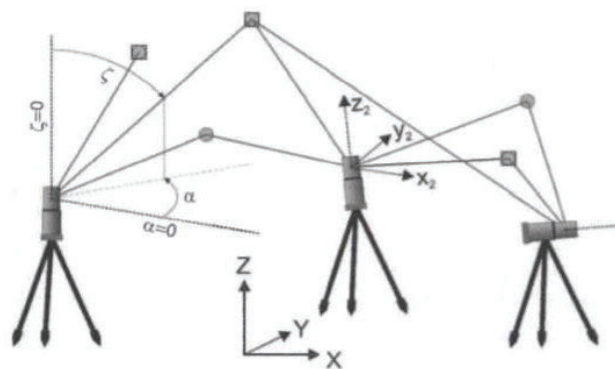


Figure 2.38 Connection of multiple laser scanning stations (Kraus, 2004)

2.8.1.4 Data collection

Rics (2006) presented the main aspects to be considered in data collection:

- Type, size and number of targets needed for coordinate transformation and registration.
- Scanning positions to avoid gaps in the data.
- Stability of the scanning stations.
- Document the survey with photographs that will aid significantly in the scan interpretation.
- Health and Safety considerations.

The determination of the data collection positions is critical to the success of the project. The requirements of the survey are on some occasions in conflict with some of the other activities on site. Since exact planning is impossible on a construction site, it is recommendable to have some redundancy in the scans at the expense of more data to be managed. However, the amount of data must be manageable and computing power will need to be provided in order to cater for this. A further reason to have some redundancy in terms of the number of positions is the reduction of the possibility of obstruction moving plant, materials and people; by taking more scans it is very likely that a moving plant will have changed position and therefore the obstructed part will be covered (Fuentes, 2010).

The presence of gaps in the point cloud in a scan can only be remediated through a number of assumptions, which in most cases reduce the accuracy of the measurements and their reliability, depending on the size of these gaps. The assumptions vary from surface extension and extrusion of points to the creation of additional data. In deformation monitoring, gaps in the point cloud of the structure being monitored are generally not acceptable (Fuentes, 2010).

Documentation of the survey is always good practice; recording positions, date and time of the day, etc. Although important in laser scanning, documenting the survey with photographs taken at the same time helps with the interpretation of the point clouds and readings extraction (Fuentes, 2010).

2.8.1.5 Point Cloud Registration

For the initial processing and editing of the scanned data, a professional 3D point cloud processing software Leica Cyclone version 7.3 (Leica Geosystems AG, Heerbrugg, Switzerland, 2011). was used. For the subsequent editing and modelling, the following software was used the point cloud processing and analysis software Leica 3DR version X (Leica Geosystems AG, Heerbrugg, Switzerland, 2011).

There are typically five different methods that can be used to carry out the registration of different scans, these are (Fuentes, 2010):

- Survey the position of the scanner (i.e. coordinate the origin of the point cloud).
- Use control targets.
- Use natural features.
- Use surface matching algorithms.
- Other algorithms (such as Iterative Closest Points - ICP).
- Combination of two or more of the above.

The most common system is the use of targets, which is applied in this study case. A good spread of the targets over the whole measured site is desirable. A typical point cloud processing software would provide an estimate of the accuracy of the registration process (Fuentes, 2010).

Chapter 03

Materials and methods

“Put your heart, mind, and soul into even your smallest acts. This is the secret of success.” — Swami Sivananda

3. Materials and Methods

3.1 Subsidence Management and Prediction System

An analysis was carried out to process and analyze the measured subsidence data and, subsequently, create a numerical model to predict the surface subsidence of a case study mine. The model was developed based on a finite element method (FEM). It was achieved by considering the geological characteristics of the area, the design features of the mine, the surface subsidence measured over twelve years and the time-dependent behavior of the geological layers. Figure 3.1 represents the methodology followed to obtain the average surface subsidence profile. The characteristics of the case study are in brackets.

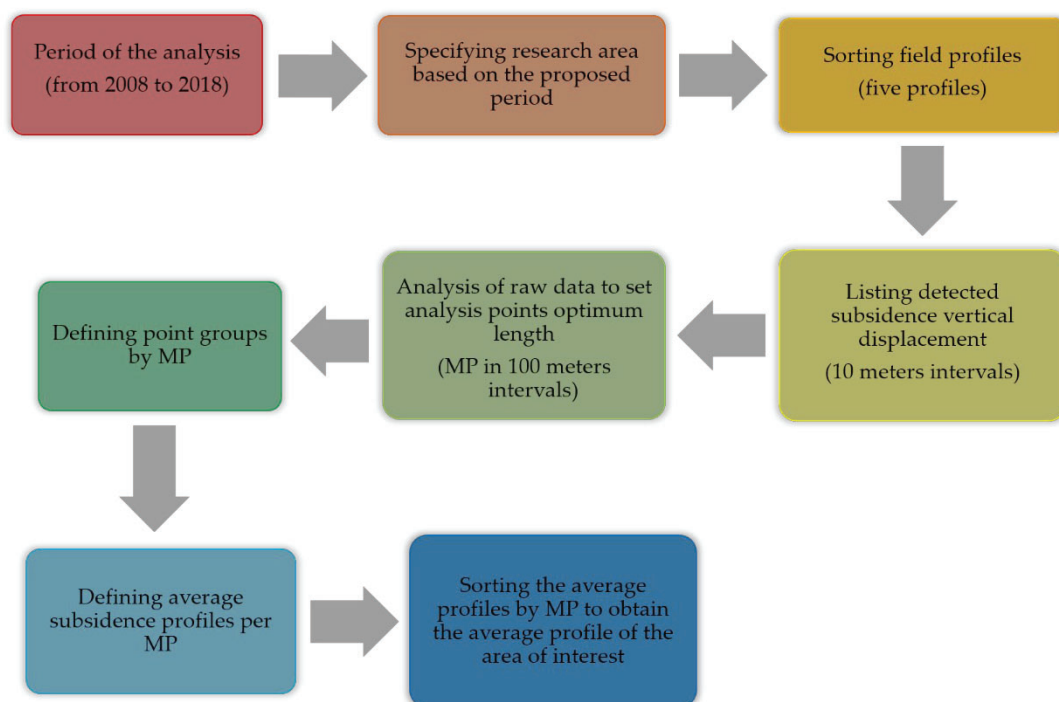


Figure 3.1. The methodology followed to reach the average surface subsidence profile.

The method used to model the geomechanical behavior of the potassic deposit through the finite element method is detailed below. It is divided into 7 sections; GPS and InSAR technology, the definition of the Targeted area, development of the subsidence average profile, numerical model design, design of mining drifts, numerical model definition, and Young's modulus decreasing methodology.

3.1.1 GPS and InSAR technology

The case study has 700 control points in an area of 50 km², with measurements from 2008 to 2021. The control points are distributed throughout the geographical area potentially affected by subsidence, obtaining the X, Y and Z coordinates of

each point by GPS. The method used to obtain the coordinates in post-processing is based on the use of four static differential GPS with dual frequency receivers. This method requires locating two receivers at two points of known and well-established coordinates, while the other two receivers are used to take measurements at the control points, with a minimum measurement time per point of 12 minutes. This methodology guarantees an accuracy of 1-1.5 cm in planimetric and altimetric coordinates, which implies that the maximum possible error between measurements of the same point is 2-3 cm. Consequently, only differences greater than these errors are relevant to indicate whether subsidence is present. Periodic quality control measurements are made to verify the reliability of the measurements.

Since 2016, InSAR images are also used as an additional monitoring system. However, the surface characteristics of the area, mainly forestry and agricultural, still require a considerable number of GPS control points to obtain a reliable subsidence offset. In this regard, a minimum of 200 points are required. The combination of both systems allows to obtain of highly reliable information on the X, Y and Z surface displacements (Bahuguna et al., 1991), the accuracy of this technology has been widely demonstrated (Bürgmann et al., 2000; Bitelli et al., 2015; Rateb & Abotalib, 2020). The combination of both technologies has allowed the development of a displacement surface for each period. The analysis is initially performed individually, defining how subsidence evolves over annual and biennial measurements. The analysis is done by biennial periods from 2008 to 2016, while annual periods are used from 2016 onwards.

3.1.2 Targeted area

The case study area is defined by the fully exploited zones from 2008 to 2018, based on the subsidence data collected. The initial year, 2008, is determined as it is the first year in which surface subsidence data are obtained. The final year, 2018, is determined according to (Sanmiquel et al., 2018), where it is stated that 90% of the surface subsidence for an active potash mine occurs within the initial 5 years. Figure 3.2 shows the targeted area in the enclosed orange perimeter and the mining drifts excavated during the years 2008-2018 are marked in light green. The light blue perimeter delimits the area exploited before 2008.

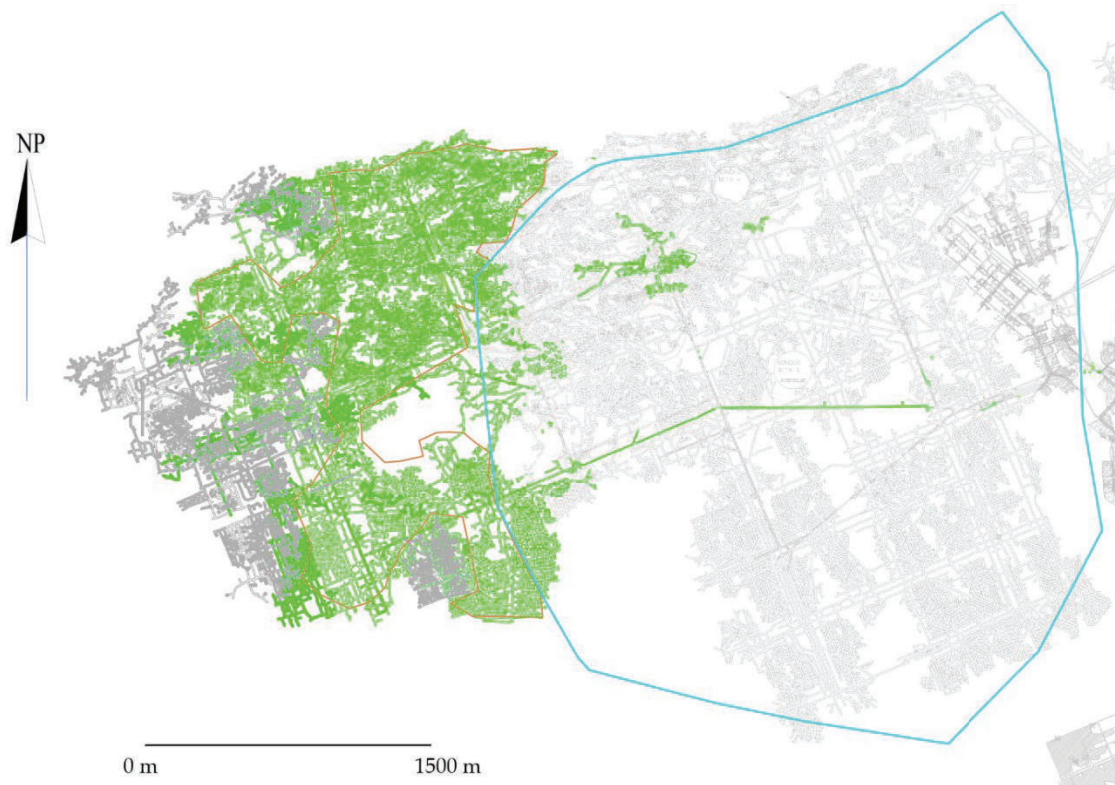


Figure 3.2 The mining area, with the two different perimeters.

3.1.3 Subsidence average profile

The average subsidence profile could be developed based on the displacement surfaces done using GPS and InSAR technology. Five profiles are defined within the area of interest in each of the displacement surfaces. Each profile crosses the area completely, every 10 meters in the direction of the mine advance, East-West, a Metric Point (MP) is listed. These MPs show the displacement in the Z coordinates for each subsidence calculation period. According to Sanmiquel et al. (2018), a 400-meter protection area is determined in order to separate the targeted area from the area exploited before 2008, as no data is available (Figure 3.3). After analyzing all the raw data collected, the MP points are reduced and re-listed every 100 meters, since it is considered an adequate distance to appreciate the evolution of subsidence. Figure 3.2 shows the targeted area in the enclosed orange perimeter and the mining drifts excavated during the years 2008-2018 are marked in light green. The light blue perimeter delimits the area exploited before 2008. Pink lines depict the 5 profiles used to determine the average subsidence of the targeted area, while dark blue marks the 12 mining zones selected to test the model, as they have been sorted from north to south and east to west, respectively. On the other hand, Figure 3.3 shows the targeted area amplified, therefore, the five profiles and the 12 selected mining zones can be seen in more detail. The analysis is initially done individually, defining how subsidence evolves over annual and biennial measurements. Subsequently, subsidence

values are gathered together to obtain the profile of maximum subsidence for each MP and perform a statistical analysis to determine the average subsidence profile of the targeted area, as well as the level of confidence of the subsidence measured.



Figure 3.3. Mining areas with two different perimeters, the five profiles and the twelve selected zones can be seen.

3.1.4 Numerical model design

The model has been designed based on the stratigraphic column taken from Campos de Orellana (1996) and subsequently modified by Cendón et al. (2003), adding two horizons of Anhydrite and Halite on top of those, known as roof salt. The first lithology consists of sedimentary material such as sandstone, limestone and lutites, and the second group of lithologies consists of two layers of anhydrite. These two groups of stratum correspond to the overburden part of the model. The following layers are defined by the potassic seams, formed by Carnalite, Bed B, Intermediate salt, Bed A and Footwall salt, and finally comes the last lithology formed by the lower salt. Figure 4 is not to scale, the top and bottom have been cut off only showing the middle part of the model, which is considered the representative part of it. The geomechanical values of the lithologies were determined by laboratory and field testing, while some data was taken from (Campos de Orellana, 1996). Table 3.1 shows values of geomechanical properties for each lithology. In order to model the deposit using FEM methodology, the stratigraphic column has been simplified as shown in Figure 3.4. Therefore, the potassic seams have been simplified into 4 lithologies; Upper

salt, Carnallite, Silvite (1 and 2 seams) and Rock salt (Halite), which are the ones considered to have creep properties within them. Consequently, their geomechanical properties have been modified (Table 3.2). An example of the stratigraphic column samples can be seen in Appendix 1.

Table 3.1. Values of geomechanical properties for each lithology.

Lithology	Sedimentary material	Anhydrite material 01	Anhydrite material 02	Upper salt	Potassic layer 01	Potassic layer 02	Footwall salt	Lower salt
Unit weight(kN/m ³)	26.55	29.7	23.5	23.7	19,8	21	21	21
Poisson ratio	0.31	0.3	0.26	0.29	0.145	0.215	0.2	0.2
Young Modulus (kPa)	3.57·10 ⁰⁷	4·10 ⁰⁷	3.09·10 ⁰⁶	5.3·10 ⁰⁶	5.19·10 ⁰⁶	2.19·10 ⁰⁶	1.38·10 ⁰⁶	1.38·10 ⁰⁶
Tensile Strength (kPa)	4850	6040	2680	3900	2330	2650	2500	2500
Friction angle (degrees)	34	33	30	35	36	45	45	35
Cohesion (kPa)	6970	13600	9755	3800	2100	3277.5	2900	2900

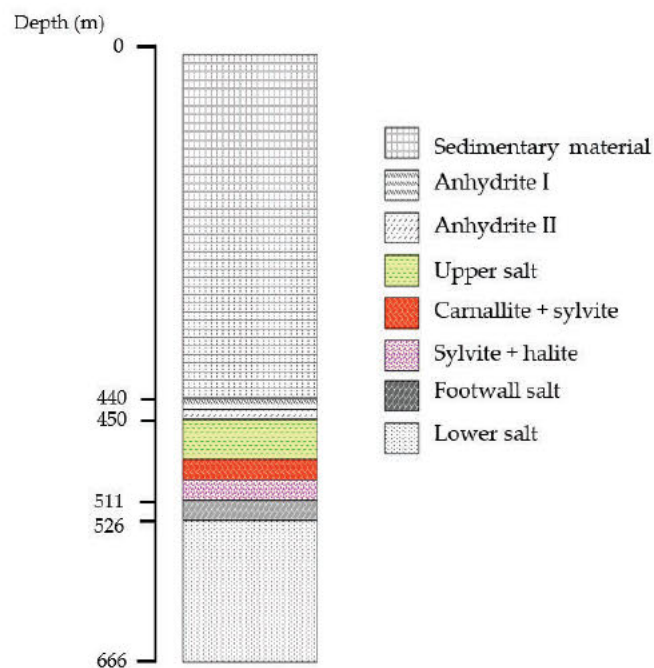


Figure 3.4 The stratigraphic column used for the RS2 model.

Table 3.2. Geomechanical properties of the potassic group used in the RS2 models.

Properties	Materials			
	Carnallite + Potash layer 01	Intermediate salt + Potassic layer 02	Upper salt	Footwall salt (Rock salt)
Unit Weight (KN/m ³)	19,8	21	21	21
Poisson ratio	0,145	0,215	0,38	0,2

Young modulus (Kpa)	5,19E+06	2,19E+06	5,30E+06	1,38E+06
Tensile strength (Kpa)	2330	2650	2780	2500
Friction angle (°)	36	45	45	45
Cohesion (Kpa)	2100	3277,5	5910	2900

3.1.4.1 Design of the mining drifts

The tunnels have been defined using the "Tunnel Wizard" option. Therefore, the basic geometry of the "shoulder cavern" type tunnel has been modified using the dimensions of the real mine planning (Figure 3.5). The height has been unified to 6 meters for all sections, the width of drifts has been taken from the real mine map and the crown and shoulder radius have been approximated for each case, using the above-mentioned parameters (base values of the "shoulder cavern", height and width for each drift).

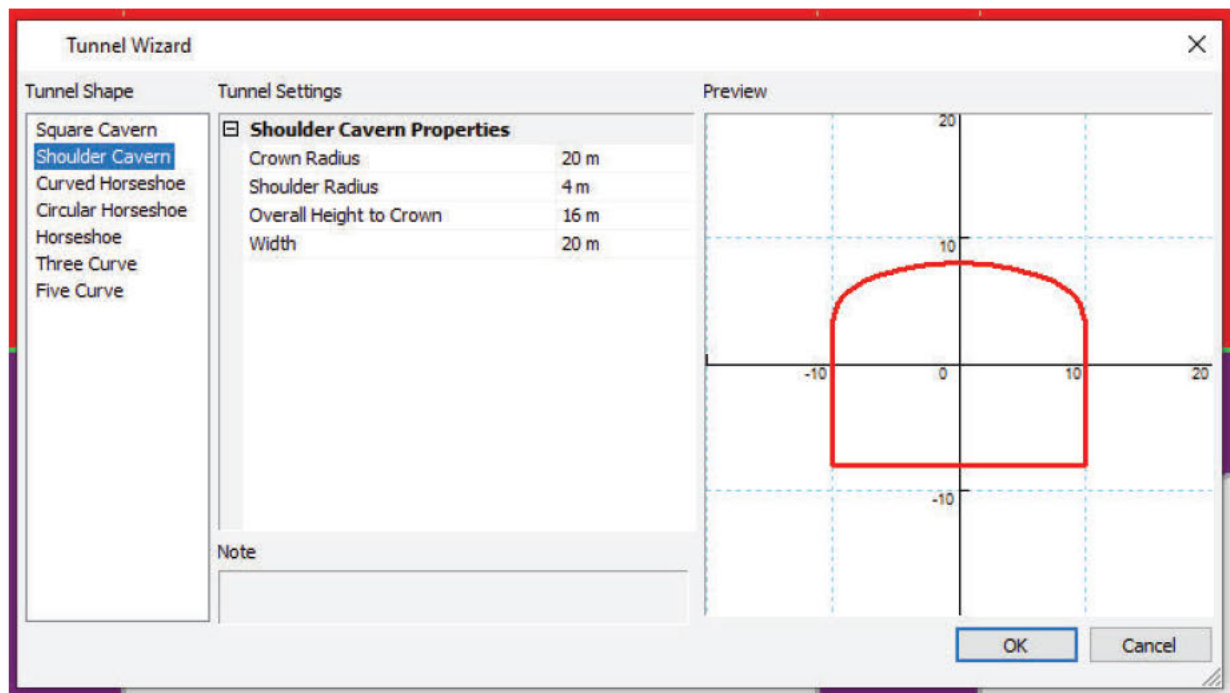


Figure 3.5 Tunnel wizard tool (RS2 software).

3.1.4.2 Numerical model definition

The numerical model has been generated using indirect time-dependent behavior modelling, using the RS2 v11.003 software. After analyzing the geometries of the drifts and the extraction ratio, an initial model has been run. The total size of the model is 225 meters by 666 meters, with a minimum of 37.5 meters of walls on each side and, therefore, 150 meters of exploitation are modelled. The model size is based on the stratigraphic column size proposed by

Campos de Orellana (1996). Several studies have been used in order to define the wall width (Xu et al., 2013; Parmar et al., 2019). The mesh consists of 6 nodal triangles, while it is graded and densified around 150 meters of the mined area, as well as in the areas of lithological variations to adequately capture displacements adjacent to the drift wall. No support material has been placed in the drifts. The Mohr-Coulomb constitutive model has been adopted for the analysis. RS2 model is presented in Figure 3.6, where all the materials can be seen.

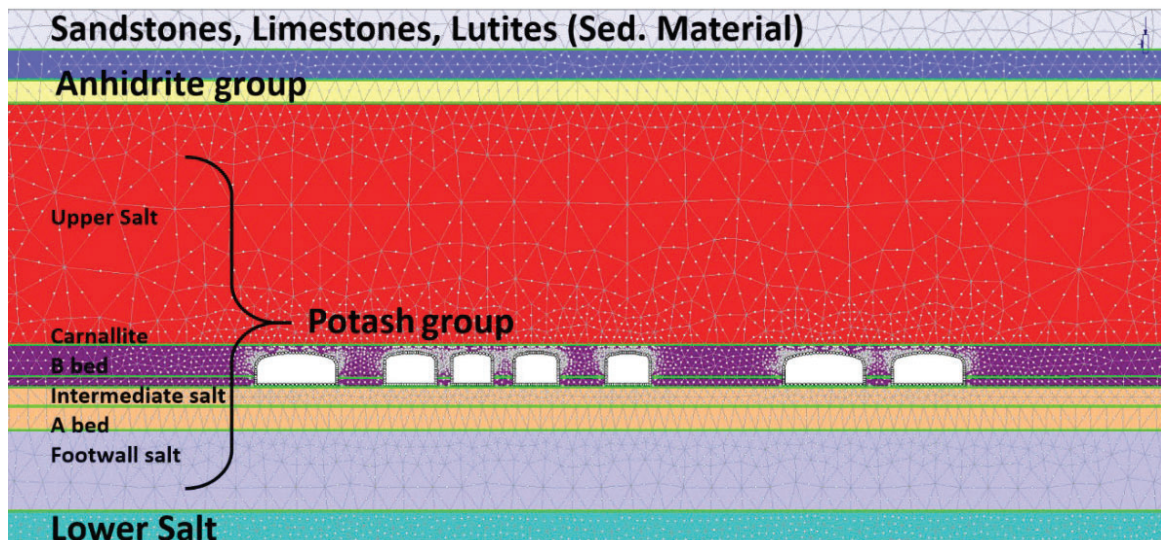


Figure 3.6. Example of an RS2 model with the geological and drifts characteristics.

3.1.4.3 Young's modulus decreasing methodology

The materials with time-dependent behavior are the following lithologies: Carnallite, bed B, Intermediate salt, bed A and footwall salt. Seven stages have been defined, each one representing two years. As can be seen in Figure 6, in the first stage, the original properties of the geological materials have been used, while Young's modulus of the materials with time-dependent behavior has been reduced from the second stage onwards. Figure 3.7 illustrates the methodology to define Young's modulus decrease. The first modulus reduction was defined according to Paraskevopoulou et al. (2012), while the following reductions are determined by an iterative approach (Figure 3.6), comparing the actual subsidence data and RS2 values.

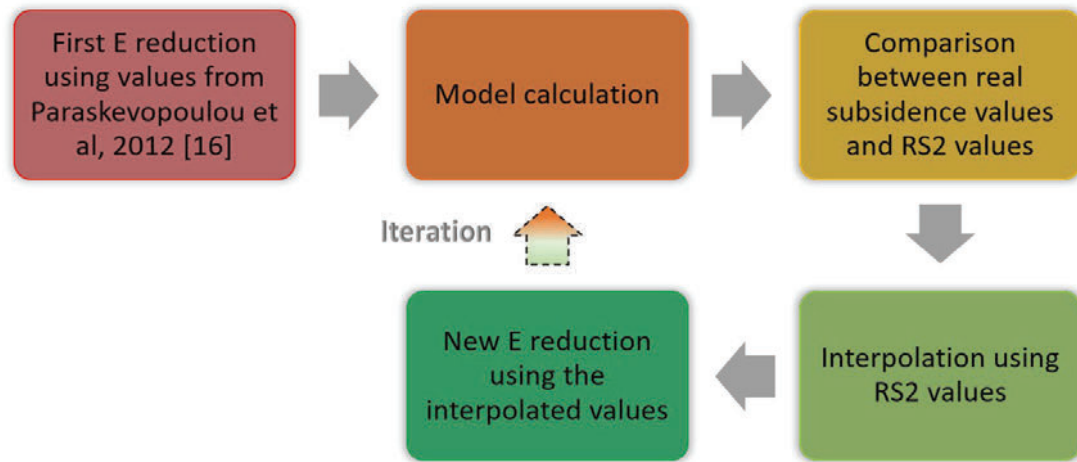


Figure 3.7. The methodology followed to define Young’s modulus decrease.

The factor used in each stage to reduce modulus is included in Figure 3.8, weakening the material properties of the model as a time-dependent behavior. The determination of geomechanical characteristics of each stage is verified using the surface subsidence values. Once all the steps of the initial model were verified, it was tested in 12 selected mining zones, all of them included in the target area. The selection of these zones was done randomly in order to achieve more representativity of the procedure proposed and its usage.

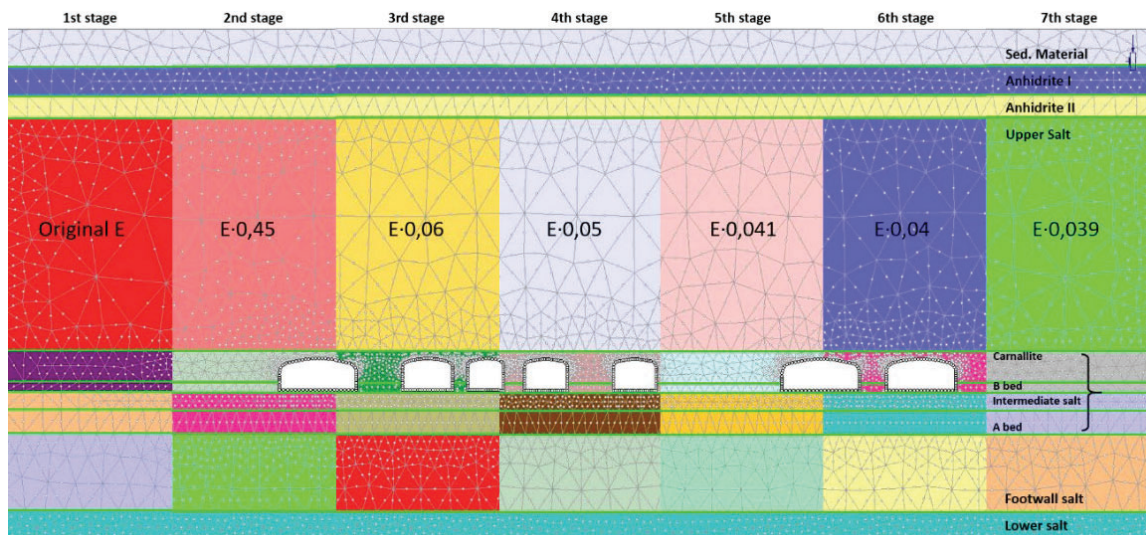


Figure 3.8 Example of the seven stages and their associated Young’s modulus (E).

The decrease of the Young modulus is characterized by being in the first three stages very pronounced and more reduced in the following four stages (Figure 3.9). The first three stages correspond to the first 6 years, according to Sanmiquel et al. (2018), while the first 5-year period is where 90% of the subsidence is

concentrated. On the contrary, in the later periods, the subsidence process is more stable, entering what is known as the residual subsidence period.

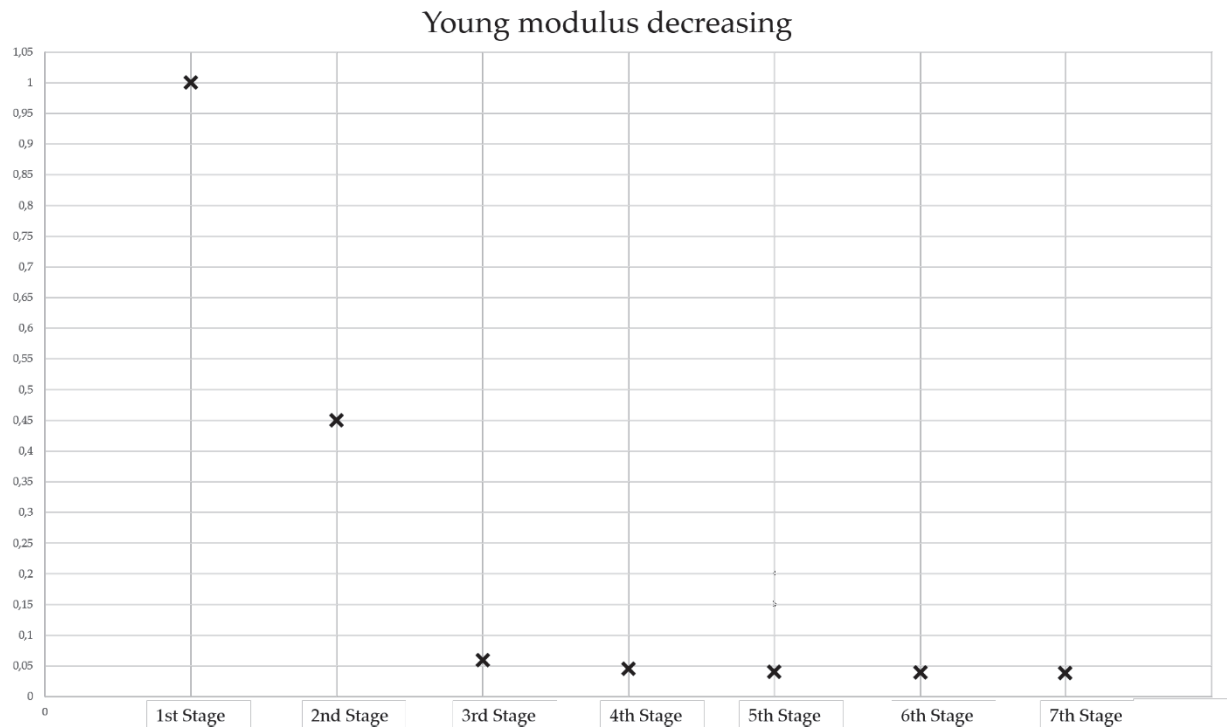


Figure 3.9 Young modulus decrease.

3.2. Definition of characteristic subsidence parameters. A case study in the Catalan Potash Basin

The following three sections will provide a description of the methodology used. Firstly, the creation of the database was done based on GNSS and InSAR techniques. Following this, a specific methodology was designed based on CAD software, coupled with the aforementioned techniques. The definition of nine sections allowed the study of 74 subsidence profiles, which provided an accurate analysis of the selected area. Finally, a methodology was successfully developed to approximate the subsidence basin profile by a Gaussian distribution using the least squares method.

3.2.1 Database creation

An analysis was carried out to identify the typical values defining the surface of a subsidence basin, the angles and the governing function. The model has been developed based on the classical equations that define the parameters for surface subsidence (National Coal Board, 1975). For this purpose, the topographic characteristics of the terrain were considered by means of measurements carried out over nonconsecutive twelve years in the period from 1995 to 2021. In Table 3.3, a correlation between periods and methodologies employed is shown. The

case study has been monitored over an area of 46 km² using GNSS and InSAR technology. The set of GNSS control points has been used to cover the whole area affected by the subsidence process, additionally, InSAR imagery has also been used to complement the monitoring system. Although there are some urban areas, the target area is dominated by forest and agricultural land. GNSS and InSAR methods were employed due to their reliability and accuracy in mining subsidence research (Amelung et al., 1999; Diao et al., 2019; Modeste et al., 2021). Only in the first periods, 1995 to 2003 and 2003 to 2008, the measurement campaigns were developed by the mining company, and the methodology used was classic total station topography. 2008 the data was transferred to the research group, and a new methodology was established using GNSS.

The GNSS method used is based on static differential GPS with dual frequency receivers, using 4 devices. This way, two of them are considered as bases, placing them in two well-identified coordinate points. The other two devices are used to measure the control points. The minimum measurement time for each control point is 12 minutes. Thus, for each point, it was possible to obtain the coordinates in the three axes, X, Y, and Z with a maximum error of two centimeters, taking into account that the methodology used has an accuracy of one centimeter in planimetric and altimetric coordinates. In addition, a double quality control has been performed with the following steps: Firstly, during the GPS post-process, using the Magnet Tools software, a warning is set off when an error higher than two cm is detected. Secondly, when the error is detected, the point is remeasured two times within a one-week gap.

InSAR technology was introduced in the subsidence control method in 2016, being a well-established and reliable approach at that time (Sanmiquel et al., 2018). The given approach used an average number of 176 InSAR images from the SENTINEL-1 satellite coupled with an average number of 241 GNSS points; details are shown in Table 01. Displacement surfaces for the whole period are available as a result of deploying the combined methodologies (Sanmiquel et al., 2018).

Table 3.3 Correlation between periods and methodologies used.

Initial year	End year	Methodology of measurements
1995	2003	Surveying by total station. Measurement with an average of 600 control points.
2003	2008	
2008	2010	Surveying by GNSS. Measurement with an average of 1000 points.
2010	2012	
2012	2014	
2014	2016	
2016	2017	Surveying by GNSS and InSAR technology. Measurement of 246 GNSS control points combined with 201 images from SENTINEL-1

2017	2018	Surveying by GNSS and InSAR technology. Measurement of 305 GNSS control points combined with 142 images from SENTINEL-1.
2018	2019	Surveying by GNSS and InSAR technology. Measurement of 282 GNSS control points combined with 142 images from SENTINEL-1.
2019	2020	Surveying by GNSS and InSAR technology. Measurement of 147 GNSS control points combined with 175 images from SENTINEL-1.
2020	2021	Surveying by GNSS and InSAR technology. Measurement of 224 GNSS control points combined with 220 images from SENTINEL-1.

3.2.2 Database management

To analyze the displacement surfaces, AutoCAD and TCP-MDT software have been used. Nine sections were selected in the area affected by subsidence (Figure 2); four of them cross the target area from East to South West, identified with numbers (1 to 4), while 5 vertical sections from North to South (A to E). A Metric Point (MP) is considered every 10 meters in all sections of the twelve periods, showing the displacement in the Z-coordinate. The calculation periods used to determine each subsidence base are accumulative, using an interval of more than five years, which corresponds to 90% of the subsidence that can be formed in the case study (Sanmiquel et al., 2018) and, therefore, it may be possible to detect a well-formed subsidence base in all of them and see how progresses. According to nine sections and the displacement surface for each indicated period, a total number of 74 subsidence basin profiles were analyzed.

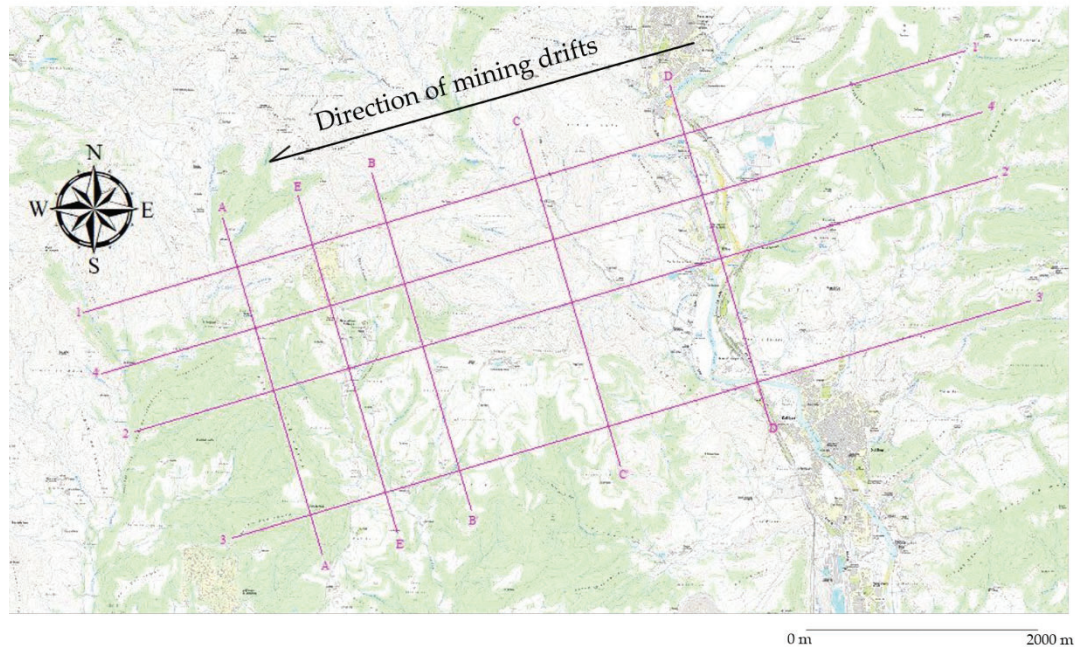


Figure 3.10. The nine sections are located in the case study area, in pink.

The proposed methodology allows to calculate of the distance of influence by establishing the start and end parts of each subsidence profile and the total depth for each subsidence profile. In Figure 3.11, accumulative subsidence basins profiles of section 01 are shown, each color indicates a different period in order to observe its evolution over time, it can be noticed that the subsidence profile becomes better defined as the time period increases, since with time mining infrastructure increases. Mining subsidence is a phenomenon that is closely related to the mining excavation ratio, among other geological and mining parameters (Hunt, 1980; Salmi et al., 2017; Sasaoka et al., 2015; Diao et al., 2019). Points in red indicate points of zero subsidence (start and end point of subsidence basin). Taking these points and the mining map into account from 1995 to 2021, it was possible to determine the distance of influence, which is the shortest distance between the point of zero subsidence and the nearest mining drift allowing the determination of the distance of influence for all subsidence profiles. However, to calculate the total depth from the surface to the drift, it was necessary to check the cartographic maps available from the Cartographic and Geological Institute of Catalonia (ICGC) since the depths indicated on the mining map are referenced to sea level.

The boundary angle is defined by the zero-subsidence point and the total depth of the mining drifts. Considering this definition, it can be calculated following the mathematic relationship stated by the National Coal Board (1975), as shown in Figure 3.12. The determination of the characteristic boundary angle for the area of interest was carried out through statistical calculation. Finally, Figure 3.13 shows the process of the methodology used up to the reaching point of the

characteristic boundary angle and distance of influence.

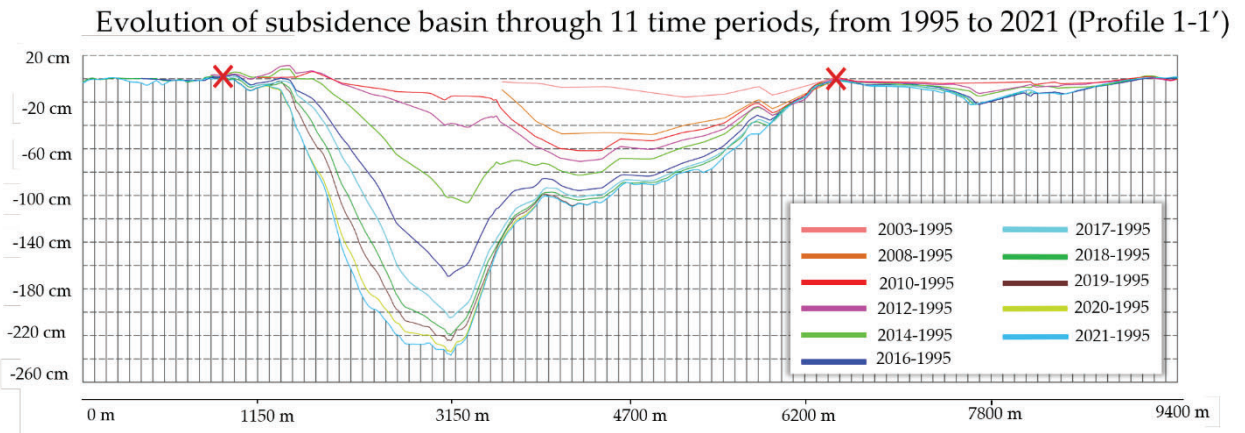


Figure 3.11. Example of 11 subsidence basins from 2003 to 2021.

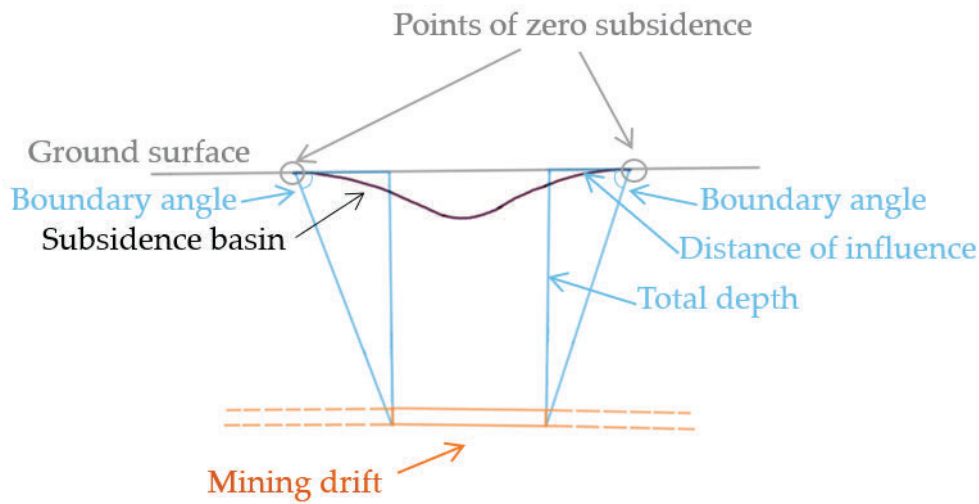


Figure 3.12. Mathematic relationship scheme.

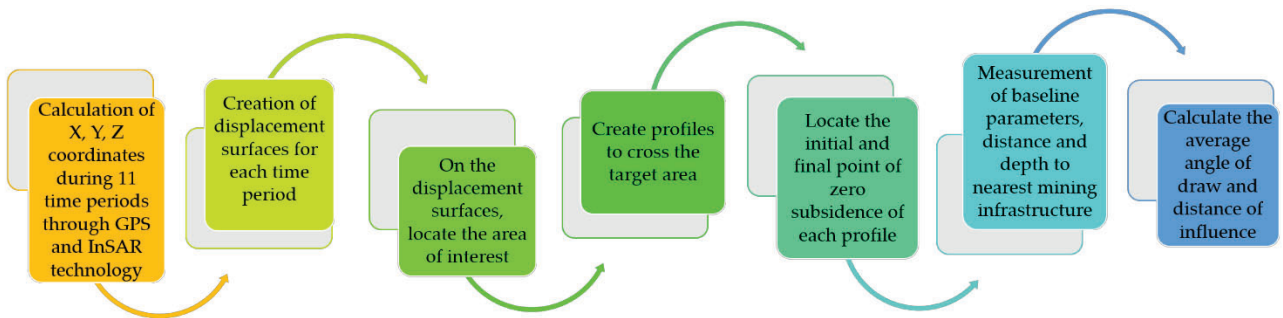


Figure 3.13. The methodology proposed to calculate the limit boundary angle and distance of influence.

3.2.3 Characteristic function of the subsidence basin

The effect of underground mining drifts on the surface topography is inevitably associated with the resulting ground movements in a subsidence basin. A considerable amount of data is available from field measurements of surface settlement profiles on tunnels in clays. Figure 3.14 has been used to summarize

the settlement trough adopted from several research, where the surface vertical settlements and horizontal stress and displacement are shown (Schmidt, 1969; Peck, 1969; National Coal Board, 1975; Clough and Schmidt, 1981; O'Reilly and New, 1982; Rankin, 1988; Peng, 1992). The green field settlement profile, which can represent the profile of a subsidence basin over a single tunnel, can generally be approximated by the error function or normal probability curve (also known as Gaussian curve) as follows (Equation 3.1):

$$S_v(x) = S_{vmax} \exp\left(\frac{-x^2}{2 i_x^2}\right) \quad \text{Equation 3.1}$$

where S_{vmax} is the maximum surface subsidence at the centre line of the tunnel or drift, S_v is the surface subsidence at displacement distance x from the tunnel centre line, x is the horizontal distance from the center line, i_x is the horizontal distance from the center line to the inflexion point in the subsidence basin.

Alternatively, O'Reilly and New (1982), based on monitoring data from several tunnels in the UK, were able to prove that the horizontal surface displacements occur in the transverse direction of the excavation axis and, assuming that, the resulting displacement vector is oriented towards the tunnel, the horizontal movement can be expressed as follows (equation 3.2).

$$S_{hx} = \frac{x S_v(x)}{z_0} \quad \text{Equation 3.2}$$

Where z_0 depth of the tunnel or drift center line, S_{hx} is the horizontal movement at displacement distance x from the tunnel center line.

The horizontal displacement corresponds to the inflexion point of the subsidence basin. The horizontal deformation can be calculated by deriving the aforementioned expression (equation 3.3).

$$\varepsilon_{hx}(x) = \frac{S_v(x)}{z_0} \left(\frac{x^2}{i_x^2} - 1 \right) \quad \text{Equation 3.3}$$

Where the I parameter is the inflexion point of the subsidence basin, ε_{hx} is the strain or horizontal deformation, and S_v is the surface subsidence at offset distance x from the tunnel center line.

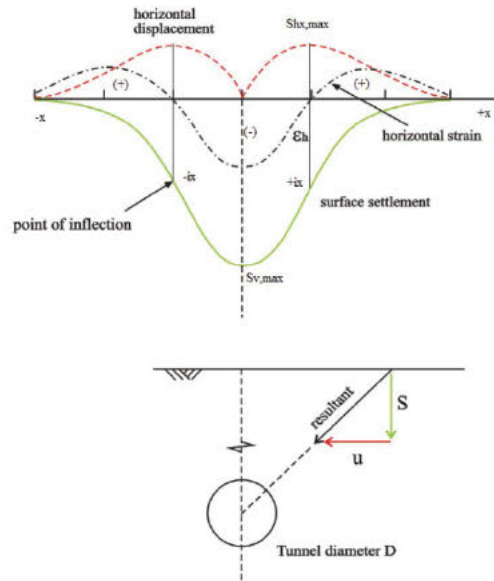


Figure 3.14. Distribution of horizontal strain, surface displacements, boundary angle and surface vertical settlements trough (O'Reilly, M.P. & New, 1982).

In subsidence engineering, the terminology “deformation or strain (ϵ)” is the change in length over a piece of ground, expressed either as a dimension over the whole length or as a fraction of the unit of length. The direction is always specified with extensions and compressions, indicated by a + and – sign, respectively. Furthermore, the degree to which any surface site may be expected to tilt, as a result of subsidence, is calculated from the subsidence profile. Prediction of deformation from curvature is a useful tool that can be applied to any part of any profile.

The curvature can be calculated by dividing the subsidence difference by the distance between the observed stations (STN), which gives the slope (θ), determining the curvature and horizontal strain. An example can be seen in Figure 3.15.

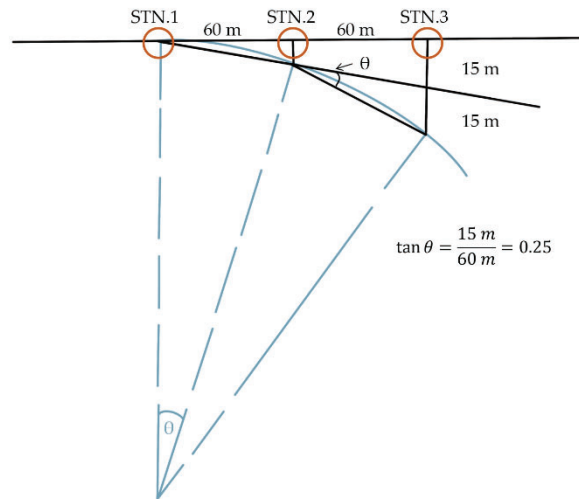
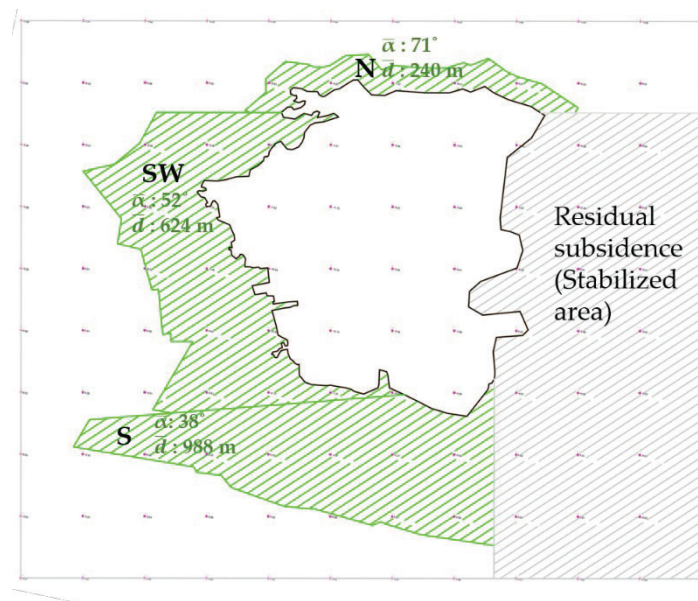


Figure 3.15. Example of strain curvature (Adapted from (National Coal Board, 1975).

3.3 Statistical Model Definition

Considering the area of interest based on the average angle of the draw and the distance of influence for the period 1995-2021 in section 3.2, it was possible to design a final area of interest for testing the statistical model.

The statistical model started with the definition of the geological and mining characteristics that may influence the subsidence process. These characteristics were evaluated at 120 points, these points were determined by designing a 500m x 500m mesh (Figure 3.16), using MDT and AutoCAD software. This mesh was used in all the accumulative subsidence basin surfaces. Therefore, it was possible to define the X, Y, and Z coordinates in 120 points.



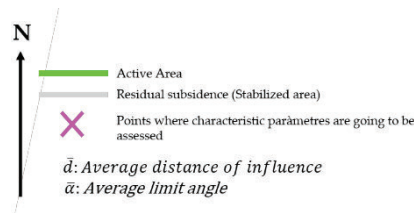


Figure 3.16 Area of interest with 120 points defined

3.3.1 Characteristics of the statistical model

3.3.1.1 Fault

Faults are flat or slightly curved fractures through which significant displacement has occurred as a result of rock mass movements. In several works, faults are considered a geological characteristic that directly influences subsidence processes (Burbey, 2002; Nie et al., 2013). In the subsidence process due to mining infrastructure, some authors consider that mining works can increase the fault influence regarding the subsidence process (Xie et al., 1998; Donnelly, 2009). To know how the fault affects the mining management and design is important to know the type and main characteristics of the fault, such as direction, dip and length. Therefore, analysis points have been defined in the entire area where the fault intersects the mining infrastructure.

3.3.1.2 Topography

The topography of the study area is an essential parameter to consider when assessing, predicting and managing subsidence processes. Therefore, several works use it to evaluate surface subsidence, for instance (Zhou et al., 2022), where a practical prediction model based on the optimization of combined slope-slide parameters is proposed to evaluate landslides and the surface collapses. According to Akcin, (2021), a risk assessment decision matrix based on the geographic information system model (RADM-GIS) was applied to assess the spatial risk of surface subsidence and building damage due to active underground coal mining located in Turkey. The main characteristics to build the model are mining tunnels and production panels, topography, geology and land use of the area. Thus, the area has been divided into zones based on its topography.

3.3.1.3 Overburden

The overburden is the material above an economic mining area, including the rocks, soil and ecosystem above the ore body. It is the part that connects the underground to the surface and, therefore, represents a key parameter to consider in order to properly manage and predict surface subsidence processes (W. Guo et al., 2021), (Lawson et al., 2017).

3.3.1.4 Typology

In a subsidence basin due to underground mining, it is essential to manage its progression. Three types of subsidence can be defined according to the development of mining extraction (Modeste et al., 2021; Wang et al., 2018). It is, therefore, essential to detect where are the areas with an active subsidence process and those with residual subsidence. It is essential to detect between active zones and those with residual subsidence. According to Sanmiquel et al. (2018), 90% of subsidence occurs in the first five years. Thus, it has been possible to differentiate between each point, whether it was within the active area or the residual subsidence basin.

3.3.1.5 Percentage of filling

Mine backfilling is the procedure to fill the cavities created by the underground extraction of minerals. This procedure is widely used to reduce or prevent surface environmental impacts such as surface subsidence, the potential hazard of tailings storage or, in addition, to improve productivity (Van Sambeek, 1992; Zhu et al., 2016). Nowadays, backfilling is being used to improve the productivity of the mining operation in the case studied. However, using the available data, the impact on the evolution of the subsidence process will be evaluated.

3.3.1.6 Extraction ratio

The percentage of mineral extraction in an ore deposit has a direct influence on the movements produced on the surface, such as surface subsidence (Bell et al., 2000). Therefore, it will be considered as a parameter to be evaluated to determine its relationship with the evolution of the subsidence basin year by year.

3.4 Geomechanical and geochemical parameters of saline Lithologies

3.4.1 Sampling

The set of samples consists of a total of 50 units, divided among the 7 lithologies that form the deposit. Appendix 12 shows the locations of each lithological group. The lithologies chosen for the study can be divided into two types; the layers containing potassium, which constitute the main block of economic interest of the mining operation, and the lithologies containing a greater presence of clay discontinuities, since they are the most likely to constitute a risk of falling blocks in the mining infrastructure. At the beginning of the sample analysis, they have been visually inspected and photographed. The visual study consisted of summarizing the physical characteristics of each of the lithologies and inspecting the discontinuities and possible recrystallizations (Appendix 1). Twenty samples

were chosen for analysis. Table 3.3 summarizes the analytical techniques used for each of them.

Table 3.4 Analytical techniques applied to samples.

Cabanasses' samples												
Name	Weight (g)	Clay weight (g)	Analytics									
			Geomechanics						Insoluble particles			
			Humidity	% insoluble particles	Natural density	Granulometry	Uniaxial Compression Strength	Roughness profiles	SEM-EDS	XRD		
"Intermediate Salt (S2)"	S2_01	318,5,3	19,352							x	x	x
	S2_02	2127,7	6,014								x	x
	S2_03	2736,8	7,986								x	x
	S2_04	1914	-	x	x	x					x	x
	S2_05	2378,5	-							x		x
Σ			33,352									
"Upper Salt (ST)"	ST_01*	1526,4	-									
	ST_02	3141,1	11,274							x	x	x
	ST_03	1191,5	7,193									x
	ST_04	3178	29,995	x	x	x				x	x	x
	ST_05	1333,2	-							x	x	x
Σ			48,459									
"A Potash Bed (A)"	CA_01	3549,5	20,6							x	x	x
	CA_02	3274,3		x	x	x					x	
	CA_03	2311,4										
	CA_04	3166,5										
	CA_05	1411,3										

Σ			20,6							
"Transformed Salt (T)"	T_0 1*	117 9,3								
	T_0 2	128 8	13,5						x	x
	T_0 3*	138 2,7								
	T_0 4	188 8,8	4,38 6						x	x
	T_0 5	271 4,2	5,99 5	x	x	x			x	x
Σ			23,8 81							

3.4.2 Geomechanical behavior

All geomechanical and geochemical tests used in the development of this research are detailed in the following sections.

3.4.2.1 Analysis of Discontinuities

The process of analyzing the roughness of the discontinuities in the samples has been done based on the ISRM suggestion (N. R. Barton, 1978), thus, it was needed the traditional tool named Barton's comb shown in (see Figure 3.17). In Figure 3.18 it can be seen an example of a discontinuity surface

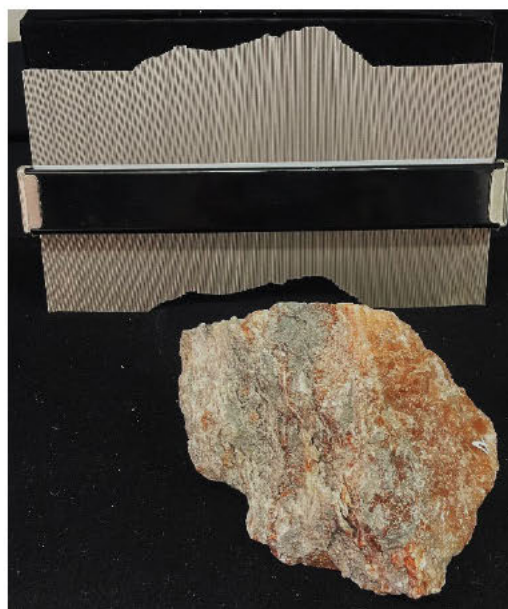


Figure 3.17 Roughness meter or Barton comb together with the saline sample.

In a few cases, it was detected that the sample was altered due to the change of atmosphere, from the underground mine to the surface conditions. Considering

this drawback, each sample has been examined, verifying the surface of discontinuities before assessing it with Barton's comb.



Figure 3.18 Discontinuity surface of a sample from the intermediate salt lithology.

3.4.2.2 Particle-size analysis (PSA) methodology

PSA is a measurement of the size distribution of individual particles in a granular sample such as soil, in this particular case, it spans a large size range, varying from stones and rocks (exceeding 0.25m in size) down to submicron clays (<1 μm). Various systems of size classification have been used to define arbitrary limits and ranges of soil-particle size. Soil particles smaller than 2000 μm are generally divided into three major size groups: sands, silts, and clays. Geologists and geomorphologists typically use the Wentworth classification scheme (Wentworth, 1922), shown in Figure 3.19 (Gee and Or, 2002).

Millimeters (mm)	Micrometers (μm)	Phi (ϕ)	Wentworth size class	Rock type
4096		-12.0	Boulder	Conglomerate/ Breccia
256		-8.0	Cobble	
64		-6.0	Pebble	
4		-2.0	Granule	
2.00		-1.0	Very coarse sand	
1.00		0.0	Coarse sand	Sandstone
1/2	0.50	1.0	Medium sand	
1/4	0.25	2.0	Fine sand	
1/8	0.125	3.0	Very fine sand	
1/16	0.0625	4.0	Coarse silt	
1/32	0.031	5.0	Medium silt	Siltstone
1/64	0.0156	6.0	Fine silt	
1/128	0.0078	7.0	Very fine silt	
1/256	0.0039	8.0	Clay	
0.00006	0.06	14.0		Mud Claystone

Figure 3.19 Udden-Wentworth grain-size classification scheme (Wentworth, 1922).

Particle-size analysis data can be presented and used in several ways, the most common being a cumulative particle-size distribution curve. An example is shown in Fig. 3.19. The percentage of particles less than a given particle size is plotted against the logarithm of the effective particle diameter. Particle-size distribution curves, when differentiated graphically, produce frequency distribution curves for various particle sizes. Frequency curves usually exhibit a peak or peaks representing the most prevalent particle sizes.

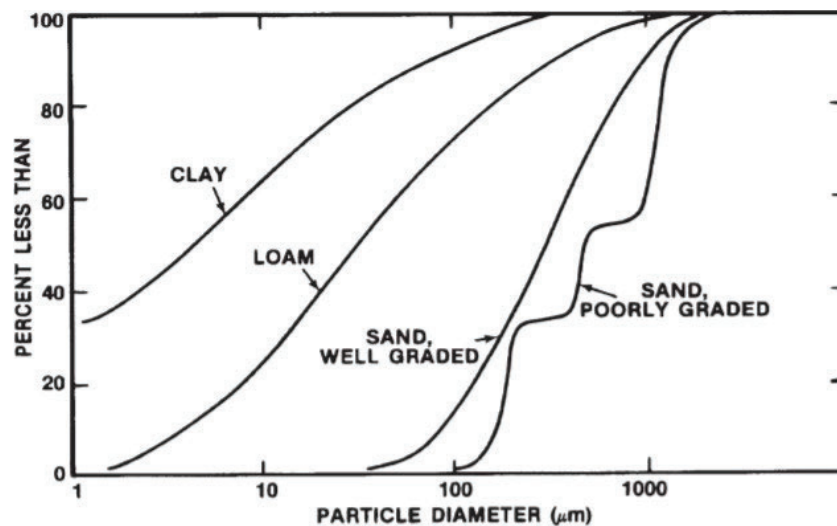


Figure 3.20 Example of different particle size distribution well and poor graded (Hillel, 1982).

In order not to damage the crystalline lattice of the material, the saline material has been crushed with the help of a rubber hammer to develop the granulometric analysis. All samples have a similar weight and they have been shredded during

a similar time and impact since the results of the particle size analytics could be properly compared. Figure 3.20 show an example of crushed material.

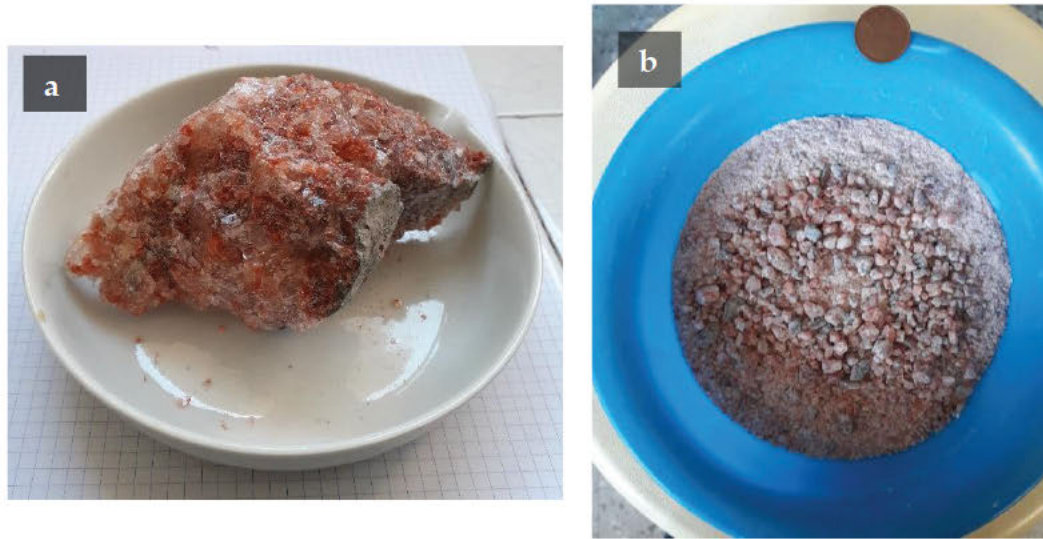


Figure 3.21 Example of original material (a) and after the crushing made with the hammer rubber (b).

Once each sample is crushed and weighed, it is time to pass it through the sieves. All samples are shredded before using the sieve to minimize their alteration. Figure 3.21 shows a part of the column used and an example of a single sieve with the material retained in it.

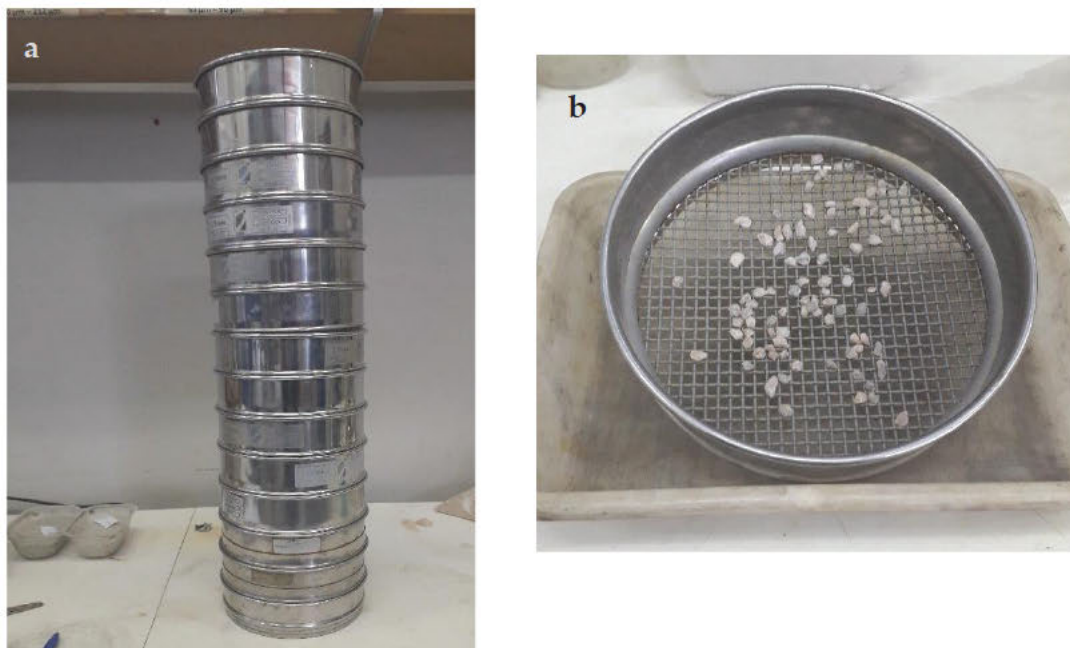


Figure 3.22 a) Sieve column, and b) detail of a single sieve; Where samples were tested.

Particle size distribution is a very useful tool in geotechnical engineering. It is an indicator of other engineering properties such as compressibility, shear strength, and hydraulic conductivity. The samples are analyzed, calculating the uniformity coefficient or Hazen coefficient (C_u) defined by (Hazen, 1892), and the curvature coefficient (C_c) according to (Iglesias, 1997). Both coefficients are calculated as it is shown in equations 3.4 and 3.5. The uniformity coefficient evaluates how uniform a sample is. A sand sample is considered as follows.

If $C_u < 6$ The sample is uniform

$6 < C_u < 20$ The sample is less uniform $C_u > 20$ The sample is heterogeneous

A gravel sample is considered as follows. If $C_u < 4$ The sample is uniform

$4 < C_u < 20$ The sample is less uniform $C_u > 20$ The sample is heterogeneous

Coefficient of uniformity

$$C_u = \frac{D_{60}}{D_{10}} \quad \text{Equation 3.4}$$

D_{60} : Size of the sieve in which 60% of the particles pass through it.

D_{10} : Size of the sieve in which the 10% of the particles pass through it

The particle size distribution can also be characterized by its curvature, or more specifically, by the coefficient of curvature C_c .

Coefficient of curvature

$$C_c = \frac{D_{30}^2}{(D_{60} \cdot D_{10})} \quad \text{Equation 3.5}$$

D_{30} : Size of the sieve in which 30% of the particles pass through it

If $1 < C_c < 3$ Sample well-graded

3.4.2.3 Determination of natural density methodology

Due to the inconveniences of the dissolution of the samples, it is used the hydrostatic balance method to obtain the estimated value of natural density. The performance of this test is regulated by the UNE 103.301-94 standard. According to the UNE standard, the density of soil is determined as the ratio between the mass and the volume of the soil. To perform the test, the sample must have the just content of humidity and tiny particles to allow paraffin coating. To develop this test, 4 samples from Cabanasses were used, each sample from a different salt lithology; intermediate Salt, Upper Salt, A potash bed and Transformed salt. All samples are irregular; therefore, their volume is unknown.

All samples were then weighed on a balance with an accuracy of 0,001gr (W_1). And they were waxed with a very thick layer of paraffin type P.F. (56-58°C) in lentils, used in laboratories PANREAC QUIMICA, S.A, previously melted (Figure 3.22). In Appendix 2, it is attached the Paraffin technical datasheet.

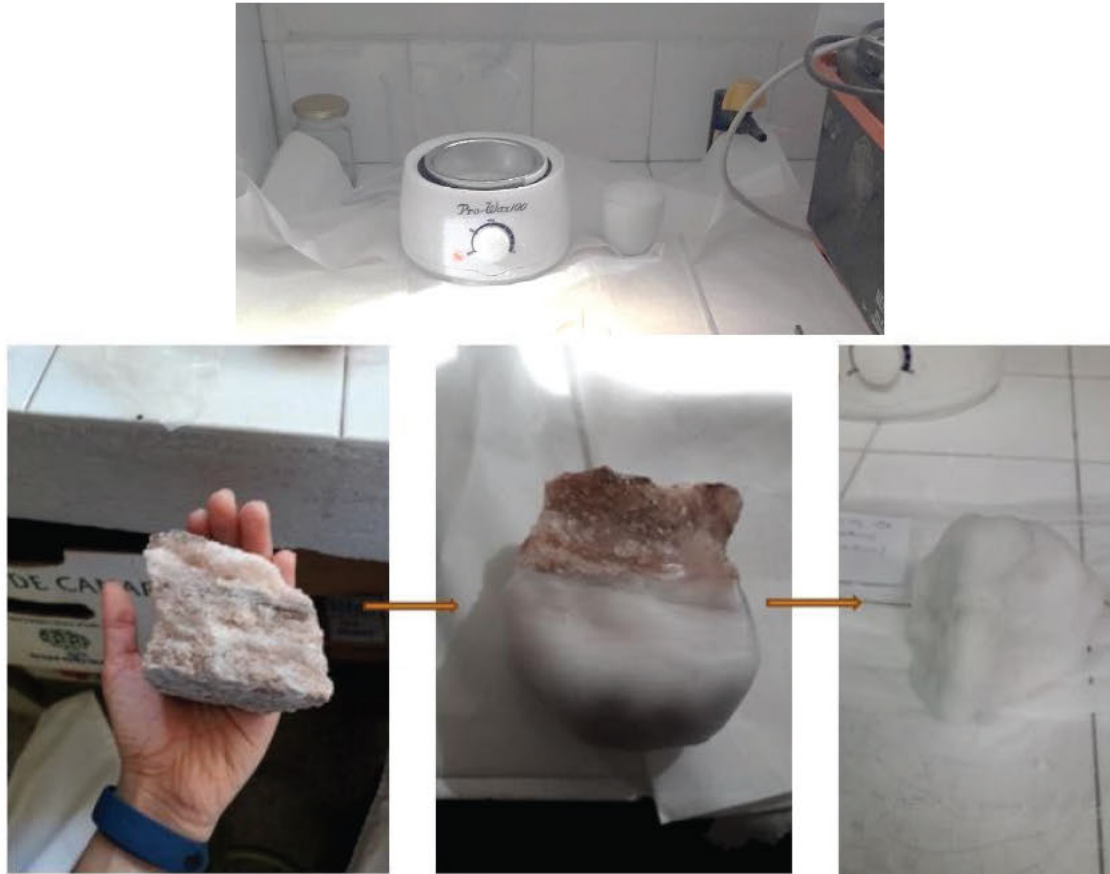


Figure 3.23 Process of waxed.

Once the samples were paraffinized, they were weighed again, finding (W_2), with the precision of 0.001gr and immersed in distilled water using a hanging basket so that it does not touch the bottom of the full container of water (Figure 3.23). The balance determines the weight of the submerged sample (W_{sum}).

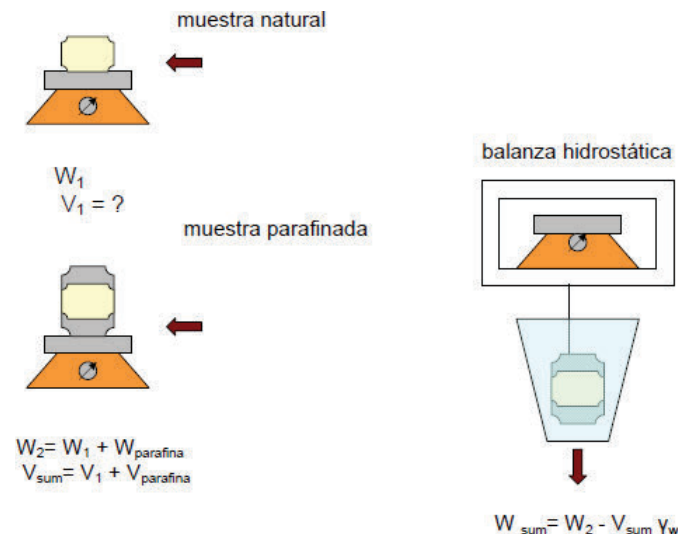


Figure 3.24 Scheme of natural density test, from (Yubero, 2008).

The following is shown in Figure 3.24 The hydrostatic bascule was built using laboratory material; a bascule with a precision of 0.001gr, a stick of glass, 2 meters of wire, adhesive tape, a hanging basket, a container, and 15 litres of distilled water.



Figure 3.25 Hydrostatic bascule built with the laboratory material.

Subsequently, the difference between the values of W_2 and W_1 will correspond to the mass of the paraffin added on the surface of the sample, W_{paraffin} . Its volume, V_{paraffin} , in cm^3 , is given by the quotient between the W_{paraffin} mass and paraffin density in g/cm^3 .

$$W_{\text{Paraffine}} = w_2 - w_1 \cdot V_{\text{Paraffine}} = \frac{W_{\text{Paraffine}}}{\gamma_{\text{Paraffine}}} \left(\frac{\text{g}}{\text{cm}^3} \right) \quad \text{Equation 3.6}$$

The submerged mass of the paraffined sample is determined on a hydrostatic balance, W_{sum} , in gr, with the precision required in balances (0.001 gr). The volume of the sample, V_{sum} , in cm^3 , will be given by the expression (Equation 3.7, 3.8):

$$V_{SUB} = W_1 - W_{SUB} - V_{Paraffine}(cm^3) \tag{Equation 3.7}$$

$$V_1 = V_{SUB} - V_{Paraffine} = \frac{W_2 - W_{SUB}}{\gamma_w} - \frac{W_2 - W_1}{\gamma_{Paraffine}}(cm^3) \tag{Equation 3.8}$$

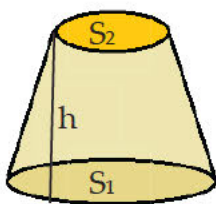
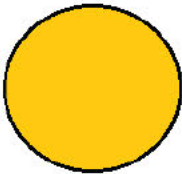
Finally, the natural density γ_n expressed in gr / cm^3 is determined by the quotient (Equation 3.9):

$$\gamma_n = \frac{W_1}{V_1} \left(\frac{g}{cm^3} \right) \tag{Equation 3.9}$$

3.4.2.3.1 Density of Paraffine

The estimated value of paraffine is 0.89 g/ cm^3 , which was obtained in two different ways. On the one hand, its volume was obtained from a known volume and, on the other hand, it was obtained from an irregular volume. In the first case, Table 3.4 and Equations 3.10 and 3.11 show the parameters for calculating the volume of the kerosene.

Table 3.4. Calculation of paraffin density

	
<p>Volume of a Cone Frustum: $\frac{h}{3} \cdot (S_1 + S_2 + (S_1 + S_2)^{1/2})$ h:2,58</p>	<p>Area of a Circle: $2 \cdot \pi \cdot \text{radius}$</p>
	<p>$S_1: 2601/400 \cdot \pi \approx 20,428cm^2$ $r_1: 2,55cm$</p>
	<p>$S_2: 2209/400 \cdot \pi \approx 17,349cm^2$ $r_2: 2.35cm$</p>

Volume of a Paraffine Cone

$$\text{Frustum} \approx 122,766 \text{ cm}^3$$

$$V_{PCF} = \frac{h}{3} (B_1 + B_2 + \sqrt{B_1 B_2}) \quad \text{Equation 3.10}$$

$$\gamma_{paraffine} = \frac{m_{paraffine(g)}}{V_{paraffine(cm^3)}} = \frac{108,878}{122.766} = \frac{0,8868g}{cm^3} \quad \text{Equation 3.11}$$

The second way to calculate the density of the paraffine is using an irregular volume of paraffine which is introduced in a tank full of water, therefore the volume of its solid will be the same as the volume of water left over the tank (Eq. 3.12). To submerge the paraffin solid, a weight since the paraffin does not submerge needed to remain on the surface of the water.

V₁: Volume of the irregular paraffin solid with a weight of 133cm³

V₂: Volume weight= 12cm³

V_p: V₁-V₂= 121cm³

$$\gamma_{paraffine} = \frac{m_{paraffine(g)}}{V_{paraffine(cm^3)}} = \frac{108,878}{121} = \frac{4949}{5500} \approx \frac{0,8998g}{cm^3} \quad \text{Equation 3.12}$$

Finally, the average of the two values is: 0,8933g/cm³

3.4.2.4 Humidity Methodology test

Humidity ω (Equation 3.13) is defined as the ratio of the pore water weight to the weight of solid grains, for a unit volume. Its value is expressed in% and can reach values greater than 100%.

$$\omega = \frac{W_w}{W_{brine}} \cdot 100\% \quad \text{Equation 3.13}$$

It is impossible to determine the humidity due to its saline and the water that fills the pores is brine (Water with a high content of salt). For this reason, two definitions of humidity are distinguished: Classical humidity, ω_w (weight of pure water/weight of solid particles) and brine humidity, ω_{brine} (weight of brine/weight of Solid particles). The weight of the solid particles does not include the weight of dissolved salts that precipitate when the sample dries.

Two weights are considered in determining humidity; first the total weight of the wet sample (W_{wet}), equation 3.14. Secondly the weight of the sample after drying in the oven at 110 °C for 24 hours (W_{dried}), equation 3.15. From these two weights and the dissolved salts concentration, [c] in grams of salt/grams of water, both humidity can be calculated as:

$$\omega_{\omega} = \frac{W_{Wet} - W_{dried}}{W_{dried} (1 + c) - c \cdot W_T} \quad \text{Equation 3.14}$$

$$\omega_{brine} = \frac{(W_{Wet} - W_{dried})(1 + c)}{W_{dried} (1 + c) - c \cdot W_{Wet}} \quad \text{Equation 3.15}$$

$$= \omega_{\omega} (1 + c)$$

3.4.2.4.1 Determination of Concentration

According to Olivella et al. (1996), the empirical formulas that relate concentration to temperature were used to evaluate the concentration of the samples (Equations 3.16, 3.17). This concentration also indicates the degree of solubility of the sample:

$$c = \frac{35,335 - 0,22947T}{1 - 0,0069059T}; \quad T(^{\circ}\text{C}) \quad \text{Equation 3.}$$

$$w_l^h = \frac{c}{100 + c} \quad \text{Equation 3.17}$$

According to the laboratory conditions, the concentration can be calculated as follows (Equations 3.18, 3.19).

$$c = \frac{35,335 - 0,22947T}{1 - 0,0069059T} = \frac{35,335 - 0,22947 \cdot 26}{1 - 0,0069059 \cdot 26} \quad \text{Equation 3.18}$$

$$= 35,8144$$

$$w_l^h = \frac{c}{100 + c} = \frac{35,8144}{100 + 35,8144} = 0,2637 \quad \text{Equation 3.19}$$

Table 3.5 has been made, according to the equations of concentration, which provides the concentrations of maximum saturation or solubility corresponding to pure NaCl at different temperatures:

Table 3.5 Maximum saturation or solubility corresponding to pure NaCl at different temperatures.

T($^{\circ}\text{C}$)	c	w_l^h
20	35,6726	0,2629
21	35,6924	0,2630
22	35,7124	0,2631
23	35,7328	0,2633
24	35,7536	0,2634
25	35,7747	0,2635
26	35,7961	0,2636
27	35,8179	0,2637

28	35,8401	0,2638
29	35,8626	0,2640
30	35,8856	0,2641

Considering the extraction of the samples was developed in summer, the temperatures of the laboratory where the samples were kept ranged above 23°C, almost reaching 26°C. The maximum saturation concentration at 23°C is 35.7328gr and at 26°C is 35.7961. The values for the temperature range from 20°C to 30°C have also been calculated. Therefore, the solubility varies from 35.6726 g of salt dissolved in water to 35.8856, although the difference is greater, it does not represent a substantial change. It represents a reference for the value of both concentration and the value of the fraction of g of Salt / in g of the total mass. Figure 3.25 shows the heater and the temperature used to do the humidity test.



Figure 3.26 Heater used (geology laboratory, EPSEM).

3.4.2.5 Determination of dry density test methodology

When it has been obtained the value of the saline concentration, it will allow obtaining other values such as dry density (γ_d), equation 3.20. The dry density is the dry matter included in a unit of volume in its natural state, that is, the weight that remains of this sample after the loss of all its interstitial water.

$$\gamma_d = \frac{W_s}{V} \quad \text{Equation 3.20}$$

But it can also be calculated with the humidity and natural specific weight, as follow, in equation 3.21:

$$\gamma_d = \frac{\gamma_n}{1 + \omega_{brine}} \quad \text{Equation 3.21}$$

3.4.2.6 Determination of insoluble particles percentage

To determine the percentage of insoluble within the saline material, it is necessary to take a sample with a representative insoluble material for each lithology. The first step is to mill manually the sample reaching a granulometry of about 1 mm and weigh it in a precision bascule (0,001g). Then the samples will be dissolved in 5 litres of distilled water and mixed for approximately 3 hours until the solution is obtained as much homogeneous as possible. Then every mixture needs to rest for 24 hours, covered, in order not to produce evaporation. Following, with the help of a vacuum pump (Figure 3.26), all the mixture is filtered. The last part to filter is the mud trying to make easier the filtering stage. The set of filters used for each sample is dried together with the held material in them, once they are dried they are weighted, taking into account the weight of the filters, and the percentage of insoluble particles can be calculated.

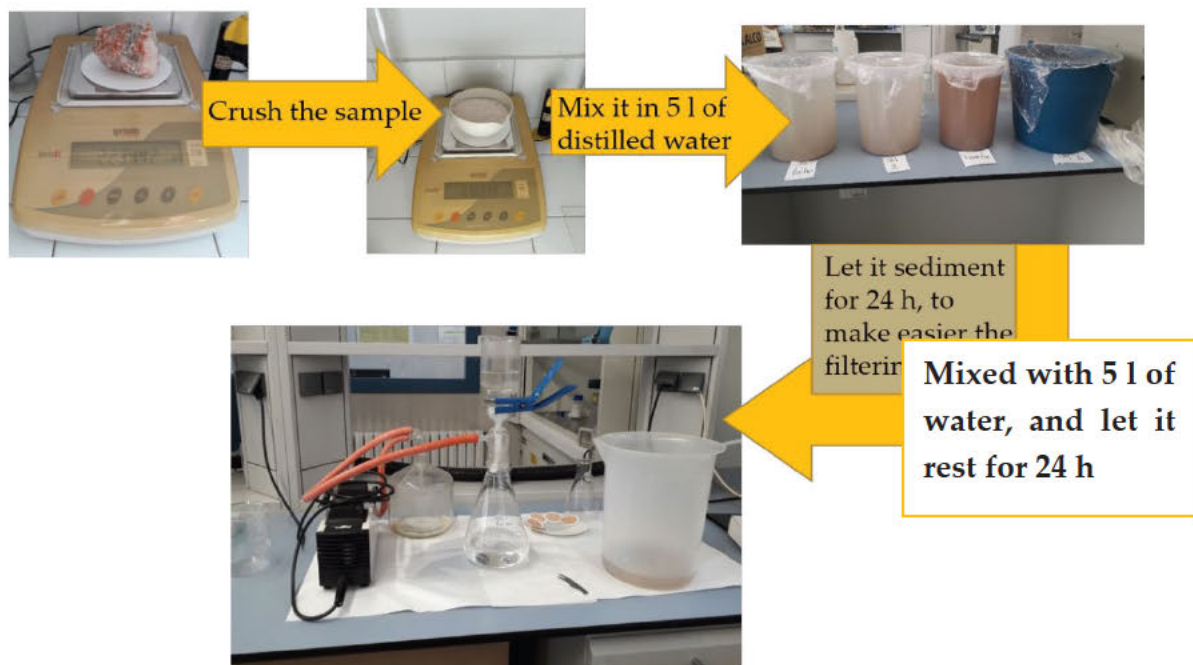


Figure 3.27 Equipment used for calculating the percentage of insoluble particles.

3.4.2.7 Insoluble particle analysis with geochemical techniques

3.4.2.7.1 Scanning Electron Microscopy (SEM) with Energy dispersive X-ray Spectroscopy (EDS)

SEM technology is based on the interactions between an electron beam and the surface of the sample. The Hitachi TM-1000 tabletop model (desktop model), located in the EPSEM geology laboratory, has been used in this study.

The interactions between the incident electrons and the sample cause the emission of secondary electrons, backscattered electrons and X-rays characteristic of the

elements present in the sample, for qualitative and, in some cases, semi-quantitative chemical analysis. In the SEM system, different detectors amplify the signal emitted by the surface of the sample when it is swept by a thin beam of electrons. The intensity of the amplified signal is displayed on a computer screen.

The images that can be obtained by SEM can be reached using the magnification of 10,000 or up to 50,000 times the size of the object. For the present study, the microscopic images have been produced from the backscattered electrons (BSE) emitted by the sample, whose intensity depends on a coefficient that is a function of the atomic number of the elements that make up the sample. It is because of this property that these images can be called compositional images or SEM-BSE. Additionally, as a consequence of the interaction of electrons with matter, it emits X-rays as a continuous spectrum along with several characteristic peaks, which depend on the elements present in the sample. Thanks to this phenomenon, it is possible to obtain qualitative, point or area chemical analyses, through the use of X-ray energy dispersive spectrometry (EDS).

3.4.2.7.2 X-ray powder diffraction (XRD)

X-ray powder diffraction (XRD) is a method of structural analysis, which allows minerals to be identified by their crystalline structure. It is therefore not a chemical analytical method, but it allows indirect estimating of the composition of the sample analyzed, with a good approximation of the content of major elements. This is because practically all minerals are crystalline, they have their chemical components (atoms, ions, molecules) regularly filling the space. Eventually, all crystals can develop polyhedral outer forms, although much of the mineral mass does not necessarily manifest this property. The regular distribution in space of the mineral components is described by the crystalline lattices, which reveal the periodic repetition of the mineral cell. The cell is the unit, in the shape of a parallelepiped, which is repeated identically and fills the entire space of the crystal (Melgarejo et al., 2010).

The unit cell forms crystalline lattices and these contain oriented lattice planes which are denoted by h , k , and l and this spacing, corresponds to the succession of these parallel planes which is called $dhkl$. Bragg's law of diffraction establishes that the X-rays are reflected on the crystal planes according to an angle θ that depends on the spacing $dhkl$, this law allows us to obtain for each mineral, the values of their spacing and thus compare them with standard mineral diffraction patterns for identification.

The method used in this study to perform these analyses is the method known as the crystalline powder method. The preparation of the samples for analysis was done by milling the material until obtaining an impalpable powder in an agate

mortar. Once the material was milled, it was mounted in an aluminum sample holder and placed on the diffractometer support. This diffractometer has performed the analysis in a 2θ range from 4° to 65° . The result is an X-ray diffractogram in which the intensities of the data are collected as a function of the diffraction angle 2θ .

The samples were pulverized in an agate mortar until obtaining a fine powder, was placed in a sampleholder and taken to analyse The X-ray diffraction analyses were made in a diffractometer located in the Science and Technology Centers of the University of Barcelona (CCiT-UB).

Mineralogy was determined by X-ray powder diffraction (XRPD). Measurements were taken using an automatic X'Pert diffractometer (PANalytical, Almelo, The Netherlands) graphite monochromator, automatic gap, $K\alpha$ -radiation of Cu at $\lambda = 1.54061 \text{ \AA}$, powered at 45 kV and 40 mA, scanning range $4\text{--}100^\circ$ with a 0.017° 2θ step scan and a 50 s measuring time. Identification and semiquantitative evaluation of phases were made on PANanalytical X'Pert HighScore software, Version 2.0.1 (PANalytical, Almelo, The Netherlands). Calculation of the Hinckley crystallinity index was obtained according to the instructions of Hinckley (Hinckley, 1962; Garcia-Valles et al., 2020).

3.5 Laser Scanner post-processing

3.5.1 Cyclone software (Leica Geosystems)

3.5.1.1 Cyclone REGISTER 360 (Leica Geosystems)



Chapter 4

Results and discussion

“All sorts of things can happen when you are open to new ideas and playing around with things.” — Stephanie Kwolek

Chapter 5

Conclusions

“Patience is bitter, but its fruit is sweet” – Jean-Jacques Rousseau.

5.1. Findings and hypothesis fulfilment

5.1.1 Hypothesis 1

The creation of a straightforward model that can predict the surface subsidence of the deposit, based on its geomechanical parameters, will provide solutions as well as improvements in the current mining management.

The approach proposed gives the possibility to determine the evolution of subsidence over time. The system allows the generation of average profiles at different points and an average subsidence profile of an area. The system also provides crucial information on mining activity behavior and gives the possibility to analyze the subsidence velocity of a representative period in a very simple and straightforward way, which represents one of the major strengths of the assessed technique. The tested numerical method has sufficient capacity to evaluate the time-dependent behavior of the potash and salt layers, using an indirect method—a 2D FEM model.

Although the model has some limitations in achieving subsidence stabilization in the final stage, it was proven as a particularly useful tool, especially during the years of mining activity. The model is able to analyze potential extraction scenarios and measures taken to reduce the subsidence whenever it is necessary and, therefore, reduce the environmental impact of the mining extraction and increase the operational safety levels.

5.1.2 Hypothesis 2

The geochemical characterization and the textural analysis of the interlayered mineralogy between the saline beds, as well as other insoluble mineralogy within them, will help to improve the health and safety of the underground mining infrastructure.

According to the obtained diffractions, SEM-EDS and XRD analysis a first estimation of the mineralogy can be stated. The minerals that could be detected are basically minerals from the potassium feldspar group, as well as from the chlorite group. Percentages of quartz, magnesite, gypsum and muscovite were also detected, and a small amount of iron oxides. Therefore, the minerals that form the insoluble particle fraction, are basically phyllosilicates.

This result gives a first approach to the whole variety of minerals that form this phase. It shows the importance of continuing the analysis to achieve a more accurate and clear result of the set of minerals forming the pelitic phase of the ore deposit.

5.1.3 Hypothesis 3

The characterization and evaluation of the surface subsidence basin and the main mining and geological parameters that influence the settlement process will improve land management, and contribute to reducing the current environmental impact.

The research developed introduces a new approach to characterize and predict a subsidence basin at any point in a targeted area. This new methodology allows working with large amounts of data, straightforwardly, to determine the main parameters of any subsidence basin. Therefore, having the potential to be used in other subsidence basin case studies.

Based on the methodology used, the analysis of 74 subsidence profiles has been done. Considering them, the area of interest has been divided into four different zones, according to cardinal directions, namely North, South, East and Southwest areas. The eastern zone is considered under a process of residual subsidence, while the other three belong to an active subsidence process. In that case, it has been possible to calculate their boundary angle and distance of influence. The highest value of the boundary angle is 71° in the northern zone, decreasing towards the south, thus, in the southwest part reaches a value of 52° , and eventually reaches its minimum value, 38° , in the southern zone. The distance of influence is inversely proportional to the boundary angle trend and, therefore, it has the smallest value in the northern part with 240 m, in the southwestern part has a value of 624 m and the maximum value is 988 m in the southern area. In addition, the presented methodology also allows to successfully approximate the subsidence curve to the Gaussian function using the least squares method, moreover, the characteristic parameters, such as the key parameters "i", "x", and " θ/l ", were identified following the same methodology. In addition, the algorithm that governs the subsidence process has been accurately calculated, allowing it to properly approximate its deformation at any given point in the area of interest. Furthermore, it can be stated that the forecast and prediction of the targeted subsidence basin have been accurately enhanced, resulting in an increase in safety levels, not only in the mining area but also in its surroundings.

Finally, the presented method can constitute an appropriate complement to upgrade the management of land subsidence in mining companies, not only for its adaptability and simplicity but also due to its effective, accurate and functional approach.

5.1.4 Hypothesis 4

The application of laser scanner technology for monitoring the stability of underground mine drifts will improve the health and safety of daily production activities in the deposit, reducing the possibility of sudden mine collapses.

The performance of the laser scanner technique has given a first approach to the results that can be achieved, showing that it represents a strong and accurate tool to quantify the displacements that happen in the mining drifts.

The implementation of this method gives the information to the mining technicians to detect weekly deformations, thus, making it possible to calculate their deformation rate.

This knowledge gives the possibility to notice if a mining drift is under a high or low deformation process, therefore making it possible to apply the required preventive measures.

5.2 Implication of the findings: Further research and improvements

The study offers some approaches to improve health and safety conditions and land management, as well as presents some characteristic values and expressions for modeling the behavior of the underground and surface environment. These results, obtained from two case studies, can also be used as reference values for other potash mines with similar operating characteristics.

Despite the results obtained, model improvements and continued research would be required to strengthen the current results and broaden the scope of the research in terms of improved working conditions and a more effective subsidence management system. Weaknesses, potential improvements and the need for additional research are discussed in the following paragraphs.

5.2.1 Hypothesis 1

The creation of a straightforward model that can predict the surface subsidence of the deposit, based on its geomechanical parameters, will provide solutions as well as improvements in the current mining management.

To improve the knowledge of the geomechanical behavior of the basin, an analysis to understand the development of the horizontal displacement based on the numerical model currently proposed should be carried out.

Moreover, it should be planned to update, during the following years, the numerical model using more sections to better approach the subsidence

movements in the targeted area, as well as to develop numerical modellings for other strategic areas of the Catalan Potash Basin, such as the main active ore deposit in the western area of the basin.

In addition, it is going to be evaluated a possible correlation between the underground displacement that the numerical model predicts and the displacement that currently happens in the active ore deposits. Nowadays, it does not exist any prediction model used in daily mining activities and it could be a useful tool to predict possible areas where high deformation will happen, increasing the health and safety levels of the mining activity.

Finally, it is suggested to analyze geomechanically all the lithologies that form the ore deposit, in order to not use bibliographical values, to create a more realistic approach.

5.2.2 Hypothesis 2

The geochemical characterization and the textural analysis of the interlayered mineralogy between the saline beds, as well as other insoluble mineralogy within them, will help to improve the health and safety of the underground mining infrastructure.

Nowadays, the analysis has been developed in a punctual targeted area. To have broader results, it is going to be carried out a characterization of the whole pelitic and insoluble mineralogy included in the saline lithologies.

To have more accurate information about the clayey material, it is going to be carried out analysis such as fluorescence (FRX) to know the chemistry of the pelitic materials interlayered within the saline lithologies. Additional analysis such as Differential thermal analysis (DTA) and thermal gravimetric analysis (TG) will allow us to determine the difference in thermal behavior between a substance and a reference material. Besides, ATD analysis tells us whether a reaction or physical change is endothermic or exothermic, while TG analysis tells us when a sample loses or gains weight. Moreover, a thin layer analysis should be done to complement the outcomes of the other performed techniques.

On the other hand, analyzing the clay layer through which the block has fallen could give an important insight. Locating these layers and checking if there is any correlation in the block falls that have happened up to now. Furthermore, to analyze the existing clays in the advance active zone, in order to detect possible unstable layers.

5.2.3 Hypothesis 3

The characterization and evaluation of the surface subsidence basin and the main mining and geological parameters that influence the settlement process will improve land management, and contribute to reducing the current environmental impact.

To characterize the whole subsidence basin is suggested the analysis of the whole group of active and abandoned ore deposits in the Catalan Potash Basin, updating the characterization of active and residual zones year by year to better predict the possible subsidence basin.

Determine which mining and geological characteristics that most influence the subsidence process in both active and abandoned mining areas of the CPB. Based on this analysis of parameters, determine the areas of risk of higher subsidence, and renovate the analysis periodically as the mine progresses.

5.2.4 Hypothesis 4

The application of laser scanner technology for monitoring the stability of underground mine drifts will improve the health and safety of daily production activities in the deposit, reducing the possibility of sudden mine collapses.

The laser scanner is a powerful tool that gives advantages regarding underground health and safety to production activities. However, it has to be properly and carefully used. It has been detected that in various cases, the topography of targets was not well updated, thus, locating the cloud point in the wrong position, preventing the comparison of the mining drift mesh with others.

In addition, another inconvenience of the laser scanner due to its high precision, if mining production machinery is, near the laser scanner, it can produce an error in the acquisition of the point cloud, causing a double mesh error. Therefore, when the laser scanner is under point cloud acquisition, it is highly recommended to have as few production machines powered on as possible.

5.3 Conclusions

It is confirmed that the Numerical 2D modelling is a useful tool to provide land management solutions as well as improvements in mine planning. The possibility to complement the model with more targeted areas and straightforwardly create new models gives enormous flexibility to predict and control vast surfaces in order to manage the affection for the environment.

Moreover, the methodology can be adapted to any other type of underground infrastructure.

The geochemical analysis of the pelitic materials interlayered and the insoluble mineralogy within saline lithologies has been developed successfully. The results state that the mineralogy of this material is extensive, thus, more analysis should be performed to determine all the minerals existing in it. Moreover, it is necessary to continue the analysis to increase the tested areas to have a broader result that can include all the extensions of the current active ore deposit. It can be stated that the study of the geochemical characterization of the insoluble and pelitic materials has given key information to improve the current health and safety levels of the underground mining infrastructure.

The subsidence characterization of the east part of the Catalan Potash Basin has been developed satisfactorily. Four different areas, including one under a process of residual subsidence, have been determined. The methodology implemented allowed us to work with high amounts of data straightforwardly. Its effectiveness and adaptability make this methodology a useful tool to be implemented for any mining company. Moreover, it has the potential to be used in other studies with a subsidence process undergone it.

By approximating the subsidence curve to the Gaussian function, the prediction of the subsidence process in the eastern zone has been updated. It has been possible to approximate the algorithm that governs the subsidence process, allowing it to adequately approximate its deformation at any point in the zone of interest. In this regard, the existing knowledge on the subsidence process has been increased, improving safety levels not only in the mining area but also in the surrounding area.

Finally, the usage of the laser scanner technique has given a good approach to understanding better the typology of displacements existing during the first stages of opening an underground mining drift in the case study. The technique is intuitive and has a straightforward approach to make it suitable to be used during the production stage, to control periodically the deformations in the mining facilities.

References

- Abu Seif, E.-S. S. (2014). Geotechnical Characteristics of Anhydrite/Gypsum Transformation in the Middle Miocene Evaporites, Red Sea Coast, Egypt. *Arabian Journal for Science and Engineering*, 39(1), 247–260. <https://doi.org/10.1007/s13369-013-0857-x>
- Adams, V., & Askenazi, A. (1999). *Building better products with finite element analysis*. Cengage Learning.
- Akcin, H. (2021). A GIS-based building risk assessment for the subsidence due to undercity coal mining activities in Zonguldak, Turkey. *Arabian Journal of Geosciences*, 14(5), 376. <https://doi.org/10.1007/s12517-021-06702-6>
- Alberto, W., Giardino, M., Martinotti, G., & Tiranti, D. (2008). Geomorphological hazards related to deep dissolution phenomena in the Western Italian Alps: Distribution, assessment and interaction with human activities. *Engineering Geology*, 99(3–4), 147–159. <https://doi.org/10.1016/j.enggeo.2007.11.016>
- Alonso, E. E., Berdugo, I. R., & Ramon, A. (2013). Extreme expansive phenomena in anhydritic-gypsiferous claystone: The case of Lilla tunnel. *Géotechnique*, 63(7), 584–612. <https://doi.org/10.1680/geot.12.P.143>
- Amelung, F., Galloway, D. L., Bell, J. W., Zebker, H. A., & Lacznia, R. J. (1999). Sensing the ups and downs of Las Vegas: InSAR reveals structural control of land subsidence and aquifer-system deformation. *Geology*, 27(6), 483. [https://doi.org/10.1130/0091-7613\(1999\)027<0483:STUADO>2.3.CO;2](https://doi.org/10.1130/0091-7613(1999)027<0483:STUADO>2.3.CO;2)
- Antonielli, B., Sciortino, A., Scancella, S., Bozzano, F., & Mazzanti, P. (2021). Tracking Deformation Processes at the Legnica Glogow Copper District (Poland) by Satellite InSAR—I: Room and Pillar Mine District. *Land*, 10(6), 653. <https://doi.org/10.3390/land10060653>
- Aplicación de datos del mes: Mapeo de Deformación del Terreno Usando DInSAR | UN-SPIDER Knowledge Portal. <https://www.un-spider.org/es/enlaces-y-recursos/fuentes-de-datos/daotm-mapeo-deformacion-dinsar>. Accedido 15 de julio de 2023.
- Arabmofrad, S., Bagheri, M., Rajabi, H., & Jafari, S. M. (2020). Nanoadsorbents and nanoporous materials for the food industry. In *Handbook of Food Nanotechnology* (pp. 107–159). Elsevier. <https://doi.org/10.1016/B978-0-12-815866-1.00004-2>

- Augarde, C. E., Lee, S. J., & Loukidis, D. (2021). Numerical modelling of large deformation problems in geotechnical engineering: A state-of-the-art review. *Soils and Foundations*, 61(6), 1718–1735. <https://doi.org/10.1016/j.sandf.2021.08.007>
- Aydin, A., & Johnson, A. M. (1983). Analysis of faulting in porous sandstones. *Journal of Structural Geology*, 5(1), 19–31.
- Ayora, C., Garcia-Veigas, J., & Pueyo, J.-J. (1994a). The chemical and hydrological evolution of an ancient potash-forming evaporite basin as constrained by mineral sequence, fluid inclusion composition, and numerical simulation. *Geochimica et Cosmochimica Acta*, 58(16), 3379–3394. [https://doi.org/10.1016/0016-7037\(94\)90093-0](https://doi.org/10.1016/0016-7037(94)90093-0)
- Ayora, C., Garcia-Veigas, J., & Pueyo, J.-J. (1994b). X-ray microanalysis of fluid inclusions and its application to the geochemical modeling of evaporite basins. *Geochimica et Cosmochimica Acta*, 58(1), 43–55. [https://doi.org/10.1016/0016-7037\(94\)90444-8](https://doi.org/10.1016/0016-7037(94)90444-8)
- Ayora, C., Taberner, C., Pierre, C., & Pueyo, J.-J. (1995). Modeling the sulfur and oxygen isotopic composition of sulfates through a halite-potash sequence: Implications for the hydrological evolution of the upper eocene Southpyrenean basin. *Geochimica et Cosmochimica Acta*, 59(9), 1799–1808. [https://doi.org/10.1016/0016-7037\(95\)00083-C](https://doi.org/10.1016/0016-7037(95)00083-C)
- Bahuguna, P. P., Srivastava, A. M. C., & Saxena, N. C. (1991). A critical review of mine subsidence prediction methods. *Mining Science and Technology*, 13(3), 369–382. [https://doi.org/10.1016/0167-9031\(91\)90716-P](https://doi.org/10.1016/0167-9031(91)90716-P)
- Bailey, S. W. (1988). Chlorites: Structures and crystal chemistry. Pp. 347-403 in: Hydrous Phyllosilicates (exclusive of micas)(SW Bailey, editor). *Reviews in Mineralogy*, 19.
- Bamler, R., & Hartl, P. (1998). Synthetic aperture radar interferometry. *Inverse Problems*, 14(4), R1–R54. <https://doi.org/10.1088/0266-5611/14/4/001>
- Barberán, M. L. (2000). *Análisis termomecánico de cavidades en rocas salinas rellenas de agregados porosos de sal*.
- Barnes, H. A., Hutton, J. F., & Walters, K. (1989). *An introduction to rheology* (Vol. 3). Elsevier.
- Barton, C. D., & Karathanasis, A. D. (2002). Clay minerals. In *Encyclopedia of soil science* (Vol. 10). Marcel Dekker: New York.

- Barton, N. (1973). Review of a new shear-strength criterion for rock joints. *Engineering Geology*, 7(4), 287–332.
- Barton, N. (1976). The shear strength of rock and rock joints. *International Journal of Rock Mechanics and Mining Sciences & Geomechanics Abstracts*, 13(9), 255–279.
- Barton, N. (2002). Some new Q-value correlations to assist in site characterisation and tunnel design. *International Journal of Rock Mechanics and Mining Sciences*, 39(2), 185–216. [https://doi.org/10.1016/S1365-1609\(02\)00011-4](https://doi.org/10.1016/S1365-1609(02)00011-4)
- Barton, N., & Bandis, S. (1982). Effects of block size on the shear behavior of jointed rock. *The 23rd US Symposium on Rock Mechanics (USRMS)*.
- Barton, N., & Choubey, V. (1977). The shear strength of rock joints in theory and practice. *Rock Mechanics*, 10, 1–54.
- Barton, N., Lien, R., & Lunde, J. (1974). Engineering classification of rock masses for the design of tunnel support. *Rock Mechanics Felsmechanik Mecanique Des Roches*, 6(4), 189–236. <https://doi.org/10.1007/BF01239496>
- Barton, N. R. (1978). International society for rock mechanics commission on standardization of laboratory and field tests: Suggested methods for the quantitative description of discontinuities in rock masses. *International Journal of Rock Mechanics and Mining Sciences & Geomechanics Abstracts*, 15(6), 319–368. [https://doi.org/10.1016/0148-9062\(78\)91472-9](https://doi.org/10.1016/0148-9062(78)91472-9)
- Bastidas, G., Soria, O., Mulas, M., Loaiza, S., & Bordehore, L. J. (2022). Stability Analysis of Lava Tunnels on Santa Cruz Island (Galapagos Islands, Ecuador) Using Rock Mass Classifications: Empirical Approach and Numerical Modeling. *Geosciences*, 12(10), 380. <https://doi.org/10.3390/geosciences12100380>
- Bechor, N. B., & Zebker, H. A. (2006). Measuring two-dimensional movements using a single InSAR pair. *Geophysical Research Letters*, 33(16).
- Bell, F. G., Stacey, T. R., & Genske, D. D. (2000). Mining subsidence and its effect on the environment: Some differing examples. *Environmental Geology*, 40(1–2), 135–152. <https://doi.org/10.1007/s002540000140>
- Bergaya, F., & Lagaly, G. (2013). *Handbook of clay science*. Newnes.
- Bieniawski, Z. T. (1973). Engineering classification of jointed rock masses. *Civil Engineering= Siviele Ingenieurswese*, 1973(12), 335–343.

- Bieniawski, Z. T. (1989). *Engineering rock mass classifications: A complete manual for engineers and geologists in mining, civil, and petroleum engineering*. John Wiley & Sons.
- Bieniawski, Z. T. (1993). Classification of Rock Masses for Engineering: The RMR System and Future Trends. In *Rock Testing and Site Characterization* (pp. 553–573). Elsevier. <https://doi.org/10.1016/B978-0-08-042066-0.50028-8>
- Bieniawski, Z. T. (1979). The geomechanics classification in rock engineering applications. *4th ISRM Congress*.
- Bitelli, G., Bonsignore, F., Del Conte, S., Novali, F., Pellegrino, I., & Vittuari, L. (2015). Integrated Use of Advanced InSAR and GPS Data for Subsidence Monitoring. In G. Lollino, A. Manconi, F. Guzzetti, M. Culshaw, P. Bobrowsky, & F. Luino (Eds.), *Engineering Geology for Society and Territory – Volume 5* (pp. 147–150). Springer International Publishing. https://doi.org/10.1007/978-3-319-09048-1_29
- Blewitt, G. (1997). Basics of the GPS technique: Observation equations. *Geodetic Applications of GPS, 1*, 46.
- Boyum, B. H. (1961). Subsidence case histories in Michigan mines. *The 4th US Symposium on Rock Mechanics (USRMS)*.
- Brady, B. H., & Brown, E. T. (2006). *Rock mechanics: For underground mining*. Springer science & business media.
- Bräuner, G. (1973). *Subsidence due to underground mining* (Issues 8571–8572). US Department of the Interior, Bureau of Mines.
- Brown, T. E. (2003). *Block Caving Geomechanics. 2nd edn. Indoeroopilly: Julius Kruttschnitt Mineral Research Centre*.
- Bryan, A., Bryan, J. G., & Fouche, J. (1964). Some problems of strata control and support in pillar workings. *The Mining Engineer, 123*(41), 238–266.
- Burbey, T. (2002). The influence of faults in basin-fill deposits on land subsidence, Las Vegas Valley, Nevada, USA. *Hydrogeology Journal, 10*(5), 525–538. <https://doi.org/10.1007/s10040-002-0215-7>
- Bürgmann, R., Rosen, P. A., & Fielding, E. J. (2000). Synthetic aperture radar interferometry to measure Earth's surface topography and its deformation. *Annual Review of Earth and Planetary Sciences, 28*(1), 169–209.

Camara Zapata, E. (2019). *Ensayos WST de probetas de rocas salinas a distintas velocidades de carga*. Universitat Politècnica de Catalunya.

Campos de Orellana, A. C. (1996). Pressure solution creep and non-associated plasticity in the mechanical behavior of potash mine openings. *International Journal of Rock Mechanics and Mining Sciences & Geomechanics Abstracts*, 33(4), 347–370.

Carter, N. L., Horseman, S. T., Russell, J. E., & Handin, J. (1993). Rheology of rock salt. *Journal of Structural Geology*, 15(9–10), 1257–1271.

Cendón, D. I., Ayora, C., Pueyo, J. J., & Taberner, C. (2003). The geochemical evolution of the Catalan potash subbasin, South Pyrenean foreland basin (Spain). *Chemical Geology*, 200(3–4), 339–357. [https://doi.org/10.1016/S0009-2541\(03\)00195-5](https://doi.org/10.1016/S0009-2541(03)00195-5)

Chakraverty, S., & Pradhan, K. K. (2018). *Computational structural mechanics: Static and dynamic behaviors*. Academic Press.

Chen, K.-S. (2016). *Principles of synthetic aperture radar imaging: A system simulation approach* (Vol. 2). CRC Press.

Cheng, A. H.-D., & Cheng, D. T. (2005). Heritage and early history of the boundary element method. *Engineering Analysis with Boundary Elements*, 29(3), 268–302.

Clough, R. W. (1980). The finite element method after twenty-five years: A personal view. *Computers & Structures*, 12(4), 361–370.

Clough, R. W. (1990). Original formulation of the finite element method. *Finite Elements in Analysis and Design*, 7(2), 89–101.

Clough, R. W. (1960). *The Finite Element Method in Plane Stress Analysis*.

Clough, W. y Schmidt, B. (1981). Design and performance of excavations and tunnels in soft clay. *Soft Clay Engineering*, Elsevier, Amsterdam.

Concha, A., Ripoll, J., Piña, J., Gabàs, A., & Piña, P. (2010). *Two-dimensional coupled numerical modelling of subsidence due to water extraction at the Lower Llobregat River, Spain*.

Cooper, S., & Durrant-Whyte, H. (1994). A Kalman filter model for GPS navigation of land vehicles. *Proceedings of IEEE/RSJ International Conference on Intelligent Robots and Systems (IROS'94)*, 1, 157–163. <https://doi.org/10.1109/IROS.1994.407396>

Costa, E., Garcés, M., Lopez-Blanco, M., Beamud, E., Gómez-Paccard, M., & Larrasoaña, J. C. (2009). Closing and continentalization of the South Pyrenean foreland basin (NE Spain): Magnetostratigraphical constraints: Ebro basin closing and continentalization chronology. *Basin Research*, no-no. <https://doi.org/10.1111/j.1365-2117.2009.00452.x>

Coulomb, C. A. (1776). *Essai sur une application des règles de maximis & minimis à quelques problèmes de statique à l'architecture*. De l'Imprimerie Royale.

Crane, W. R. (1931). *Essential Factors Influencing Subsidence and Ground Movement* (Vol. 6501). US Department of Commerce, Bureau of Mines.

Dai, H. (2018). Mining subsidence variables and their time-space relationship description. *China Coal Soc*, 43, 450–459.

Davis, G. H., Reynolds, S. J., & Kluth, C. F. (2011). *Structural geology of rocks and regions*. John Wiley & Sons.

De Bruyn, I. A., Bell, F. G., & Jermy, C. A. (2000). The problem of sinkhole formation in two dolomite areas of South Africa. *ISRM International Symposium*.

Diao, X., Wu, K., Chen, R., & Yang, J. (2019). Identifying the Cause of Abnormal Building Damage in Mining Subsidence Areas Using InSAR Technology. *IEEE Access*, 7, 172296–172304. <https://doi.org/10.1109/ACCESS.2019.2956094>

Diao, X., Wu, K., Zhou, D., & Li, L. (2016). Integrating the probability integral method for subsidence prediction and differential synthetic aperture radar interferometry for monitoring mining subsidence in Fengfeng, China. *Journal of Applied Remote Sensing*, 10(1), 016028. <https://doi.org/10.1117/1.JRS.10.016028>

Diez, R. R., & Alvarez, J. T. (2000). Hypothesis of the multiple subsidence trough related to very steep and vertical coal seams and its prediction through profile functions. *Geotechnical & Geological Engineering*, 18, 289–311.

Donnelly, L. J. (2009). A review of international cases of fault reactivation during mining subsidence and fluid abstraction. *Quarterly Journal of Engineering Geology and Hydrogeology*, 42(1), 73–94. <https://doi.org/10.1144/1470-9236/07-017>

Dusseault, M. B., & Fordham, C. J. (1993). Time-dependent behavior of rocks. In *Rock testing and site characterization* (pp. 119–149). Elsevier.

Fàbrega C, Bonvehí A, & Redó S. (2007). *Quan les roques parlen... Punts d'interès geològic a l'entorn de Súria*. Ajuntament de Súria.

- Ferretti, A., Monti-Guarnieri, A., Prati, C., Rocca, F., & Massonet, D. (2007). *InSAR principles-guidelines for SAR interferometry processing and interpretation* (Vol. 19).
- Fredrich, J. T., Arguello, J. G., Deitrick, G. L., & de Rouffignac, E. P. (2000). Geomechanical modeling of reservoir compaction, surface subsidence, and casing damage at the Belridge diatomite field. *SPE Reservoir Evaluation & Engineering*, 3(04), 348–359.
- Galve, J. P., Bonachea, J., Remondo, J., Gutiérrez, F., Guerrero, J., Lucha, P., Cendrero, A., Gutiérrez, M., & Sánchez, J. A. (2008). Development and validation of sinkhole susceptibility models in mantled karst settings. A case study from the Ebro valley evaporite karst (NE Spain). *Engineering Geology*, 99(3–4), 185–197. <https://doi.org/10.1016/j.enggeo.2007.11.011>
- Garcia-Castellanos, D., Vergés, J., Gaspar-Escribano, J., & Cloetingh, S. (2003). Interplay between tectonics, climate, and fluvial transport during the Cenozoic evolution of the Ebro Basin (NE Iberia): TECTONICS, CLIMATE, AND DRAINAGE. *Journal of Geophysical Research: Solid Earth*, 108(B7). <https://doi.org/10.1029/2002JB002073>
- Garcia-Valles, M., Alfonso, P., Martínez, S., & Roca, N. (2020). Mineralogical and thermal characterization of kaolinitic clays from Terra Alta (Catalonia, Spain). *Minerals*, 10(2), 142.
- Geertsma, J. (1973). *A basic theory of subsidence due to reservoir compaction; the homogeneous case*.
- Geertsma, J., & Opstal, V. (1973). *A numerical technique for predicting subsidence above compacting reservoirs, based on the nucleus of strain concept*.
- Giambastiani, M. (2020). Geomechanical Characterization of Evaporitic Rocks. In M. Kanji, M. He, & L. Ribeiro e Sousa (Eds.), *Soft Rock Mechanics and Engineering* (pp. 129–161). Springer International Publishing. https://doi.org/10.1007/978-3-030-29477-9_6
- Grafarend, E. W., & Shan, J. (2002). GPS Solutions: Closed Forms, Critical and Special Configurations of P4P. *GPS Solutions*, 5(3), 29–41. <https://doi.org/10.1007/PL00012897>
- Guo, Q., Meng, X., Li, Y., Lv, X., & Liu, C. (2021). A prediction model for the surface residual subsidence in an abandoned goaf for sustainable development of resource-exhausted cities. *Journal of Cleaner Production*, 279, 123803. <https://doi.org/10.1016/j.jclepro.2020.123803>

- Guo, W., Zhao, G., Bai, E., Guo, M., & Wang, Y. (2021). Effect of overburden bending deformation and alluvium mechanical parameters on surface subsidence due to longwall mining. *Bulletin of Engineering Geology and the Environment*, 80(3), 2751–2764. <https://doi.org/10.1007/s10064-020-02091-4>
- Gutiérrez, F., Guerrero, J., & Lucha, P. (2008). A genetic classification of sinkholes illustrated from evaporite paleokarst exposures in Spain. *Environmental Geology*, 53(5), 993–1006. <https://doi.org/10.1007/s00254-007-0727-5>
- Halbaum, H. W. (1905). The great planes of strain in the absolute roof of mines. *Transactions of the Institution of Mining Engineers*.
- Hardie, L. A., & Eugster, H. (1970). The evolution of closed-basin brines. *Mineral. Soc. Amer. Spec. Pap*, 3, 273–290.
- Hardie, L. A., & Eugster, H. P. (1971). The depositional environment of marine evaporites: a case for shallow, clastic accumulation. *Sedimentology*, 16(3–4), 187–220. <https://doi.org/10.1111/j.1365-3091.1971.tb00228.x>
- Hillier, S. (2003). Chlorite in sediments. In G. V. Middleton, M. J. Church, M. Coniglio, L. A. Hardie, & F. J. Longstaffe (Eds.), *Encyclopedia of Sediments and Sedimentary Rocks* (pp. 123–127). Springer Netherlands. https://doi.org/10.1007/978-1-4020-3609-5_43
- Hinckley, D. N. (1962). Variability in “crystallinity” values among the kaolin deposits of the coastal plain of Georgia and South Carolina. *Clays and Clay Minerals*, 11, 229–235.
- Hoek, E. (2007). Practical rock engineering. 2007. *Online. Ed. Rocscience*.
- Hoek, E., & Brown, E. T. (1980). Empirical strength criterion for rock masses. *Journal of the Geotechnical Engineering Division*, 106(9), 1013–1035.
- Hoek, E., & Brown, E. T. (1990). *Underground excavations in rock*. London: Institute of Mining and Metallurgy. Spon Press, Taylor & Francis.
- Hoek, E., & Brown, E. T. (1988). The Hoek-Brown failure criterion—a 1988 update. *Proc. 15th Can. Rock Mech. Symp, Toronto, Canada*.
- Hoek, E., Carranza-Torres, C., & Corkum, B. (2002). Hoek-Brown failure criterion-2002 edition. *Proceedings of NARMS-Tac*, 1(1), 267–273.
- Hohlfelder, J. J., & Hadley, G. R. (1979). Laboratory studies of water transport in rock salt. *Letters in Heat and Mass Transfer*, 6(4), 271–279.

Hu, J., Li, Z. W., Ding, X. L., Zhu, J. J., Zhang, L., & Sun, Q. (2014). Resolving three-dimensional surface displacements from InSAR measurements: A review. *Earth-Science Reviews*, 133, 1–17.

Huang, P. M., & Wang, M. K. (2005). MINERALS, PRIMARY. In D. Hillel (Ed.), *Encyclopedia of Soils in the Environment* (pp. 500–510). Elsevier. <https://doi.org/10.1016/B0-12-348530-4/00464-1>

Hubbert, M. K. (1956). Darcy's law and the field equations of the flow of underground fluids. *Transactions of the AIME*, 207(01), 222–239.

Huggett, J. M. (2015). Clay Minerals. In *Reference Module in Earth Systems and Environmental Sciences*. Elsevier. <https://doi.org/10.1016/B978-0-12-409548-9.09519-1>

Hunsche, U., & Hampel, A. (1999). Rock salt—The mechanical properties of the host rock material for a radioactive waste repository. *Engineering Geology*, 52(3–4), 271–291.

Hunt, S. R. (1980). *Surface subsidence due to coal mining in Illinois*. University of Illinois at Urbana-Champaign.

Hussain, M. A., Chen, Z., Shoaib, M., Shah, S. U., Khan, J., & Ying, Z. (2022). Sentinel-1A for monitoring land subsidence of coastal city of Pakistan using Persistent Scatterers In-SAR technique. *Scientific Reports*, 12(1), 5294. <https://doi.org/10.1038/s41598-022-09359-7>

International Fertilizer Association. (2019). *International Fertilizer Association, Executive Summary Fertilizer Outlook 2019 – 2023* (IFA Annual Conference).

Jaeger, J. C., Cook, N. G., & Zimmerman, R. (2009). *Fundamentals of rock mechanics*. John Wiley & Sons.

Jeremic, M. L. (1994). *Rock mechanics in salt mining: AA Balkema. Rotterdam, The Netherlands*.

JM, Rios. (1963). *Materiales salinos del suelo Español*. Instituto Geologico i Minero de España.

Johnston, C. T. (2018). Clay mineral–water interactions. In *Developments in Clay Science* (Vol. 9, pp. 89–124). Elsevier. <https://doi.org/10.1016/B978-0-08-102432-4.00004-4>

Karmis, M., Jarosz, A., Schilizzi, P., & Agioutantis, Z. (1987). Surface deformation characteristics above undermined areas: Experiences from the Eastern United States Coalfield. *Civ. Eng. Trans., Inst. Eng., Aust.:(Australia)*.

Ketelaar, V. G. (2009). *Satellite radar interferometry: Subsidence monitoring techniques* (Vol. 14). Springer Science & Business Media.

Kolivand, F., & Rahmamejad, R. (2018). Estimation of geotechnical parameters using Taguchi's design of experiment (DOE) and back analysis methods based on field measurement data: Case study: Tehran Metro line no. 7. *Bulletin of Engineering Geology and the Environment*, 77(4), 1763–1779. <https://doi.org/10.1007/s10064-017-1042-3>

Kotal, M., & Bhowmick, A. K. (2015). Polymer nanocomposites from modified clays: Recent advances and challenges. *Progress in Polymer Science*, 51, 127–187. <https://doi.org/10.1016/j.progpolymsci.2015.10.001>

Labuz, J. F., & Zang, A. (2012). Mohr–Coulomb failure criterion. *Rock Mechanics and Rock Engineering*, 45, 975–979.

Lawongkerd, J., Shiau, J., Keawsawasvong, S., Seehavong, S., & Jamsawang, P. (2022). Design Equations for Predicting Stability of Unlined Horseshoe Tunnels in Rock Masses. *Buildings*, 12(11), 1800. <https://doi.org/10.3390/buildings12111800>

Lawson, H. E., Tesarik, D., Larson, M. K., & Abraham, H. (2017). Effects of overburden characteristics on dynamic failure in underground coal mining. *International Journal of Mining Science and Technology*, 27(1), 121–129. <https://doi.org/10.1016/j.ijmst.2016.10.001>

Li, C. C. (2017). *Rockbolting: Principles and applications*. Butterworth-Heinemann.

Li, P., Tan, Z., & Yan, L. (2018). A Shaft Pillar Mining Subsidence Calculation Using Both Probability Integral Method and Numerical Simulation. *Computer Modeling in Engineering & Sciences*, 117(2), 231–250. <https://doi.org/10.31614/cmescs.2018.02573>

Li, W., Li, D., Yang, S., Xu, Z., & Zhao, W. (2010). Design and Analysis of a New GPS Algorithm. *2010 IEEE 30th International Conference on Distributed Computing Systems*, 40–51. <https://doi.org/10.1109/ICDCS.2010.53>

Liu, H.-P., Anderson, D. L., & Kanamori, H. (1976). Velocity dispersion due to anelasticity; implications for seismology and mantle composition. *Geophysical Journal International*, 47(1), 41–58.

- Logan, D. L. (2011). *A first course in the finite element method, 5th*. Cengage.
- Logan, D. L. (2022). *First Course in the Finite Element Method, Enhanced Edition, SI Version*. Cengage Learning.
- López-Blanco, M., Marzo, M., Burbank, D. W., Vergés, J., Roca, E., Anadón, P., & Piña, J. (2000). Tectonic and climatic controls on the development of foreland fan deltas: Montserrat and Sant Llorenç del Munt systems (Middle Eocene, Ebro Basin, NE Spain). *Sedimentary Geology*, 138(1–4), 17–39. [https://doi.org/10.1016/S0037-0738\(00\)00142-1](https://doi.org/10.1016/S0037-0738(00)00142-1)
- Lowson, A. R., & Bieniawski, Z. T. (2013). Critical assessment of RMR based tunnel design practices: A practical engineer's approach. *Proceedings of the SME, Rapid Excavation and Tunnelling Conference, Washington, DC, USA*, 6, 23–26.
- Madsen, S. N., & Zebker, H. A. (1992). Automated absolute phase retrieval in across-track interferometry. In: *IGARSS'92; Proceedings of the 12th Annual International Geoscience and Remote Sensing Symposium, Houston, TX, May 26-29, 1992. Vol. 2 (A93-47551 20-43)*.
- Mainardi, F., & Spada, G. (2011). Creep, relaxation and viscosity properties for basic fractional models in rheology. *The European Physical Journal Special Topics*, 193(1), 133–160.
- Mair, R.J., Taylor, R.N. & Bracegirdle, A. (1993). Subsurface settlement profiles above tunnels in clays. *Géotechnique*, 43(2), pp.315-320.
- Marketos, G., Broerse, T., Spiers, C. J., & Govers, R. M. A. (2015). *Long-term subsidence study of the Ameland gas field: Time-dependence induced by rock salt flow*.
- Martinez Garcia, I., Sanchez Espina, A., Gillot, E., Coullault Santurtun, J., & Velasco Isusi, C. (2016, September 4). *History of Geophysical Work for Potash Salt Investigation in the Catalonian Potash Basin—ICL Iberia Súrria & Sallent*. Near Surface Geoscience 2016 - 22nd European Meeting of Environmental and Engineering Geophysics, Barcelona, Spain. <https://doi.org/10.3997/2214-4609.201601933>
- Massonnet, D., & Feigl, K. L. (1998). Radar interferometry and its application to changes in the Earth's surface. *Reviews of Geophysics*, 36(4), 441–500.
- Mehranpour, M. H., & Kulatilake, P. H. (2016). Comparison of six major intact rock failure criteria using a particle flow approach under true-triaxial stress condition. *Geomechanics and Geophysics for Geo-Energy and Geo-Resources*, 2, 203–229.

- Melgarejo, J. C., Proenza, J. A., Galí, S., & Llovet, X. (2010). Techniques of mineral characterization and their use in mining exploration and exploitation. *Boletín de La Sociedad Geológica Mexicana*, 62(1), 1–23.
- Modeste, G., Doubre, C., & Masson, F. (2021). Time evolution of mining-related residual subsidence monitored over a 24-year period using InSAR in southern Alsace, France. *International Journal of Applied Earth Observation and Geoinformation*, 102, 102392. <https://doi.org/10.1016/j.jag.2021.102392>
- Mohr, O. (1900). Welche Umstände bedingen die Elastizitätsgrenze und den Bruch eines Materials. *Zeitschrift Des Vereins Deutscher Ingenieure*, 46(1524–1530), 1572–1577.
- Moreira, A., Prats-Iraola, P., Younis, M., Krieger, G., Hajnsek, I., & Papathanassiou, K. P. (2013). A tutorial on synthetic aperture radar. *IEEE Geoscience and Remote Sensing Magazine*, 1(1), 6–43.
- Nadai, A. (1950). *Theory of flow and fracture of solids, Vol. 1*. Mc Graw Hill, New York.
- National Coal Board. (1975). Subsidence engineers' handbook. *Production Department, London*.
- Nie, L., Zhang, M., & Jian, H. (2013). Analysis of surface subsidence mechanism and regularity under the influence of seism and fault. *Natural Hazards*, 66(2), 773–780. <https://doi.org/10.1007/s11069-012-0515-8>
- O'Reilly, M.P. & New, B. M. (1982). Settlements above tunnels in the United Kingdom-their magnitude and prediction. *Tunnelling'82, The Institution of Mining and Metallurgy, London*, pp.173-181.
- O'Reilly, M.P., M. P., & New, B. M. (1982). *Settlements above tunnels in the United Kingdom-their magnitude and prediction*.
- Olander, D. R. (1980). Interaction of stresses with inclusions in solids—A review. *Journal of Nuclear Materials*, 92(2–3), 163–183.
- Olivella, S., Carrera, J., Gens, A., & Alonso, E. E. (1994). Nonisothermal multiphase flow of brine and gas through saline media. *Transport in Porous Media*, 15, 271–293.
- Olivella, S., Carrera, J., Gens, A., & Alonso, E. E. (1996). Porosity variations in saline media caused by temperature gradients coupled to multiphase flow and dissolution/precipitation. *Transport in Porous Media*, 25, 1–25.

- Paraskevopoulou, C., Vlachopoulos, N., & Diederichs, M. S. (2012). Long term tunnel behaviour and support response analysis using 2D numerical modelling methods. *46th US Rock Mechanics/Geomechanics Symposium*.
- Parmar, H., Yarahmadi Bafghi, A., & Najafi, M. (2019). Impact of ground surface subsidence due to underground mining on surface infrastructure: The case of the Anomaly No. 12 Sechahun, Iran. *Environmental Earth Sciences*, 78(14), 409. <https://doi.org/10.1007/s12665-019-8424-8>
- Patton, F. D. (1966). Multiple modes of shear failure in rock. *1st ISRM Congress*.
- Peck, R. B. (1969). Deep Excavations and Tunneling in soft Ground. *Proc. 7th Int. Conf. Soil Mech.*, 225–290.
- Peng, S. S. (1992). *Surface subsidence engineering*.
- Peng, S. S. (2020). *Surface Subsidence Engineering: Theory and Practice*. Csiro Publishing.
- Pepe, A., & Calò, F. (2017). A review of interferometric synthetic aperture RADAR (InSAR) multi-track approaches for the retrieval of Earth's surface displacements. *Applied Sciences*, 7(12), 1264.
- Pipia, L., Aguasca, A., Fabregas, X., Mallorqui, J. J., Lopez-Martinez, C., & Marturia, J. (2007). Mining induced subsidence monitoring in urban areas with a ground-based SAR. *2007 Urban Remote Sensing Joint Event*, 1–5.
- Potts, D. M., Zdravković, L., Addenbrooke, T. I., Higgins, K. G., & Kovačević, N. (2001). *Finite element analysis in geotechnical engineering: Application* (Vol. 2). Thomas Telford London.
- Potts, E. L. (1951). Ground movement in mining areas. *Planning Outlook*, 2(3), 24–32.
- Pueyo Mur, Juan José. (1975). *Estudio petrológico y geoquímico de los yacimientos potásicos de Cardona, Súria, Sallent y Balsareny (Barcelona, España)* [Universitat de Barcelona. Departament de Petrologia i Geoquímica]. <http://hdl.handle.net/10803/669746>
- Puigdefàbregas, C., & Souquet, P. (1986). Tecto-sedimentary cycles and depositional sequences of the Mesozoic and Tertiary from the Pyrenees. *Tectonophysics*, 129(1–4), 173–203. [https://doi.org/10.1016/0040-1951\(86\)90251-9](https://doi.org/10.1016/0040-1951(86)90251-9)

- Pusch, R. (2006). Chapter 6 Mechanical Properties of Clays and Clay Minerals. In *Developments in Clay Science* (Vol. 1, pp. 247–260). Elsevier. [https://doi.org/10.1016/S1572-4352\(05\)01006-8](https://doi.org/10.1016/S1572-4352(05)01006-8)
- Rankin, W. J. (1988). Ground movements resulting from urban tunneling: Predictions and effects. *Engineering Geology of Underground Movements*, 5, 79–82.
- Rao, P. P., & Morris, P. J. (2006). Use of finite element methods in frequency domain aeroacoustics. *AIAA Journal*, 44(7), 1643–1652.
- Rateb, A., & Abotalib, A. Z. (2020). Inferencing the land subsidence in the Nile Delta using Sentinel-1 satellites and GPS between 2015 and 2019. *Science of The Total Environment*, 729, 138868. <https://doi.org/10.1016/j.scitotenv.2020.138868>
- Rice, G. S. (1934). Ground movement from mining in Brier Hill mine, Norway, Michigan. *Mining and Metallurgy*, 15(325), 12–14.
- Roberts, D. G., & Bally, A. W. (2012). *Regional geology and tectonics: Phanerozoic passive margins, cratonic basins and global tectonic maps* (Vol. 1). Elsevier.
- Rosell, L., & Pueyo, J. (1997). Second marine evaporitic phase in the south Pyrenean Foredeep: The Priabonian potash basin (Late Eocene; autochthonous-allochthonous Zone). *Sedimentary Deposition in Rift and Foreland Basins in France and Spain (Paleogene and Lower Neogene)*. Columbia Univ. Press, New York, 358–387.
- Rosell Ortiz, L. L. (1983). *Estudi petrològic, sedimentològic i geoquímic de la formació de sals potàssiques de Navarra (Eocè superior)* [PhD Thesis]. Tesis Doctoral. Universidad de Barcelona.
- Rošer, J., Potočnik, D., & Vulić, M. (2018). Analysis of dynamic surface subsidence at the underground coal mining site in Velenje, Slovenia through modified sigmoidal function. *Minerals*, 8(2), 74.
- Roylance, D. (2001). Engineering viscoelasticity. *Department of Materials Science and Engineering—Massachusetts Institute of Technology, Cambridge MA, 2139*, 1–37.
- Sáez, A., Vergés, J., Taberner, C., Pueyo, J., Muñoz, J., & Busquets, P. (1991). Eventos evaporíticos paleógenos en la Cuenca Antepais Surpirenaica: causas climáticas—causas tectónicas. *Libro-Guía Excursión*, 5.
- Salmi, E. F., Nazem, M., & Karakus, M. (2017). The effect of rock mass gradual deterioration on the mechanism of post-mining subsidence over shallow abandoned coal mines. *International Journal of Rock Mechanics and Mining Sciences*, 91, 59–71. <https://doi.org/10.1016/j.ijrmms.2016.11.012>

- Sanmiquel, L., Bascompta, M., Vintro, C., & Yubero, T. (2018). Subsidence management system for underground mining. *Minerals*, 8(6), 243. <https://doi.org/10.3390/min8060243>
- Sanz, J., Tomasa, O., Jimenez-Franco, A., & Sidki-Rius, N. (2022). *Elements and Mineral Resources*. Springer International Publishing. <https://doi.org/10.1007/978-3-030-85889-6>
- Sasaoka, T., Takamoto, H., Shimada, H., Oya, J., Hamanaka, A., & Matsui, K. (2015). Surface subsidence due to underground mining operation under weak geological condition in Indonesia. *Journal of Rock Mechanics and Geotechnical Engineering*, 7(3), 337–344. <https://doi.org/10.1016/j.jrmge.2015.01.007>
- Schmidt, B. (1969). *Settlements and ground movements associated with tunnelling in soil*. University of Illinois.
- Schowalter, W. R. (1978). *Mechanics of non-Newtonian fluids*. Pergamon.
- Schulze, D. G. (2005). Clay minerals. In D. Hillel (Ed.), *Encyclopedia of Soils in the Environment* (pp. 246–254). Elsevier. <https://doi.org/10.1016/B0-12-348530-4/00189-2>
- Schütt, B. (1998). Reconstruction of paleoenvironmental conditions by investigation of Holocene playa sediments in the Ebro Basin, Spain: Preliminary results. *Geomorphology*, 23(2–4), 273–283. [https://doi.org/10.1016/S0169-555X\(98\)00009-9](https://doi.org/10.1016/S0169-555X(98)00009-9)
- Singh, G. S. P., Singh, U. K., & Murthy, V. M. S. R. (2010). Applications of Numerical Modelling for Strata Control in Mines. *Geotechnical and Geological Engineering*, 28(4), 513–524. <https://doi.org/10.1007/s10706-010-9324-6>
- Spencer, R. J. (2000). Sulfate Minerals in Evaporite Deposits. *Reviews in Mineralogy and Geochemistry*, 40(1), 173–192. <https://doi.org/10.2138/rmg.2000.40.3>
- Spiers, C. J., Schutjens, P., Brzesowsky, R. H., Peach, C. J., Liezenberg, J. L., & Zwart, H. J. (1990). Experimental determination of constitutive parameters governing creep of rock salt by pressure solution. *Geological Society, London, Special Publications*, 54(1), 215–227.
- Spiers, C. J., Urai, J. L., Lister, G. S., Boland, J. N., & Zwart, H. J. (1986). *The influence of fluid-rock interaction on the rheology of salt rock*. Commission of the European Communities.
- Stephan M, Jasinski. (2021). *2018 Minerals Yearbook, potash (advance release)* (Minerals Yearbook). <https://d9-wret.s3.us-west->

2.amazonaws.com/assets/palladium/production/atoms/files/myb1-2018-potas.pdf

Szwedzicki, T. (1999). Sinkhole formation over hard rock mining areas and its risk implications. *Transactions of the Institution of Mining and Metallurgy. Section A. Mining Industry*, 108.

Taberner, C., Dinarès-Turell, J., Giménez, J., & Docherty, C. (1999). Basin infill architecture and evolution from magnetostratigraphic cross-basin correlations in the southeastern Pyrenean foreland basin. *Geological Society of America Bulletin*, 111(8), 1155–1174. [https://doi.org/10.1130/0016-7606\(1999\)111<1155:BIAAEF>2.3.CO;2](https://doi.org/10.1130/0016-7606(1999)111<1155:BIAAEF>2.3.CO;2)

Torrijo, F. J., Fuentes, R., Boix, A., & Bracchi, P. (2020). Identification and mitigation of sinkhole hazards in an evaporite karst area (perdiguera, Spain). *The International Archives of the Photogrammetry, Remote Sensing and Spatial Information Sciences, XLIV-M-1–2020*, 707–712. <https://doi.org/10.5194/isprs-archives-XLIV-M-1-2020-707-2020>

Trusheim, F. (1960). Mechanism of salt migration in northern Germany. *AAPG Bulletin*, 44(9), 1519–1540.

Turner, M. J., Clough, R. W., Martin, H. C., & Topp, L. J. (1956). Stiffness and deflection analysis of complex structures. *Journal of the Aeronautical Sciences*, 23(9), 805–823.

Pueyo Anchuela, O., Pocoví Juan, A., Universidad de Zaragoza, Casas Sainz, A., Gracia Abadias, J., Universidad de Zaragoza, & Liesa Carrera, C. (2017). Integrated approach for sinkhole evaluation and evolution prediction in the Central Ebro Basin (NE Spain). *International Journal of Speleology*, 46(2), 237–249. <https://doi.org/10.5038/1827-806X.46.2.2064>

Urai, J. L., Schléder, Z., Spiers, C. J., & Kukla, P. A. (2008). Flow and transport properties of salt rocks. *Dynamics of Complex Intracontinental Basins: The Central European Basin System*, 277–290.

Urai, J. L., & Spiers, C. J. (2017). The effect of grain boundary water on deformation mechanisms and rheology of rock salt during long-term deformation. In *The mechanical behavior of salt—understanding of THMC processes in salt* (pp. 149–158). CRC Press.

USGS. (2022). *Mineral commodity summaries 2022*. <https://doi.org/10.3133/mcs2022>

- Utrilla, R., Pierre, C., Orti, F., & Pueyo, J. J. (1992). Oxygen and sulphur isotope compositions as indicators of the origin of Mesozoic and Cenozoic evaporites from Spain. *Chemical Geology*, 102(1–4), 229–244. [https://doi.org/10.1016/0009-2541\(92\)90158-2](https://doi.org/10.1016/0009-2541(92)90158-2)
- Valentí Masachs. (1962). *La edad, el origen, y los movimientos de las sales paleogenas de la cuenca del Ebro*: Institut Geologic i Miner de la Diputació de Barcelona.
- Van Sambeek, L. L. (1992). Testing and modelling of backfill used in salt and potash mines. *Proceedings of the Rock Support in Mining and Underground Construction, Balkema, Rotterdam 1992*, 583–589.
- Van Sambeek, L. L. (1997). Measuring Surface subsidence at Colonsay, Saskatchewan, Potash Mine. *Proceedings of the Rock Mechanics and Ground Control in the Soft Rock and Coal Industries Workshop*.
- Vatansever, S., & Butun, I. (2017). A broad overview of GPS fundamentals: Now and future. *2017 IEEE 7th Annual Computing and Communication Workshop and Conference (CCWC)*, 1–6. <https://doi.org/10.1109/CCWC.2017.7868373>
- Waltham, A. C. (1989). *Ground subsidence*.
- Wang, B., Xu, J., & Xuan, D. (2018). Time function model of dynamic surface subsidence assessment of grout-injected overburden of a coal mine. *International Journal of Rock Mechanics and Mining Sciences*, 104, 1–8. <https://doi.org/10.1016/j.ijrmms.2018.01.044>
- Wang, Y., Hong, W., Zhang, Y., Lin, Y., Li, Y., Bai, Z., Zhang, Q., Lv, S., Liu, H., & Song, Y. (2020). Ground-based differential interferometry SAR: A review. *IEEE Geoscience and Remote Sensing Magazine*, 8(1), 43–70.
- Wegmüller, U., Strozzi, T., & Werner, C. (1998). Characterization of differential interferometry approaches. *EUSAR*, 98, 25–27.
- Whiteley, J. (2014). *Finite Element Methods. A Practical Guide*, 1.
- Wongsaroj, J., Borghi, F. X., Soga, K., Mair, R. J., Sugiyama, T., Hagiwara, T., & Bowers, K. H. (2005). Effect of TBM driving parameters on ground surface movements: Channel Tunnel Rail Link Contract 220. *Geotechnical Aspects of Underground Construction in Soft Ground*, 335–341.
- Xie, H., Yu, G., Yang, L., & Zhou, H. (1998). The influence of proximate fault morphology on ground subsidence due to extraction. *International Journal of Rock Mechanics and Mining Sciences*, 35(8), 1107–1111. [https://doi.org/10.1016/S0148-9062\(98\)00161-2](https://doi.org/10.1016/S0148-9062(98)00161-2)

- Xu, N., Kulatilake, P. H. S. W., Tian, H., Wu, X., Nan, Y., & Wei, T. (2013). Surface subsidence prediction for the WUTONG mine using a 3-D finite difference method. *Computers and Geotechnics*, 48, 134–145. <https://doi.org/10.1016/j.compgeo.2012.09.014>
- Yubero, M. T. (2008). *Análisis del proceso de compactación en una escombrera de sal*. <https://upcommons.upc.edu/handle/2099.1/6445>
- Zener, C. M., & Siegel, S. (1949). Elasticity and Anelasticity of metals. *The Journal of Physical Chemistry*, 53(9), 1468–1468.
- Zhang, C., Li, Z., Yu, C., Chen, B., Ding, M., Zhu, W., Yang, J., Liu, Z., & Peng, J. (2022). An integrated framework for wide-area active landslide detection with InSAR observations and SAR pixel offsets. *Landslides*, 19(12), 2905–2923. <https://doi.org/10.1007/s10346-022-01954-z>
- Zhang, J., Sun, Q., Fourie, A., Ju, F., & Dong, X. (2019). Risk assessment and prevention of surface subsidence in deep multiple coal seam mining under dense above-ground buildings: Case study. *Human and Ecological Risk Assessment: An International Journal*, 25(6), 1579–1593. <https://doi.org/10.1080/10807039.2018.1471579>
- Zhou, B., Yan, Y., Dai, H., Kang, J., Xie, X., & Pei, Z. (2022). Mining Subsidence Prediction Model and Parameters Inversion in Mountainous Areas. *Sustainability*, 14(15), 9445. <https://doi.org/10.3390/su14159445>
- Zhu, X., Guo, G., Zha, J., Chen, T., Fang, Q., & Yang, X. (2016). Surface dynamic subsidence prediction model of solid backfill mining. *Environmental Earth Sciences*, 75(12), 1007. <https://doi.org/10.1007/s12665-016-5817-9>
- Zienkiewicz, O. C., Taylor, R. L., & Zhu, J. Z. (2005). *The finite element method: Its basis and fundamentals*. Elsevier.

Appendixes

